

USING MAX/MIN TRANSVERSE REGIONS TO STUDY THE UNDERLYING
EVENT IN RUN 2 AT THE TEVATRON

By

L. ALBERTO CRUZ

A DISSERTATION PRESENTED TO THE GRADUATE SCHOOL OF THE
UNIVERSITY OF FLORIDA IN PARTIAL FULFILLMENT OF THE
REQUIREMENTS FOR THE DEGREE OF DOCTOR OF PHILOSOPHY

UNIVERSITY OF FLORIDA

2005

I dedicate this work to my wife Rachel and my parents, Rose “Shelley” and Luis Cruz.

ACKNOWLEDGMENTS

I am very grateful to my advisor, Prof. Richard Field, for his guidance and support throughout my research.

I also thank Craig Group for all of his invaluable help and patience, Bobby Scurlock and Mike Schmitt for the basketball breaks, and Brendan Lyden for the business class ticket back from China.

TABLE OF CONTENTS

	<u>page</u>
ACKNOWLEDGMENTS.....	iii
LIST OF TABLES.....	vi
LIST OF FIGURES.....	vii
ABSTRACT.....	xx
 CHAPTER	
1 INTRODUCTION.....	1
1.1 Forces and Particles.....	3
1.2 The Standard Model.....	6
1.3 QCD and the Structure of Hadrons.....	8
1.4 Hadron Hadron Interactions.....	11
1.4.1 Parton Model and Large P_T Processes.....	12
1.4.2 The “Underlying Event” in Proton-Antiproton Collisions: Pythia and Herwig.....	14
2 ACCELERATOR AND DETECTOR.....	17
2.1 The Accelerator Complex.....	17
2.2 The Collider Detector at Fermilab.....	22
2.2.1 The CDF Coordinate System.....	23
2.2.2 Tracking.....	26
2.2.3 Calorimeters.....	30
2.3 The CDF Trigger System.....	34
3 JETS AT CDF.....	36
4 MONTE-CARLO GENERATION AND CORRECTION FACTORS.....	38
4.1 Monte-Carlo Generation.....	38
4.2 Correcting the Data to the Particle Level.....	39
5 DATA SELECTION AND SYSTEMATIC ERRORS.....	69

5.1	Data Selection.....	69
5.2	Systematic Uncertainty.....	70
6	DISCUSSION OF RESULTS.....	73
6.1	The MAX/MIN Transverse Regions.....	76
6.2	“Leading Jet” Events.....	77
6.3	“Back-to-Back” Events.....	87
6.4	“Leading Jet” versus “Back-to-Back” Events.....	98
7	SUMMARY AND CONCLUSIONS.....	108
	REFERENCES.....	111
	BIOGRAPHICAL SKETCH.....	115

LIST OF TABLES

<u>Table</u>	<u>page</u>
1-1 Gauge bosons and forces of the Standard Model. There are eight different species of gluons each corresponding to a particular color charge.....	4
1-2 Properties of leptons.....	5
1-3 Properties of quarks	5
4-1 PYTHIA Tune A (5.3.3nt) at 1.96 TeV.....	38
4-2 HERWIG (5.3.3nt) at 1.96 TeV.....	39
4-3 Observables examined in the “transverse” region (see Fig. 6-2) as they are defined at the particle level and the detector level. Charged tracks are considered “good” if they pass the selection criterion given in Table 5-2. The mean charged particle $\langle p_T \rangle$ and the charged fraction $PT_{\text{sum}}/ET_{\text{sum}}$ are constructed on an event-by-event basis and then averaged over the events. There is one PT_{max} per event with $PT_{\text{max}} = 0$ if there are no charged particles ...	40
4-4 Correction factors for Method 1. PYTHIA Tune A and HERWIG are used to calculate the observables in Table 2 at the particle level in bins of particle jet#1 P_T (GEN) and at the detector level in bins of calorimeter jet#1 P_T (uncorrected). The detector level data in bins of calorimeter jet#1 PT (uncorrected) are corrected by multiplying by QCD Monte-Carlo factor, GEN/CDFSIM.....	41
5-1 Data sets (5.3.3nt) and event selection criterion used ($L \sim 380 \text{ pb}^{-1}$).....	69
5-2 Track selection criterion	70
5-3 Range of $P_T(\text{jet}\#1)$ used for each data set.....	70
5-4 The errors on the corrected observables in Table 4-3 include both the statistical error and the systematic uncertainty (added in quadrature). The systematic uncertainty consists of σ_1 and σ_2 (added in quadrature).....	71

LIST OF FIGURES

<u>Figure</u>	<u>page</u>
1-1 Illustration of the way QCD Monte-Carlo models simulate a proton-antiproton collision in which a “hard” 2-to-2 parton scattering with transverse momentum, P_{Thard} , has occurred. The resulting event contains particles that originate from the two outgoing partons (plus initial and final-state radiation) and particles that come from the breakup of the proton and antiproton (i.e. “beam-beam remnants”). The “underlying event” is everything except the two outgoing hard scattered “jets” and consists of the “beam-beam remnants” plus initial and final-state radiation. The “hard scattering” component consists of the outgoing two jets plus initial and final-state radiation.....	2
1-2 Relative strength of the strong and electromagnetic forces	11
1-3 The parton structure functions extracted from an analysis of deep inelastic scattering data at $Q^2=10\text{GeV}^2$	13
1-4 Hard “two-body” parton interaction producing a di-jet event in a proton-antiproton collision	14
1-5 Illustration of the way PYTHIA models the “underlying event” in proton-antiproton collision by including multiple parton interactions. In addition to the hard 2-to-2 parton-parton scattering with transverse momentum, $PT(\text{hard})$, there is a second “semi-hard” 2-to-2 parton-parton scattering that contributes particles to the “underlying event”	16
2-1 Overview of the accelerator complex at Fermilab. H ⁻ ions are injected into the linac from the Cockcroft-Walton, to travel to the Booster, then to the Main Ring, and finally to the Tevatron. Some protons are extracted from the Main Ring and are used to make anti-protons. The anti-protons are re-injected into the Main Ring and then into the Tevatron. The final proton-antiproton center of mass energy is $\sqrt{s}=1.96\text{ TeV}$	18
2-2 Run II instantaneous initial luminosity	20
2-3 Run II integrated luminosity	21
2-4 Solid cutaway view of the CDF II detector	22
2-5 Elevation view of the CDF II detector	23

2-6	The CDF coordinate system	24
2-7	A quarter of the CDF detector. Only the central and end-plug subsystems are shown.....	26
2-8	The CDF II tracking volume.....	27
2-9	Schematic layout of the silicon tracking system. The innermost layer, Layer00 consists of 6 sensors in z	28
2-10	End view of the three components of the silicon microstrip detector system.....	29
2-11	The COT sense wires and potential wires are alternated and arranged in 8 ‘superlayers’	30
2-12	Calorimeter tower segmentation in η - ϕ space	32
2-13	CEM/CES/CHA wedge.	33
2-14	CES strip and wire.	33
4-1	Example of fits to the QCD Monte-Carlo results. Shows the particle level predictions at 1.96 TeV for the density of charged particles, $dN_{\text{chg}}/d\eta d\phi$, with $p_T > 0.5$ GeV/c and $ \eta < 1$ in the “transMAX” and “transMIN” regions for “leading jet” events defined in Fig. 6-3 as a function of the leading particle jet P_T for PYTHIA Tune A (<i>top</i>) and HERWIG (<i>bottom</i>).....	42
4-2	Particle level predictions from PYTHIA Tune A and HERWIG for average density of particles $dN_{\text{all}}/d\eta d\phi$ (<i>top</i>), the average charged particle $P_{T\text{sum}}$ density, $dP_{T\text{sum}}/d\eta d\phi$ (<i>middle</i>), and the average charged particle $\langle p_T \rangle$ (<i>bottom</i>) for particles with $ \eta < 1$ in the “transverse” region for “leading jet” events defined in Fig. 6-3 as a function of the leading particle jet P_T	43
4-3	Particle level predictions from PYTHIA Tune A and HERWIG for average density of particles $dN_{\text{all}}/d\eta d\phi$ (<i>top</i>), the average charged particle $P_{T\text{sum}}$ density $dP_{T\text{sum}}/d\eta d\phi$ (<i>middle</i>), and the average charged particle $\langle p_T \rangle$ (<i>bottom</i>) for particles with $ \eta < 1$ in the “transverse” region for “back-to-back” events defined in Fig. 6-3 as a function of the leading jet P_T	44
4-4	Method 1 response factors for the density of charged particles, $dN_{\text{chg}}/d\eta d\phi$, with $p_T > 0.5$ GeV/c and $ \eta < 1$ in the “transMAX” region for “leading jet” events defined in Fig. 6-3 as a function of the leading jet P_T . Shows the particle level prediction (GEN) versus the leading particle jet P_T and the detector level result (CDFSIM) versus the leading calorimeter jet P_T (uncorrected) with $ \eta(\text{jet\#1}) < 2$ for PYTHIA Tune A (<i>top</i>) and HERWIG (<i>middle</i>). Also shows the ratio of the	

	detector level to the particle level, CDFSIM/GEN, versus the leading jet P_T (<i>i.e.</i> response factor).....	46
4-5	Method 1 response factors for the density of charged particles, $dN_{chg}/d\eta d\phi$, with $p_T > 0.5$ GeV/c and $ \eta < 1$ in the “transMIN” region for “leading jet” events defined in Fig. 6-3 as a function of the leading jet P_T . Shows the particle level prediction (GEN) versus the leading particle jet P_T and the detector level result (CDFSIM) versus the leading calorimeter jet P_T (uncorrected) with $ \eta(jet\#1) < 2$ for PYTHIA Tune A (<i>top</i>) and HERWIG (<i>middle</i>). Also shows the ratio of the detector level to the particle level, CDFSIM/GEN, versus the leading jet P_T (<i>i.e.</i> response factor).	48
4-6	Method 1 response factors for the PTsum density of charged particles, $dPT_{sum}/d\eta d\phi$, with $p_T > 0.5$ GeV/c and $ \eta < 1$ in the “transMAX” region for “leading jet” events defined in Fig. 6-3 as a function of the leading jet P_T . Shows the particle level prediction (GEN) versus the leading particle jet P_T and the detector level result (CDFSIM) versus the leading calorimeter jet P_T (uncorrected) with $ \eta(jet\#1) < 2$ for PYTHIA Tune A (<i>top</i>) and HERWIG (<i>middle</i>). Also shows the ratio of the detector level to the particle level, CDFSIM/GEN, versus the leading jet P_T (<i>i.e.</i> response factor).	49
4-7	Method 1 response factors for the PTsum density of charged particles, $dPT_{sum}/d\eta d\phi$, with $p_T > 0.5$ GeV/c and $ \eta < 1$ in the “transMIN” region for “leading jet” events defined in Fig. 6-3 as a function of the leading jet P_T . Shows the particle level prediction (GEN) versus the leading particle jet P_T and the detector level result (CDFSIM) versus the leading calorimeter jet P_T (uncorrected) with $ \eta(jet\#1) < 2$ for PYTHIA Tune A (<i>top</i>) and HERWIG (<i>middle</i>). Also shows the ratio of the detector level to the particle level, CDFSIM/GEN, versus the leading jet P_T (<i>i.e.</i> response factor).	50
4-8	Method 1 response factors for the average $\langle p_T \rangle$ of charged particles with $p_T > 0.5$ GeV/c and $ \eta < 1$ in the “transverse” region for “leading jet” events defined in Fig. 6-3 as a function of the leading jet P_T . Shows the particle level prediction (GEN) versus the leading particle jet P_T and the detector level result (CDFSIM) versus the leading calorimeter jet P_T (uncorrected) with $ \eta(jet\#1) < 2$ for PYTHIA Tune A (<i>top</i>) and HERWIG (<i>middle</i>). Also shows the ratio of the detector level to the particle level, CDFSIM/GEN, versus the leading jet P_T (<i>i.e.</i> response factor).....	51
4-9	Method 1 response factors for the average maximum p_T , PT_{max} , for charged particles with $p_T > 0.5$ GeV/c and $ \eta < 1$ in the “transverse” region for “leading jet” events defined in Fig. 6-3 as a function of the leading jet P_T . Shows the particle level prediction (GEN) versus the leading particle jet P_T and the detector level result (CDFSIM) versus the leading calorimeter jet P_T (uncorrected) with $ \eta(jet\#1) < 2$ for PYTHIA Tune A (<i>top</i>) and HERWIG (<i>middle</i>). Also shows	

	the ratio of the detector level to the particle level, CDFSIM/GEN, versus the leading jet P_T (<i>i.e.</i> response factor).....	52
4-10	Method 1 response factors for the ETsum density of all particles, $dE_T/d\eta d\phi$, with $ \eta < 1$ in the “transMAX” regions for “leading jet” events defined in Fig. 6-3 as a function of the leading jet P_T . Shows the particle level prediction (GEN) versus the leading particle jet P_T and the detector level result (CDFSIM) versus the leading calorimeter jet P_T (uncorrected) with $ \eta(\text{jet}\#1) < 2$ for PYTHIA Tune A (<i>top</i>) and HERWIG (<i>middle</i>). Also shows the ratio of the detector level to the particle level, CDFSIM/GEN, versus the leading jet P_T (<i>i.e.</i> response factor).....	53
4-11	Method 1 response factors for the ETsum density of all particles, $dE_T/d\eta d\phi$, with $ \eta < 1$ in the “transMIN” regions for “leading jet” events defined in Fig. 6-3 as a function of the leading jet P_T . Shows the particle level prediction (GEN) versus the leading particle jet P_T and the detector level result (CDFSIM) versus the leading calorimeter jet P_T (uncorrected) with $ \eta(\text{jet}\#1) < 2$ for PYTHIA Tune A (<i>top</i>) and HERWIG (<i>middle</i>). Also shows the ratio of the detector level to the particle level, CDFSIM/GEN, versus the leading jet P_T (<i>i.e.</i> response factor).....	54
4-12	Method 1 response factors for the charged fraction, $PT_{\text{sum}}/ET_{\text{sum}}$, in the “transverse” region for “leading jet” events defined in Fig. 6-3 as a function of the leading jet P_T , where PT_{sum} includes charged particles with $p_T > 0.5$ GeV/c and $ \eta < 1$ and the ET_{sum} includes all particles with $ \eta < 1$. Shows the particle level prediction (GEN) versus the leading particle jet P_T and the detector level result (CDFSIM) versus the leading calorimeter jet P_T (uncorrected) with $ \eta(\text{jet}\#1) < 2$ for PYTHIA Tune A (<i>top</i>) and HERWIG (<i>middle</i>). Also shows the ratio of the detector level to the particle level, CDFSIM/GEN, versus the leading jet P_T (<i>i.e.</i> response factor).....	55
4-13	Shows the ratio of the detector level to the particle level, CDFSIM/GEN, versus the leading jet P_T (method 1 response factors) for PYTHIA Tune A for the “transMAX”, “transMIN”, and “transverse” regions for “leading jet” events defined in Fig. 6-3 as a function of the leading jet P_T . Shows the density of charged particles $dN_{\text{chg}}/d\eta d\phi$ with $p_T > 0.5$ GeV/c and $ \eta < 1$ (<i>top</i>), the PT_{sum} density of charged particles $dPT_{\text{sum}}/d\eta d\phi$ with $p_T > 0.5$ GeV/c and $ \eta < 1$ (<i>middle</i>), and ET_{sum} density of all particles $dE_T/d\eta d\phi$ with $ \eta < 1$ (<i>bottom</i>).....	56
4-14	Method 1 response factors for the density of charged particles, $dN_{\text{chg}}/d\eta d\phi$, with $p_T > 0.5$ GeV/c and $ \eta < 1$ in the “transMAX” region for “back-to-back” events defined in Fig. 6-3 as a function of the leading jet P_T . Shows the particle level prediction (GEN) versus the leading particle jet P_T and the detector level result (CDFSIM) versus the leading calorimeter jet P_T (uncorrected) with $ \eta(\text{jet}\#1) < 2$ for PYTHIA Tune A (<i>top</i>) and HERWIG (<i>middle</i>). Also shows	

- the ratio of the detector level to the particle level, CDFSIM/GEN, versus the leading jet P_T (*i.e.* response factor).57
- 4-15 Method 1 response factors for the density of charged particles, $dN_{chg}/d\eta d\phi$, with $p_T > 0.5$ GeV/c and $|\eta| < 1$ in the “transMIN” region for “back-to-back” events defined in Fig. 6-3 as a function of the leading jet P_T . Shows the particle level prediction (GEN) versus the leading particle jet P_T and the detector level result (CDFSIM) versus the leading calorimeter jet P_T (uncorrected) with $|\eta(jet\#1)| < 2$ for PYTHIA Tune A (*top*) and HERWIG (*middle*). Also shows the ratio of the detector level to the particle level, CDFSIM/GEN, versus the leading jet P_T (*i.e.* response factor).58
- 4-16 Method 1 response factors for the PTsum density of charged particles, $dPT_{sum}/d\eta d\phi$, with $p_T > 0.5$ GeV/c and $|\eta| < 1$ in the “transMAX” region for “back-to-back” events defined in Fig. 6-3 as a function of the leading jet P_T . Shows the particle level prediction (GEN) versus the leading particle jet P_T and the detector level result (CDFSIM) versus the leading calorimeter jet P_T (uncorrected) with $|\eta(jet\#1)| < 2$ for PYTHIA Tune A (*top*) and HERWIG (*middle*). Also shows the ratio of the detector level to the particle level, CDFSIM/GEN, versus the leading jet P_T (*i.e.* response factor).59
- 4-17 Method 1 response factors for the PTsum density of charged particles, $dPT_{sum}/d\eta d\phi$, with $p_T > 0.5$ GeV/c and $|\eta| < 1$ in the “transMIN” region for “back-to-back” events defined in Fig. 6-3 as a function of the leading jet P_T . Shows the particle level prediction (GEN) versus the leading particle jet P_T and the detector level result (CDFSIM) versus the leading calorimeter jet P_T (uncorrected) with $|\eta(jet\#1)| < 2$ for PYTHIA Tune A (*top*) and HERWIG (*middle*). Also shows the ratio of the detector level to the particle level, CDFSIM/GEN, versus the leading jet P_T (*i.e.* response factor).60
- 4-18 Method 1 response factors for the average $\langle p_T \rangle$ of charged particles with $p_T > 0.5$ GeV/c and $|\eta| < 1$ in the “transverse” region for “back-to-back” events defined in Fig. 6-3 as a function of the leading jet P_T . Shows the particle level prediction (GEN) versus the leading particle jet P_T and the detector level result (CDFSIM) versus the leading calorimeter jet P_T (uncorrected) with $|\eta(jet\#1)| < 2$ for PYTHIA Tune A (*top*) and HERWIG (*middle*). Also shows the ratio of the detector level to the particle level, CDFSIM/GEN, versus the leading jet P_T (*i.e.* response factor).61
- 4-19 Method 1 response factors for the average maximum p_T , PT_{max} , for charged particles with $p_T > 0.5$ GeV/c and $|\eta| < 1$ in the “transverse” region for “back-to-back” events defined in Fig. 6-3 as a function of the leading jet P_T . Shows the particle level prediction (GEN) versus the leading particle jet P_T and the detector level result (CDFSIM) versus the leading calorimeter jet P_T (uncorrected) with $|\eta(jet\#1)| < 2$ for PYTHIA Tune A (*top*) and HERWIG (*middle*). Also shows

	the ratio of the detector level to the particle level, CDFSIM/GEN, versus the leading jet P_T (<i>i.e.</i> response factor).....	62
4-20	Method 1 response factors for the ETsum density of all particles, $dE_T/d\eta d\phi$, with $ \eta < 1$ in the “transMAX” regions for “back-to-back” events defined in Fig. 6-3 as a function of the leading jet P_T . Shows the particle level prediction (GEN) versus the leading particle jet P_T and the detector level result (CDFSIM) versus the leading calorimeter jet P_T (uncorrected) with $ \eta(\text{jet}\#1) < 2$ for PYTHIA Tune A (<i>top</i>) and HERWIG (<i>middle</i>). Also shows the ratio of the detector level to the particle level, CDFSIM/GEN, versus the leading jet P_T (<i>i.e.</i> response factor).....	63
4-21	Method 1 response factors for the ETsum density of all particles, $dE_T/d\eta d\phi$, with $ \eta < 1$ in the “transMIN” regions for “back-to-back” events defined in Fig. 6-3 as a function of the leading jet P_T . Shows the particle level prediction (GEN) versus the leading particle jet P_T and the detector level result (CDFSIM) versus the leading calorimeter jet P_T (uncorrected) with $ \eta(\text{jet}\#1) < 2$ for PYTHIA Tune A (<i>top</i>) and HERWIG (<i>middle</i>). Also shows the ratio of the detector level to the particle level, CDFSIM/GEN, versus the leading jet P_T (<i>i.e.</i> response factor).....	64
4-22	Method 1 response factors for the charged fraction, $PT_{\text{sum}}/ET_{\text{sum}}$, in the “transverse” region for “back-to-back” events defined in Fig. 6-3 as a function of the leading jet P_T , where PT_{sum} includes charged particles with $p_T > 0.5$ GeV/c and $ \eta < 1$ and the ET_{sum} includes all particles with $ \eta < 1$. Shows the particle level prediction (GEN) versus the leading particle jet P_T and the detector level result (CDFSIM) versus the leading calorimeter jet P_T (uncorrected) with $ \eta(\text{jet}\#1) < 2$ for PYTHIA Tune A (<i>top</i>) and HERWIG (<i>middle</i>). Also shows the ratio of the detector level to the particle level, CDFSIM/GEN, versus the leading jet P_T (<i>i.e.</i> response factor).....	65
4-23	Leading jet P_T correction used in method 2 for “leading jet” events. Shows the difference in the observed leading jet P_T at the detector level (<i>i.e.</i> in the calorimeter) compared with the true P_T (<i>i.e.</i> corrected) of matched leading particle jets using PYTHIA Tune A and HERWIG.....	66
4-24	Method 2 response factors from PYTHIA Tune A for “leading jet” events defined in Fig. 6-3 as a function of the leading jet P_T . Shows the particle level prediction (GEN) versus the leading particle jet P_T and the detector level result (CDFSIMcor) versus the leading calorimeter jet P_T (corrected) with $ \eta(\text{jet}\#1) < 2$. Also shows the ratio of the detector level to the particle level, CDFSIMcor/GEN, versus the leading jet P_T (<i>i.e.</i> response factor).....	67
4-25	Compares the method 1 response factors versus the leading jet P_T (uncorrected) with the method 2 response factors versus the leading jet P_T (corrected) from PYTHIA Tune A.....	68

- 5-1 Data at 1.96 TeV corrected to the particle level using method 1 and method 2 compared with PYTHIA Tune A and HERWIG at the particle level. Shows the density of charged particles, $dN_{chg}/d\eta d\phi$ (*top*), the PTsum density of charged particles, $dPTsum/d\eta d\phi$ (*middle*), ($p_T > 0.5$ GeV/c and $|\eta| < 1$), and the ETsum density, $dE_T/d\eta d\phi$ (*bottom*), for particles with $|\eta| < 1$ in the “transverse” region (average of “transMAX” and “transMIN”) for “leading jet” events defined in Fig. 6-3 as a function of the leading jet P_T72
- 6-1 Illustration of correlations in azimuthal angle $\Delta\phi$ relative to the direction of the leading jet (MidPoint, $R = 0.7$) in the event, jet#1. The angle $\Delta\phi = \phi - \phi_{jet\#1}$ is the relative azimuthal angle between charged particles and the direction of jet#1. The “toward” region is defined by $|\Delta\phi| < 60^\circ$ and $|\eta| < 1$, while the “away” region is $|\Delta\phi| > 120^\circ$ and $|\eta| < 1$. The “transverse” region is defined by $60^\circ < |\Delta\phi| < 120^\circ$ and $|\eta| < 1$. Each of the three regions “toward”, “transverse”, and “away” and has an overall area in η - ϕ space of $\Delta\eta\Delta\phi = 4\pi/3$. We examine charged particles in the range $p_T > 0.5$ GeV/c and $|\eta| < 1$, but allow the leading jet to be in the region $|\eta(jet\#1)| < 2$75
- 6-2 Illustration of correlations in azimuthal angle $\Delta\phi$ relative to the direction of the leading jet (highest E_T jet) in the event, jet#1. The angle $\Delta\phi = \phi - \phi_{jet\#1}$ is the relative azimuthal angle between charged particles and the direction of jet#1. The “toward” region is defined by $|\Delta\phi| < 60^\circ$ and $|\eta| < 1$, while the “away” region is $|\Delta\phi| > 120^\circ$ and $|\eta| < 1$. The two “transverse” regions $60^\circ < \Delta\phi < 120^\circ$ and $60^\circ < -\Delta\phi < 120^\circ$ are referred to as “transverse 1” and “transverse 2”. Each of the two “transverse” regions have an area in η - ϕ space of $\Delta\eta\Delta\phi = 4\pi/6$. The overall “transverse” region defined in Fig. 3 corresponds to combining the “transverse 1” and “transverse 2” regions. Events in which there are no restrictions placed on the on the second highest E_T jet, jet#2, are referred to as “leading jet” events (*left*). Events with at least two jets where the leading two jets are nearly “back-to-back” ($\Delta\phi_{12} > 150^\circ$) with $E_T(jet\#2)/E_T(jet\#1) > 0.8$ are referred to as “back-to-back” events (*right*).76
- 6-3 Illustration of correlations in azimuthal angle $\Delta\phi$ relative to the direction of the leading jet (highest P_T jet) in the event, jet#1 for “leading jet” events (*left*) and “back-to-back” events (*right*) as defined in Fig. 4. The angle $\Delta\phi = \phi - \phi_{jet\#1}$ is the relative azimuthal angle between charged particles (or calorimeter towers) and the direction of jet#1. On an event by event basis, we define “transMAX” (“transMIN”) to be the maximum (minimum) of the two “transverse” regions, $60^\circ < \Delta\phi < 120^\circ$ and $60^\circ < -\Delta\phi < 120^\circ$. “TransMAX” and “transMIN” each have an area in η - ϕ space of $\Delta\eta\Delta\phi = 4\pi/6$. The overall “transverse” region defined in Fig. 3 includes both the “transMAX” and the “transMIN” region76
- 6-4 Illustration of the topology of a proton-antiproton collision in which a “hard” parton-parton collision has occurred. The “toward” region as defined in Fig. 6-1 contains the leading “jet”, while the “away” region, on the average, contains the

	“away-side” “jet”. The “transverse” region is perpendicular to the plane of the hard 2-to-2 scattering and is very sensitive to the “underlying event”. For events with large initial or final-state radiation the “transMAX” region defined in Fig. 6-3 would contain the third jet while both the “transMAX” and “transMIN” regions receive contributions from the beam-beam remnants (see Fig. 1-1). Thus the “transMIN” region is very sensitive to the beam-beam remnants, while the “transMAX” minus the “transMIN” is very sensitive to initial and final-state radiation.	77
6-5	Data at 1.96 TeV on the density of charged particles, $dN_{chg}/d\eta d\phi$, with $p_T > 0.5$ GeV/c and $ \eta < 1$ in the “transMAX” and “transMIN” regions for “leading jet” events defined in Fig. 6-3 as a function of the leading jet P_T compared with PYTHIA Tune A and HERWIG. (<i>top</i>) Shows the uncorrected data (with statistical errors only) compared with the theory after detector simulation (CDFSIM). (<i>bottom</i>) Shows the data corrected to the particle level (with errors that include both the statistical error and the systematic uncertainty) compared with the theory at the particle level (<i>i.e.</i> generator level).	79
6-6	Data at 1.96 TeV on the density of charged particles, $dN_{chg}/d\eta d\phi$, with $p_T > 0.5$ GeV/c and $ \eta < 1$ in the “transverse” region (average of “transMAX” and “transMIN”) for “leading jet” events defined in Fig. 6-3 as a function of the leading jet P_T compared with PYTHIA Tune A and HERWIG. (<i>top</i>) Shows the uncorrected data (with statistical errors only) compared with the theory after detector simulation (CDFSIM). (<i>bottom</i>) Shows the data corrected to the particle level (with errors that include both the statistical error and the systematic uncertainty) compared with the theory at the particle level (<i>i.e.</i> generator level).	80
6-7	Data at 1.96 TeV on the PTsum density of charged particles, $dPT_{sum}/d\eta d\phi$, with $p_T > 0.5$ GeV/c and $ \eta < 1$ in the “transMAX” and “transMIN” regions for “leading jet” events defined in Fig. 6-3 as a function of the leading jet P_T compared with PYTHIA Tune A and HERWIG. (<i>top</i>) Shows the uncorrected data (with statistical errors only) compared with the theory after detector simulation (CDFSIM). (<i>bottom</i>) Shows the data corrected to the particle level (with errors that include both the statistical error and the systematic uncertainty) compared with the theory at the particle level (<i>i.e.</i> generator level).	81
6-8	Data at 1.96 TeV on the charged PTsum density, $dPT_{sum}/d\eta d\phi$, with $p_T > 0.5$ GeV/c and $ \eta < 1$ in the “transverse” region (average of “transMAX” and “transMIN”) for “leading jet” events defined in Fig. 6-3 as a function of the leading jet P_T compared with PYTHIA Tune A and HERWIG. (<i>top</i>) Shows the uncorrected data (with statistical errors only) compared with the theory after detector simulation (CDFSIM). (<i>bottom</i>) Shows the data corrected to the particle level (with errors that include both the statistical error and the systematic uncertainty) compared with the theory at the particle level (<i>i.e.</i> generator level).	82

- 6-9 Data at 1.96 TeV on the average $\langle p_T \rangle$ of charged particles with $p_T > 0.5$ GeV/c and $|\eta| < 1$ in the “transverse” region for “leading jet” events defined in Fig. 6-3 as a function of the leading jet P_T compared with PYTHIA Tune A and HERWIG. (*top*) Shows the uncorrected data (with statistical errors only) compared with the theory after detector simulation (CDFSIM). (*bottom*) Shows the data corrected to the particle level (with errors that include both the statistical error and the systematic uncertainty) compared with the theory at the particle level (*i.e.* generator level).83
- 6-10 Data at 1.96 TeV on the average maximum p_T , P_{Tmax} , for charged particles with $p_T > 0.5$ GeV/c and $|\eta| < 1$ in the “transverse” region for “leading jet” events defined in Fig. 6-3 as a function of the leading jet P_T compared with PYTHIA Tune A and HERWIG. (*top*) Shows the uncorrected data (with statistical errors only) compared with the theory after detector simulation (CDFSIM). (*bottom*) Shows the data corrected to the particle level (with errors that include both the statistical error and the systematic uncertainty) compared with the theory at the particle level (*i.e.* generator level).85
- 6-11 Data at 1.96 TeV on the ETsum density, $dE_T/d\eta d\phi$, for particles with $|\eta| < 1$ in the “transMAX” and “transMIN” regions for “leading jet” events defined in Fig. 6-3 as a function of the leading jet P_T compared with PYTHIA Tune A and HERWIG. (*top*) Shows the uncorrected data (with statistical errors only) compared with the theory after detector simulation (CDFSIM). (*bottom*) Shows the data corrected to the particle level (with errors that include both the statistical error and the systematic uncertainty) compared with the theory at the particle level (*i.e.* generator level).86
- 6-12 Data at 1.96 TeV on the ETsum density, $dE_T/d\eta d\phi$, for particles with $|\eta| < 1$ in the “transverse” region (average of “transMAX” and “transMIN”) for “leading jet” events defined in Fig. 6-3 as a function of the leading jet P_T compared with PYTHIA Tune A and HERWIG. (*top*) Shows the uncorrected data (with statistical errors only) compared with the theory after detector simulation (CDFSIM). (*bottom*) Shows the data corrected to the particle level (with errors that include both the statistical error and the systematic uncertainty) compared with the theory at the particle level (*i.e.* generator level).87
- 6-13 Data at 1.96 TeV on the charged fraction, P_{Tsum}/E_{Tsum} , in the “transverse” region for “leading jet” events defined in Fig. 6-3 as a function of the leading jet P_T , where P_{Tsum} includes charged particles with $p_T > 0.5$ GeV/c and $|\eta| < 1$ and the E_{Tsum} includes all particles with $|\eta| < 1$. The data are compared with PYTHIA Tune A and HERWIG. (*top*) Shows the uncorrected data (with statistical errors only) compared with the theory after detector simulation (CDFSIM). (*bottom*) Shows the data corrected to the particle level (with errors that include both the statistical error and the systematic uncertainty) compared with the theory at the particle level (*i.e.* generator level).88

- 6-14 Data at 1.96 TeV on the density of charged particles, $dN_{\text{chg}}/d\eta d\phi$, with $p_T > 0.5$ GeV/c and $|\eta| < 1$ in the “transMAX” and “transMIN” regions for “back-to-back” events defined in Fig. 6-3 as a function of the leading jet P_T compared with PYTHIA Tune A and HERWIG. (*top*) Shows the uncorrected data (with statistical errors only) compared with the theory after detector simulation (CDFSIM). (*bottom*) Shows the data corrected to the particle level (with errors that include both the statistical error and the systematic uncertainty) compared with the theory at the particle level (*i.e.* generator level).90
- 6-15 Data at 1.96 TeV on the density of charged particles, $dN_{\text{chg}}/d\eta d\phi$, with $p_T > 0.5$ GeV/c and $|\eta| < 1$ in the “transverse” region (average of “transMAX” and “transMIN”) for “back-to-back” events defined in Fig. 6-3 as a function of the leading jet P_T compared with PYTHIA Tune A and HERWIG. (*top*) Shows the uncorrected data (with statistical errors only) compared with the theory after detector simulation (CDFSIM). (*bottom*) Shows the data corrected to the particle level (with errors that include both the statistical error and the systematic uncertainty) compared with the theory at the particle level (*i.e.* generator level).91
- 6-16 Data at 1.96 TeV on the PTsum density of charged particles, $dP_{T\text{sum}}/d\eta d\phi$, with $p_T > 0.5$ GeV/c and $|\eta| < 1$ in the “transMAX” and “transMIN” regions for “back-to-back” events defined in Fig. 6-3 as a function of the leading jet P_T compared with PYTHIA Tune A and HERWIG. (*top*) Shows the uncorrected data (with statistical errors only) compared with the theory after detector simulation (CDFSIM). (*bottom*) Shows the data corrected to the particle level (with errors that include both the statistical error and the systematic uncertainty) compared with the theory at the particle level (*i.e.* generator level).92
- 6-17 Data at 1.96 TeV on the PTsum density, $dP_{T\text{sum}}/d\eta d\phi$, with $p_T > 0.5$ GeV/c and $|\eta| < 1$ in the “transverse” region (average of “transMAX” and “transMIN”) for “back-to-back” events defined in Fig. 6-3 as a function of the leading jet P_T compared with PYTHIA Tune A and HERWIG. (*top*) Shows the uncorrected data (with statistical errors only) compared with the theory after detector simulation (CDFSIM). (*bottom*) Shows the data corrected to the particle level (with errors that include both the statistical error and the systematic uncertainty) compared with the theory at the particle level (*i.e.* generator level).93
- 6-18 Data at 1.96 TeV on the average $\langle p_T \rangle$ of charged particles with $p_T > 0.5$ GeV/c and $|\eta| < 1$ in the “transverse” region for “back-to-back” events defined in Fig. 6-3 as a function of the leading jet P_T compared with PYTHIA Tune A and HERWIG. (*top*) Shows the uncorrected data (with statistical errors only) compared with the theory after detector simulation (CDFSIM). (*bottom*) Shows the data corrected to the particle level (with errors that include both the statistical error and the systematic uncertainty) compared with the theory at the particle level (*i.e.* generator level).94

6-19	Data at 1.96 TeV on the average maximum p_T , P_{Tmax} , for charged particles with $p_T > 0.5$ GeV/c and $ \eta < 1$ in the “transverse” region for “back-to-back” events defined in Fig. 6-3 as a function of the leading jet P_T compared with PYTHIA Tune A and HERWIG. (<i>top</i>) Shows the uncorrected data (with statistical errors only) compared with the theory after detector simulation (CDFSIM). (<i>bottom</i>) Shows the data corrected to the particle level (with errors that include both the statistical error and the systematic uncertainty) compared with the theory at the particle level (<i>i.e.</i> generator level).	95
6-20	Data at 1.96 TeV on the ETsum density, $dE_T/d\eta d\phi$, for particles with $ \eta < 1$ in the “transMAX” and “transMIN” regions for “back-to-back” events defined in Fig. 6-3 as a function of the leading jet P_T compared with PYTHIA Tune A and HERWIG. (<i>top</i>) Shows the uncorrected data (with statistical errors only) compared with the theory after detector simulation (CDFSIM). (<i>bottom</i>) Shows the data corrected to the particle level (with errors that include both the statistical error and the systematic uncertainty) compared with the theory at the particle level (<i>i.e.</i> generator level).	97
6-21	Data at 1.96 TeV on the ETsum density, $dE_T/d\eta d\phi$, for particles with $ \eta < 1$ in the “transverse” region (average of “transMAX” and “transMIN”) for “back-to-back” events defined in Fig. 6-3 as a function of the leading jet P_T compared with PYTHIA Tune A and HERWIG. (<i>top</i>) Shows the uncorrected data (with statistical errors only) compared with the theory after detector simulation (CDFSIM). (<i>bottom</i>) Shows the data corrected to the particle level (with errors that include both the statistical error and the systematic uncertainty) compared with the theory at the particle level (<i>i.e.</i> generator level)	98
6-22	Data at 1.96 TeV on the charged fraction, $PTsum/ETsum$, in the “transverse” region for “back-to-back” events defined in Fig. 6-3 as a function of the leading jet P_T , where $PTsum$ includes charged particles with $p_T > 0.5$ GeV/c and $ \eta < 1$ and the $ETsum$ includes all particles with $ \eta < 1$. The data are compared with PYTHIA Tune A and HERWIG. (<i>top</i>) Shows the uncorrected data (with statistical errors only) compared with the theory after detector simulation (CDFSIM). (<i>bottom</i>) Shows the data corrected to the particle level (with errors that include both the statistical error and the systematic uncertainty) compared with the theory at the particle level (<i>i.e.</i> generator level).	99
6-23	Data at 1.96 TeV on the density of charged particles, $dN_{chg}/d\eta d\phi$, with $p_T > 0.5$ GeV/c and $ \eta < 1$ in the “transMAX” region (<i>top</i>), “transMIN” region (<i>middle</i>), and “transverse” region (average of “transMAX” and “transMIN”) (<i>bottom</i>) for “leading jet” and “back-to-back” events defined in Fig. 6-3 as a function of the leading jet P_T compared with PYTHIA Tune A and HERWIG. The data are corrected to the particle level (with errors that include both the statistical error and the systematic uncertainty) and compared with the theory at the particle level (<i>i.e.</i> generator level)	101

- 6-24 Data at 1.96 TeV on charged PTsum density of charged particles, $dPT_{\text{sum}}/d\eta d\phi$, with $p_T > 0.5$ GeV/c and $|\eta| < 1$ in the “transMAX” region (*top*), “transMIN” region (*middle*), and “transverse” region (average of “transMAX” and “transMIN”) (*bottom*) for “leading jet” and “back-to-back” events defined in Fig. 6-3 as a function of the leading jet P_T compared with PYTHIA Tune A and HERWIG. The data are corrected to the particle level (with errors that include both the statistical error and the systematic uncertainty) and compared with the theory at the particle level (*i.e.* generator level).102
- 6-25 Figure 6-25: Data at 1.96 TeV on the average $\langle p_T \rangle$ of charged particles (*top*) and the average maximum p_T , PT_{max} , for charged particles (*bottom*) with $p_T > 0.5$ GeV/c and $|\eta| < 1$ in the “transverse” region for “leading jet” and “back-to-back” events defined in Fig. 6-3 as a function of the leading jet P_T compared with PYTHIA Tune A and HERWIG. The data are corrected to the particle level (with errors that include both the statistical error and the systematic uncertainty) and compared with the theory at the particle level (*i.e.* generator level).104
- 6-26 Data at 1.96 TeV on the ETsum density, $dE_T/d\eta d\phi$, for particles with $|\eta| < 1$ in the “transMAX” region (*top*), “transMIN” region (*middle*), and “transverse” region (average of “transMAX” and “transMIN”) (*bottom*) for “leading jet” and “back-to-back” events defined in Fig. 6-3 as a function of the leading jet P_T compared with PYTHIA Tune A and HERWIG. The data are corrected to the particle level (with errors that include both the statistical error and the systematic uncertainty) and compared with the theory at the particle level (*i.e.* generator level).105
- 6-27 Data at 1.96 TeV on the charged fraction, $PT_{\text{sum}}/ET_{\text{sum}}$, in the “transverse” region defined in Fig. 6-3 for “leading jet” events (*top*) and “back-to-back” events (*bottom*) as a function of the leading jet P_T , where PT_{sum} includes charged particles with $p_T > 0.5$ GeV/c and $|\eta| < 1$ and the ET_{sum} includes all particles with $|\eta| < 1$, compared with PYTHIA Tune A and HERWIG. The data are corrected to the particle level (with errors that include both the statistical error and the systematic uncertainty) and compared with the theory at the particle level (*i.e.* generator level).106
- 6-28 Data at 1.96 TeV on the density of charged particles, $dN/d\eta d\phi$ and the $P_{T_{\text{sum}}}$ density, $dP_{T_{\text{sum}}}/d\eta d\phi$ for charged particles with $p_T > 0.5$ GeV/c and $|\eta| < 1$ for the “transMAX” minus the “transMIN” region defined in figure 6-3 for “leading jet” and “back-to-back” events defined in Fig. 6-2 as a function of the leading jet P_T compared with PYTHIA Tune A and HERWIG. The “transDIF” $E_{T_{\text{sum}}}$ density, $dE_{T_{\text{sum}}}/d\eta d\phi$ for particles with $|\eta| < 1$ is also presented. The data are corrected to the particle level (with errors that include both the statistical error and the systematic uncertainty) and compared with the theory at the particle level (*i.e.* generator level).108

7-1	A comparison between the Run I and Run II analysis on the PTsum density in the “transverse” region. (<i>top</i>) Data uncorrected (with errors that include both statistical and the systematic uncertainty) at 1.8 TeV on the charged PTsum density, $dPT_{\text{sum}}/d\eta d\phi$, with $PT > 0.5$ GeV/c and $ \eta < 1.0$ for leading jet events defined in Fig. 6-3 as a function of leading jet PT compared PYTHIA set A, PYTHIA set B, and HERWIG. (<i>bottom</i>) Data corrected (with errors that include both statistical and the systematic uncertainty) at 1.96 TeV on the charged PTsum density, $dPT_{\text{sum}}/d\eta d\phi$, with $PT > 0.5$ GeV/c and $ \eta < 1.0$ for “leading jet events” defined in Fig. 6-3 as a function of leading jet PT compared PYTHIA Tune A and HERWIG.	11
-----	--	----

Abstract of Dissertation Presented to the Graduate School
of the University of Florida in Partial Fulfillment of the
Requirements for the Degree of Doctor of Philosophy

USING MAX/MIN TRANSVERSE REGIONS TO STUDY THE UNDERLYING
EVENT IN RUN 2 AT THE TEVATRON

By

Luis Alberto Cruz

August 2005

Chair: Richard Field
Major Department: Physics

We study the behavior of the charged particle ($p_T > 0.5 \text{ GeV}/c$, $|\eta| < 1$) and energy ($|\eta| < 1$) components of the “underlying event” in hard scattering proton-antiproton collisions at 1.96 TeV. We use the direction of the leading calorimeter jet in each event to define two “transverse” regions of η - ϕ space that are very sensitive to the “underlying event”. Defining a variety of MAX and MIN “transverse” regions helps separate the “hard component” (initial and final-state radiation) from the “beam-beam remnant” and multiple parton interaction components. In addition, selecting events with at least two jets that are nearly back-to-back ($\Delta\phi_{12} > 150^\circ$) with $P_T(\text{jet}\#3) < 15 \text{ GeV}/c$ suppresses the hard initial and final-state radiation, thus increasing the sensitivity of the “transverse” region to the “beam-beam remnant” and the multiple parton scattering components of the “underlying event.” In this analysis we use the MidPoint algorithm ($R = 0.7$, $f_{\text{merge}} = 0.75$) and correct the observables to the particle level. The corrected observables are then compared with PYTHIA Tune A and HERWIG at the particle level (*i.e.*, generator level).

CHAPTER 1 INTRODUCTION

Elementary particle physics is concerned with the understanding of the fundamental constituents of matter. Our current understanding of nature reveals only a small number of fundamental particles. Furthermore, the taxonomy is greatly simplified because these particles are perfectly replicated in indistinguishable copies. It should then be sufficient to simply list these particles and describe their interactions. Unfortunately, due to their size, we are left to discover how they interact via indirect measurements. Classically this requires the study of decay rates, bound states, and scattering experiments. To fix the laws of physics in a formulated phrase, the traditional approach is to guess a form of the interaction and compare the resulting theoretical calculations to experimental measurements.

One important quantity measured by the experimentalist and calculated by the theorist is the differential scattering cross section. Suppose particles 1 and 2 collide, producing particles 3,4,...,n, the cross section is given by formula 1.1,

$$d\sigma = |M|^2 \frac{S}{4\sqrt{(p_1 \cdot p_2)^2 - (m_1 m_2)^2}} \left[\left(\frac{d^3 \vec{p}_3}{(2\pi)^3 2E_3} \right) \left(\frac{d^3 \vec{p}_4}{(2\pi)^3 2E_4} \right) \cdots \left(\frac{d^3 \vec{p}_n}{(2\pi)^3 2E_n} \right) \right] \times (2\pi)^4 \delta^4(p_1 + p_2 - p_3 - p_4 \cdots - p_n) \quad (1.1)$$

where M is the invariant amplitude (matrix element) for the process, $p_i = (E_i, \vec{p}_i)$ is the four-momentum of particle i (mass m_i), $E_i = \sqrt{m_i^2 + \vec{p}_i^2}$, and S is a statistical factor

The inclusive jet cross section at the Tevatron, $d\sigma/dE_T$ averaged over a small range of pseudorapidity, $\eta = -\ln(\tan \theta/2)$, is an important object for study because it tests

perturbative QCD at the highest Q^2 ($Q^2 = -q^2 = (p_i - p_f)^2$) scale currently possible [1,2]. This measurement continues to substantiate QCD and contributes to its global data fitting used to measure parton distribution functions [3]. It is imperative that we consider all systematic effects that influence our interpretation of the measurement.

One of the contributing effects results from the “underlying event” that is present in all proton-antiproton collisions. Figure 1-1 illustrates a “hard” 2-2 parton scattering with transverse momentum, $P_{T\text{hard}}$. The “hard” scattering component is comprised of the two outgoing jets plus initial and final-state radiation. Removal of the two outgoing jets leaves only the “underlying event.”

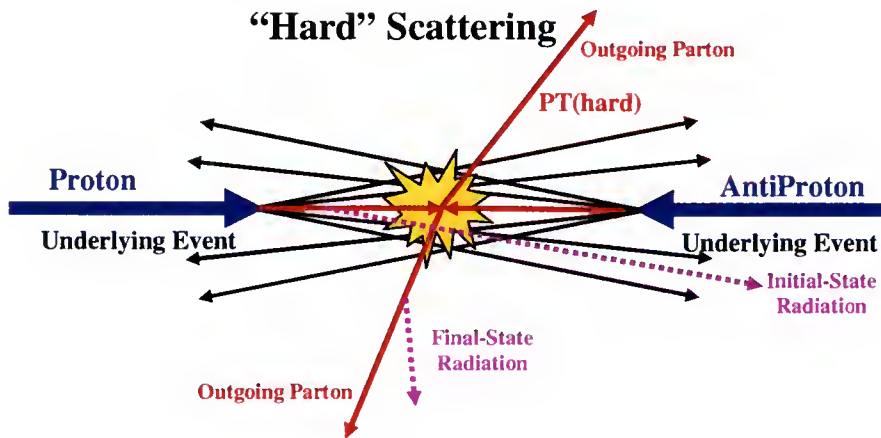


Figure 1-1: Illustration of the way QCD Monte-Carlo models simulate a proton-antiproton collision in which a “hard” 2-to-2 parton scattering with transverse momentum, P_T^{hard} , has occurred. The resulting event contains particles that originate from the two outgoing partons (plus initial and final-state radiation) and particles that come from the breakup of the proton and antiproton (*i.e.* “beam-beam remnants”). The “underlying event” is everything except the two outgoing hard scattered “jets” and consists of the “beam-beam remnants” plus initial and final-state radiation. The “hard scattering” component consists of the outgoing two jets plus initial and final-state radiation.

Theoretical analysis of such a process uses simulations based on QCD Monte Carlo models. The justification lies in the factorization theorem [4-6], which, roughly, states that physical observables are the product of short distance functions and long distance

functions. The short distance functions are calculable in perturbation theory, where the usual perturbative expansion in terms of Feynman diagrams is used to calculate matrix elements. The long distance functions are fit at a scale, but their evolution to any other scale is also calculable in perturbation theory. Of course, due to the nature of Quantum mechanics it is impossible to distinguish initial state radiation from final state radiation. However, in the Leading Log Approximation Figure 1-1 can be factorized into the following subprocesses: (1) final state emission; (2) initial state emission; (3) the elementary hard subprocess, which can be computed exactly to finite order in perturbation theory; and (4) The hadronization process.

Refinement of each of these subprocesses extends the comparative scale of high energy physics. The work presented here extends to higher energies the previous characterization of the “underlying event” [7-13]. Unlike the previous analysis we examine the energy in the transverse regions and correct the data back to the particle level.

1.1 Forces and Particles

Four known forces serve as the impetus of our physical theories: strong, electromagnetic, weak, and gravitational. Intimately related to these forces are the relatively few “elementary” particles on which they act: leptons, quarks, and bosons.

Our current understanding of gravity started with Sir Isaac Newton’s law of universal gravitation. This classical theory of gravity saw its relativistic generalization to the general theory of relativity by Albert Einstein. However, gravitational forces are the weakest, and they are important for massive bodies but negligible for nuclear and subnuclear particles.

Electrodynamics, the theory describing electromagnetic forces, owes its classical formulation to the Scottish physicist James Clerk Maxwell. It was not until the 1940's that Tomonaga, Feynman, and Schwinger would perfect the quantum theory of electrodynamics. The theory of weak interactions or flavordynamics was originally formulated by Fermi in 1933, but in the 1960's Glashow, Wienberg, and Salam (GWS) put it into its present form. In the GWS model the weak and electromagnetic interactions are treated as different manifestations of a single electroweak force. This electroweak force provides for the attraction between charged particles and is responsible for the β decay of nuclei.

Chromodynamics emerged in the mid-seventies to support the pioneering work of Yukawa on the strong force. The work of Gross, Politzer, and Wilczek on a strong force earned them recent recognition in the form of the 2004 Nobel Prize in physics. Strong forces act only at very small distances: they bind quarks into nucleons and nucleons together to make nuclei.

All of these apparently different forces are each mediated by the exchange of an integer-spin particle, called a boson. Table 1-1 summarizes the properties of the gauge bosons of the Standard Model.

Table 1-1: Gauge bosons and forces of the Standard Model. There are eight different species of gluons each corresponding to a particular color charge.

Boson	Force	Spin	Charge [e]	Mass [GeV/c ²]	Range [fm]
g	strong	1	0	0	$<\sim 1$
γ	electromagnetic	1	0	0	∞
W^{\pm}	weak	1	± 1	80.425 ± 0.038	$\approx 10^{-3}$
Z^0	weak	1	0	91.1876 ± 0.0021	$\approx 10^{-3}$

The Standard Model [14, 15] classifies elementary particles as structureless at all scales presently accessible. Furthermore, it states that all visible matter consists of elementary particles of two kinds: leptons and quarks. These particles are interpreted as quantum excitations of a field and are characterized by having spin $\frac{1}{2}$ intrinsic angular momentum in units of \hbar . They obey the Pauli Exclusion Principle and are called fermions. There are six types of leptons and six types of quarks which are each grouped into three generations according to their mass, the properties of which are summarized in Tables 1-2 and 1-3. Each has an associated antiparticle with the same mass and spin but opposite charge.

Table 1-2: Properties of leptons.

	Lepton	Spin	Charge [e]	Mass [MeV/c ²]
1st generation	e^-	1/2	-1	$0.51099892 \pm 0.00000004$
	ν_e	1/2	0	$< 3 \cdot 10^{-6}$
2nd generation	μ^-	1/2	-1	105.658369 ± 0.000009
	ν_μ	1/2	0	< 0.19
3rd generation	τ^-	1/2	-1	$1776.99^{+0.29}_{-0.26}$
	ν_τ	1/2	0	< 18.2

Table 1-3: Properties of quarks.

	Quark	Spin	Charge [e]	Mass
1st generation	u	1/2	+2/3	$1.5\text{-}4 \text{ MeV/c}^2$
	d	1/2	-1/3	$4\text{-}8 \text{ MeV/c}^2$
2nd generation	c	1/2	+2/3	$1.15\text{-}1.35 \text{ GeV/c}^2$
	s	1/2	-1/3	$80\text{-}130 \text{ MeV/c}^2$
3rd generation	t	1/2	+2/3	$178.0 \pm 4.3 \text{ GeV/c}^2$
	b	1/2	-1/3	$4.1\text{-}4.4 \text{ GeV/c}^2$

1.2 The Standard Model

The Standard Model of strong, weak, and electromagnetic interactions is based on the symmetry group $SU(3)_C \times SU(2)_L \times U(1)_Y$ [16] where the subscripts denote special features of a given symmetry which act on the quark and lepton fields. The C in $SU(3)_C$ stands for color. Each quark has three color components and $SU(3)_C$ transforms them into one another. $SU(3)_C$, the basis of quantum chromodynamics (QCD), is an exact symmetry of nature. There are eight massless gluons which correspond to the eight gauge fields of $SU(3)_C$. This description requires a new quantum number: color charge. By convention, the three colors are red, green, and blue and each quark is supposed to carry one of these colors. The gluons, the quanta of color fields, also carry color. Quarks are bound together in hadrons by the strong color force via the exchange of colored gluons. All observed hadrons are described in the parton model as color singlet states (referred to as “colorless”) composed of three quarks (baryons: qqq) or of a quark-antiquark pair (mesons: $q\bar{q}$). The quarks of these configurations are called valence quarks because they are responsible for the charge and other quantum numbers of hadrons.

The L on $SU(2)_L$, the weak isospin group, denotes the fact that only left-handed components, Ψ_L , of spinor fields, $\psi_L \equiv \left(\frac{1 - \gamma^5}{2} \right) \psi$, transform as doublets under that group. The right-handed spinor components $\psi_R \equiv \left(\frac{1 + \gamma^5}{2} \right) \psi$ are isosinglets under $SU(2)_L$; i.e., they are unchanged under $SU(2)_L$ transformations and therefore do not couple to its three gauge fields which we denote by $W_\mu^\pm \equiv \frac{W_\mu^1 \pm iW_\mu^2}{\sqrt{2}}$ and W_μ^3 . The fact

that only left-handed quarks and leptons couple to those gauge fields makes their (weak) interactions maximally parity violating [17].

The Y on $U(1)_Y$ stands for weak hypercharge, the charge associated with that Abelian group. That gauge group has one gauge field B_μ that couples to quarks and leptons via their hypercharge Y . It couples to left and right handed components of these particles differently and therefore also violates parity, but not maximally. The $SU(2)_L \times U(1)_Y$ part of the standard model is not an exact symmetry. If it were, the W_μ^\pm , W_μ^3 , and B_μ would all be massless gauge bosons. That is not the case. To accommodate electroweak phenomenology, a scalar (spin 0) field is introduced which breaks the symmetry $SU(2)_L \times U(1)_Y$ down to the $U(1)$ symmetry of QED. That breaking gives mass to the W_μ^\pm , and the combination of fields $Z_\mu = W_\mu^3 \cos \theta_w - B_\mu \sin \theta_w$ which is called the Z boson. The orthogonal combination $A_\mu = B_\mu \cos \theta_w + W_\mu^3 \sin \theta_w$ remains massless and is identified as the photon. The angle θ_w , called the weak mixing angle, is experimentally found to be $\sin^2 \theta_w = 0.23$. That leads to standard model predictions $\text{Mass}_w \approx 80 \text{ GeV}/c^2$ and $\text{Mass}_Z \approx 91 \text{ GeV}/c^2$. The discoveries of the W [18, 19] and Z [20, 21] bosons by the UA1 and UA2 collaborations at Cern substantiate the validity of the Standard Model. The search for the spin 0 Higgs Boson continues to be one of the most important problems to be addressed during Run 2 at the Tevatron and future LHC experiments.

1.3 QCD and the Structure of Hadrons

QCD is a non-Abelian¹ gauge theory that is based on the $SU(3)_C$ group of transformations which relate quarks of different colors. The gauge bosons associated with the eight group generators, known as gluons, can be emitted or absorbed by quarks in transition in which the color (but not flavor) can change. Since the gluons themselves carry color they can interact with each other as well.

In quantum field theories like QED and QCD any charge (color or electromagnetic) is shielded by a cloud of polarized charges: a quark can emit a gluon which can convert into $q\bar{q}$ or gg pairs which in turn can radiate gluons and we have a branching tree of quarks and gluons (this effect is called vacuum polarization). Because of the effect of charge screening the charge one measures depends on the distance (or wavelength, or transferred momentum Q^2) with which one is probing the charge itself. We thus have a “running” coupling constant which changes with the transferred momentum:

$$\alpha = \alpha(Q^2) \quad \text{with} \quad Q^2 = -q^2 > 0 \quad (1-2)$$

where q is the four-momentum of the virtual boson exchanged between charges.

For both QED and QCD the effective coupling constant α depends on the momentum (or distance) scale at which it is evaluated, and takes the general form of equation 1-3.

$$\alpha(Q^2) = \frac{\alpha(0)}{1 - X(Q^2)} \quad (1-3)$$

Where $\alpha(0)$ for QED is the fine structure constant and is approximately equal to $1/137$.

For QED it can be shown that $X(Q^2)$ takes the form of equation 1-4.

¹ A group or other algebraic object is called non-Abelian if the law of commutativity does not always hold.

$$X(Q^2) = \left(\sum_{i=1}^{N_f} \left(\frac{q_i}{e} \right)^2 \right) \frac{\alpha(\mu^2)}{3\pi} \ln \left(\frac{Q^2}{\mu^2} \right) \quad (1-4)$$

Here N_f is the number of fundamental fermions with masses below $\frac{1}{2}|Q|$ and μ is the mass of the heaviest fermion in the energy region being considered. Clearly, $X(Q^2)$ for QED is > 0 , and the coupling constant grows with energy. At some energy scale the coupling of QED becomes strong and perturbation theory no longer applies. Due to this behavior, the bare charge in QED is said to be “ultraviolet divergent.”

The coupling constant in QCD exhibits the opposite behavior. It can be shown that $X(Q^2)$ for QCD takes the form of equation 1-5.

$$X(Q^2) = \frac{\alpha_s(\mu^2)}{12\pi} \ln \left(\frac{Q^2}{\mu^2} \right) [2N_f - 11N_c], \quad (1-5)$$

Here N_f is the number of quark flavors with masses below $\frac{1}{2}|Q|$ and μ is the mass of the heaviest quark in the energy region being considered, and N_c is the number of colors. In contrast to the form of the QED term, for 6 flavors and 3 colors $2N_f - 11N_c < 0$ and therefore $\alpha(Q^2)$ decreases with increasing momentum (or shorter distances). Only in a world with more than 16 quark flavors (we are safely below this number at present energies) is the sign of $X(Q^2)$ the same as in QED. This results in an antiscreening of the color charge: by moving closer to the original quark the amount of the measured color charge decreases.

The QCD “running coupling constant” (Eq. 1-6) is usually expressed in terms of a parameter, Λ_{QCD} , that indicates the magnitude of the scale at which $\alpha_s(Q^2)$ becomes

$$\alpha_s(Q^2) \equiv \frac{4\pi}{\left(\frac{11}{3}N_c - \frac{2}{3}N_f \right) \ln \frac{Q^2}{\Lambda_{QCD}^2}}, \quad (1-6)$$

strong; it is determined experimentally to be about 0.2 GeV.

Figure 1-2 compares the relative strength of the strong and electromagnetic forces at different energy scales. With three colors and six flavors we can see that $\alpha_s(Q^2)$ in eq. 1-6 goes to zero as Q^2 goes to infinity. This results in quarks and gluons appearing almost like free particles when probed at very high energies or short distances. This behavior is called asymptotic freedom and allows perturbation theory to be applied to theoretical QCD calculations to produce experimentally verifiable predictions for hard scattering processes.

Asymptotic freedom is quickly overcome by the strong force as color charges separate. In contrast, as two electrically charged particles separate, the electric fields between them quickly diminish, allowing electrons to become unbound from nuclei. However, the gluon field lines associated with color charges do not radially fan out but remain confined to a narrow cylindrical region. This leads to an interaction energy that is proportional to the separation distance of the sources of the field lines. When quarks become separated, as happens in high energy hadron collisions, at some point it is energetically favorable for a new quark/antiquark pair to “pop” out of the vacuum than to allow the quarks to separate further. As a result of this, when quarks are produced in collisions, instead of seeing the individual quarks, we see an avalanche of colorless particles clustered together moving in roughly the same direction known as jets. This process is called hadronization, fragmentation or string-breaking.

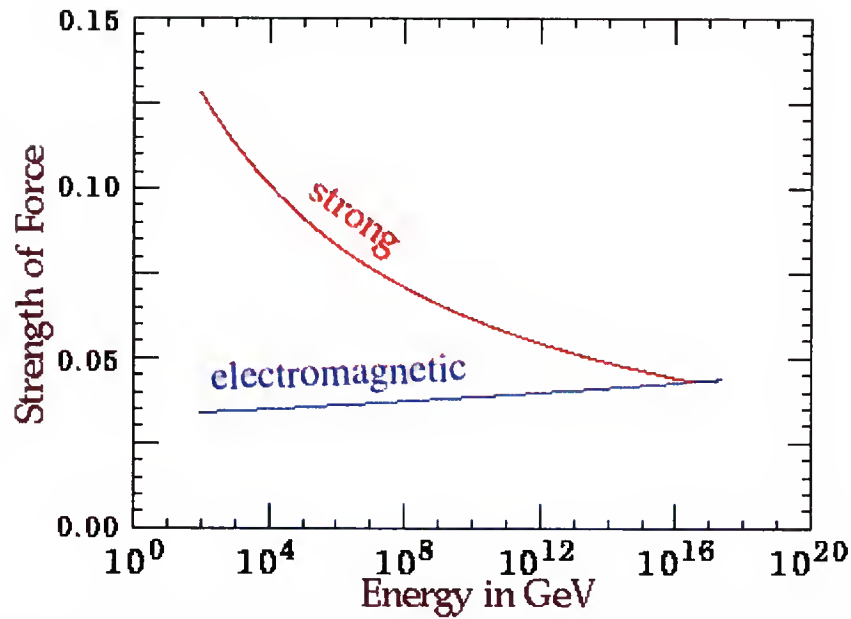


Figure 1-2: Relative strength of the strong and electromagnetic forces

1.4 Hadron Hadron Interactions

From a phenomenological point of view, we can consider two hadrons colliding at high energies, such as we have at the Tevatron Collider, to be colliding broad-band beams of quarks, antiquarks, and gluons. An average hard scattering event consists of a collection (or burst) of hadrons traveling roughly in the direction of each of the initial beam particles and two collections of hadrons with large transverse momentum. The two large transverse momentum jets are roughly back to back in azimuthal angle. One can use the topological structure of hadron-hadron collisions to study the “underlying event” [13, 22-24]. Of course, from a certain point of view there is no such thing as an “underlying event” in a proton-antiproton collision. There is only an “event” and one cannot say where a given particle in the event originated. On the other hand, hard scattering collider “jet” events have a distinct topology. On the average, the outgoing hadrons “remember” the underlying 2-to-2 hard scattering subprocess.

1.4.1 Parton Model and Large P_T Processes

Hadronic collisions which involve a short distance scattering can be described, in first approximation, by the Parton Model. Since the transferred momentum is the conjugate variable of the (quark-quark) impact parameter, larger Q^2 implies that partons have scattered at small distances where α_s is small. In order to be able to apply perturbation theory one needs a momentum transfer of about 10 GeV: from the uncertainty principle we calculate that the associated distance is in the order of 10^{-17}m . From the experimental point of view there is no certain way to separate such rare events but intuition suggests that large p_t final state particles should be a good indication and experiments fully support this.

We can picture this scattering process as a sequence of three different phases occurring at different time scales. Partons approach each other carrying a fraction, x , of the momentum of their parent hadrons. The transverse momenta of the partons are neglected. “Parton Distribution Functions” (PDF) $f_i(x, \mu^2)$ are so introduced giving the probability for parton i to have fractional momentum between x and $x + dx$ (μ is a factorization scale). Figure 1-3 is an example of such parton distribution functions. These functions are extracted from experimental data in deep inelastic scattering (DIS) of leptons on nucleons [25]. These parton distribution functions of the proton are a result of the work done by the H1 [26-28] and ZEUS [29] collaborations at HERA, and of the inclusive jet distribution by D0 [30] and CDF [31] collaborations at the Tevatron. As the data only cover a finite range of Q^2 , the evolution of such functions with Q^2 is computed, using perturbation theory, with the Altarelli-Parisi equation [32].

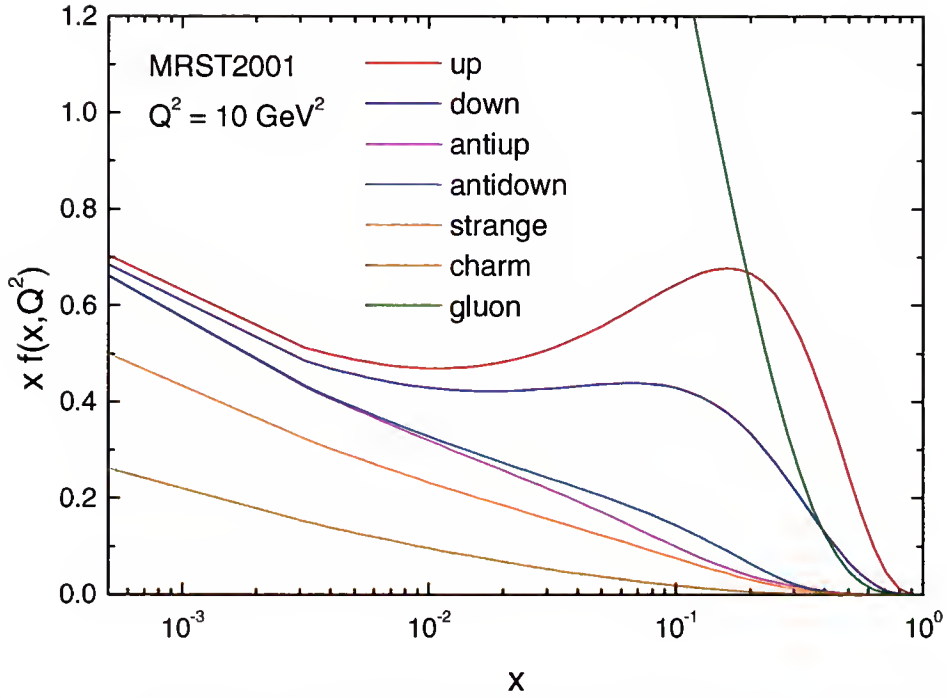


Figure 1-3: The parton structure functions extracted from an analysis of deep inelastic scattering data at $Q^2=10\text{GeV}^2$.

A hard collision then takes place between a pair of partons regarded as free particles. Predictions for jet production are given by folding the parton distribution functions with perturbatively calculated “two-body” scattering cross sections $\hat{\sigma}_{i,j}$. Any cross section of interest is calculated using equation (1-7).

$$\sigma = \sum_{i,j} \int f_i(x_1, \mu^2) f_j(x_2, \mu^2) \hat{\sigma}_{i,j} \left(x_1 P, x_2 P, \alpha_s(\mu_R^2), \frac{Q^2}{\mu^2}, \frac{Q^2}{\mu_R^2} \right) dx_1 dx_2 \quad (1-7)$$

Figure 1-4 shows the representation of an elementary “two-body” interaction between two partons in a $p\bar{p}$ collision producing a di-jet event.

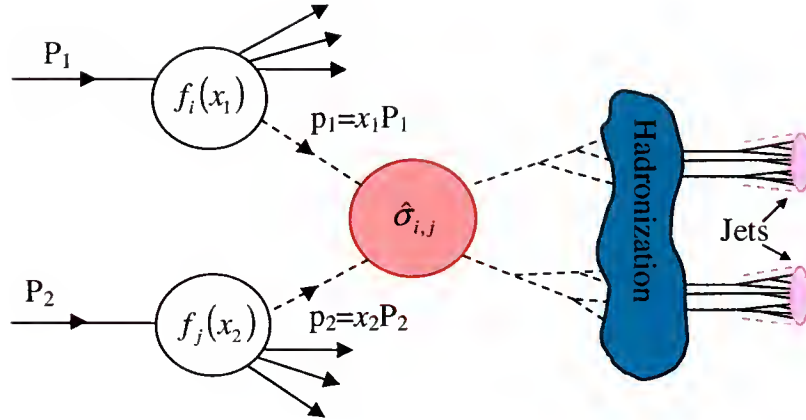


Figure 1-4: Hard “two-body” parton interaction producing a di-jet event in a proton-antiproton collision.

The factorization scale μ discriminates whether a parton, inside the incoming hadron, takes part or not in the hard scattering: if the momentum of a parton is greater than the scale μ , it contributes to the short-distance cross section (as the partons i and j in fig. 1-4); if its momentum is less than the scale μ , it is considered part of the hadron structure not involved in the hard interaction (spectator parton).

1.4.2 The “Underlying Event” in Proton-Antiproton Collisions: Pythia and Herwig

Fig. 1-1 illustrates the way QCD Monte-Carlo models simulate a proton-antiproton collision in which a “hard” 2-to-2 parton scattering with transverse momentum, $P_T(\text{hard})$, has occurred. The resulting event contains particles that originate from the two outgoing partons (*plus initial and final-state radiation*) and particles that come from the breakup of the proton and antiproton (*i.e.*, “beam-beam remnants”). The “underlying event” is everything except the two outgoing hard scattered “jets” and receives contributions from the “beam-beam remnants” plus initial and final-state radiation. The “hard scattering” component consists of the outgoing two jets plus initial and final-state radiation. Any measured observable of the underlying event necessarily receives contributions from

initial and final state radiation. It is possible to reduce these contributions by placing constraints on event topology and jet energy.

The “beam-beam remnants” are what is left over after a parton is knocked out of each of the initial two beam hadrons. It is the reason hadron-hadron collisions are more “messy” than electron-positron annihilations and no one really knows how it should be modeled. For the QCD Monte-Carlo models the “beam-beam remnants” are an important component of the “underlying event.” Also, it is possible that multiple parton scattering contributes to the “underlying event.” Figure 1-5 shows the way PYTHIA [33] models the “underlying event” in proton-antiproton collision by including multiple parton interactions. In addition to the hard 2-to-2 parton-parton scattering and the “beam-beam remnants,” sometimes there is a second “semi-hard” 2-to-2 parton-parton scattering that contributes particles to the “underlying event.”

For the hadronization process we have three types of non-perturbative contributions to consider: (1) representation of the incoming partons as constituents of the incident hadrons via parton distribution functions; (2) the conversion of the emitted partons into outgoing hadrons using quark and gluon fragmentation functions; and (3) the “soft” component to the “underlying event” generated by spectator partons. The “underlying event” receives contributions from the original $p\bar{p}$ system (“beam-beam remnants”), initial and final-state radiation, and possibly hadrons resulting from multiple parton interactions, as in Figure 1-5.

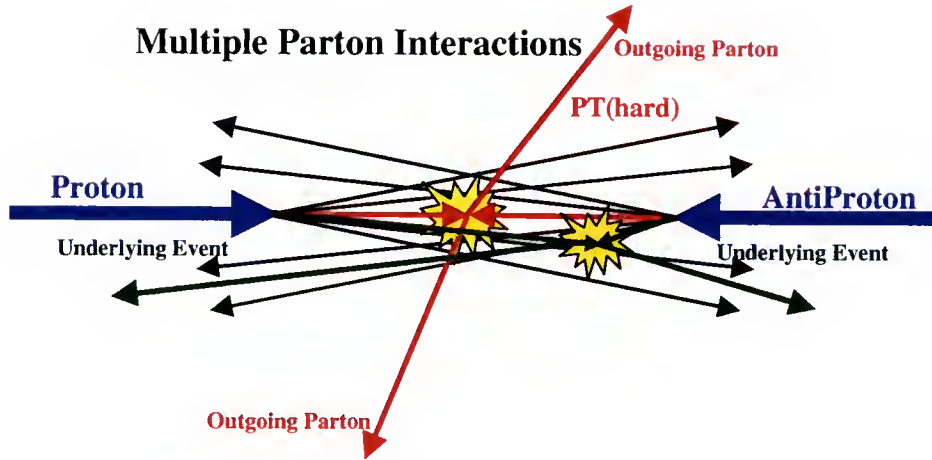


Fig. 1-5. Illustration of the way PYTHIA models the “underlying event” in proton-antiproton collision by including multiple parton interactions. In addition to the hard 2-to-2 parton-parton scattering with transverse momentum, $P_T(\text{hard})$, there is a second “semi-hard” 2-to-2 parton-parton scattering that contributes particles to the “underlying event”.

Both of the QCD Monte Carlo models, HERWIG [34] and PYTHIA, include a “soft” underlying event structure that is modeled by a parameterization of minimum bias data, and creates jets from the beam remnants. This is an imperfect model of the “underlying event,” since it always contains particles, yet the soft underlying event can be absent, as shown by the finite survival probabilities for inelastic events with large rapidity gaps [35-38]. PYTHIA has added multiple parton interactions to enhance the activity of the “underlying event,” and Tune A [22-23] was specifically tuned to fit the “underlying event” in the Run I data.

The QCD perturbative 2-to-2 parton-parton differential cross section diverges as the transverse momentum of the scattering, P_T , goes to zero (see figure 1-1). PYTHIA uses a tunable parameter to prevent divergences at low P_T . Tune A was tuned to fit the Run I data, and the low P_T region was an area of focus. HERWIG does not allow for this, and a suitable P_T cutoff must be chosen. We use $P_T > 5 \text{ GeV}/c$ for all 2-to2 hard scattering events in HERWIG.

CHAPTER 2 ACCELERATOR AND DETECTOR

The Tevatron [39] $p\bar{p}$ Collider is currently the world's highest energy particle accelerator in operation. It is the largest in a chain of five accelerators at the Fermi National Accelerator Laboratory (FNAL, Fermilab) and is capable of producing proton-antiproton collisions at a center of mass energy $\sqrt{s}=1.96$ TeV. The Collider Detector at Fermilab (CDF) [40] and D0 [41] are the multipurpose detectors built at collision points to exploit physics at the Tevatron. The analysis presented in this dissertation is based on the data sample collected by CDF during the 2001-2004 (Run II) running period of the Tevatron.

2.1 The Accelerator Complex

The Accelerator Complex at FNAL (see Figure 2-1) uses multiple stages of acceleration to achieve proton-antiproton collisions at a center of mass energy $\sqrt{s}=1.96$ TeV. The protons used in the collisions originate from ionized Hydrogen gas molecules. These H^+ ions are first accelerated to 750 KeV in the Cockcroft-Walton accelerator. They are then fed into the Linac, a 150m long series of nine radio-frequency (RF) cavities which produce an electric field that rapidly changes direction. In this linear accelerator the H^+ ions are brought to 400 MeV. Subsequent to this stage, the beam is focused and made to collide with a thin fixed carbon target which affects the loss of two electrons per ion. The denuded H^+ ions are now the protons that will ultimately be collided or used to make the anti-protons at the Target Station.

The 75.5 m radius Booster is a fast cycling proton synchrotron of conventional magnets (used to steer and focus the beam) and an RF cavity (used to accelerate the beam). The accelerated protons leave with kinetic energy of 8 GeV and are then injected

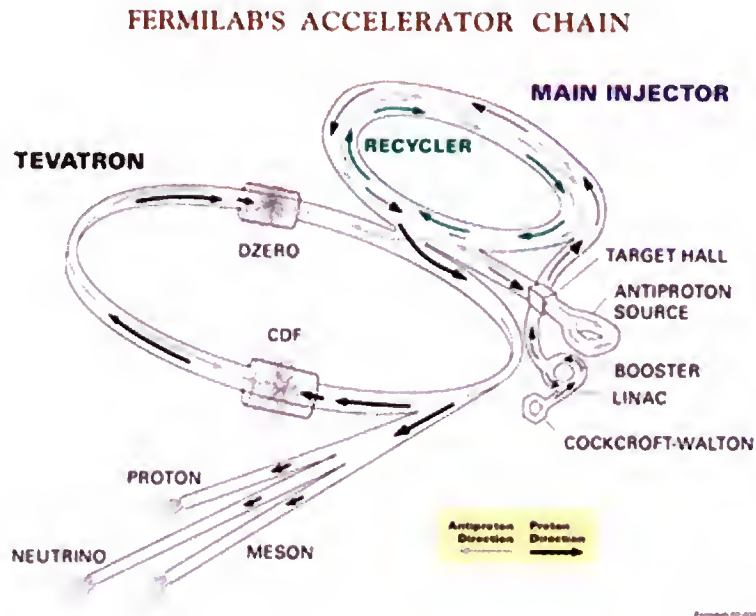


Figure 2-1: Overview of the accelerator complex at Fermilab. H^- ions are injected into the linac from the Cockcroft-Walton, to travel to the Booster, then to the Main Ring, and finally to the Tevatron. Some protons are extracted from the Main Ring and are used to make anti-protons. The anti-protons are re-injected into the Main Ring and then into the Tevatron. The final $p\bar{p}$ center of mass energy is $\sqrt{s} = 1.96$ TeV.

into the Main Ring. These protons are then further accelerated to 150 GeV in the Main Injector, and finally brought to 980 GeV by the Tevatron. The Tevatron was the world's first superconducting synchrotron. The beam is guided around the closed path by dipole magnets. As the beam energy is ramped up by RF cavities from 150 GeV to 980 GeV, the bending magnetic fields and the RF frequency must be carefully synchronized to ensure beam stability. The transverse motion of the beam is stabilized by quadrupole magnets that take advantage of magnetic field gradient technology.

Anti-protons are produced by sending 120 GeV protons from the Main Injector to a nickel target. From the resulting shower of particles, antiprotons of around 8 GeV are selected and sent to the Debuncher and Accumulator Rings where RF and stochastic cooling systems are used in the momentum stacking process. Once a 'stack' has been collected the antiprotons are sent back to the Main Injector, accelerated to 150 GeV and put into the Tevatron, circulating counter to the proton bunches. For every million protons that hit the target, only about twenty 8 GeV anti-protons will be stacked into the Accumulator.

The Recycler is placed directly above the Main Injector beamline. This dual function system serves as a post Accumulator storage ring and as a recycler for the antiprotons left over at the end of a store¹. These recycled anti-protons can be mixed with those from the Accumulator and then accelerated to 150 GeV in the Main Injector and then injected into the Tevatron.

Once both beams are at the maximum energy they are focused and brought to collision at the two interaction points, one of which is at the center of the CDF detector. The luminous region has a Gaussian dispersion of around 30 μm transverse to the beam direction, and a length along the beam direction of around 30 cm.

The beams typically circulate for 12-18 hours during which time the luminosity falls approximately an order of magnitude. During this time antiproton are continuously stacked. When the stack is sufficiently large and the luminosity has significantly decayed, the beam in the Tevatron is dumped and new bunches are injected.

¹ A store refers to the period of time when proton-antiproton collisions are taking place. Stores can be selectively terminated when luminosity has reached a minimum or a new stack of antiprotons is ready. Alternatively, a store can end with a magnet quench or other problem.

The instantaneous luminosity L is given by equation 2-1

$$L = \frac{f N_p N_{\bar{p}}}{A}, \quad (2-1)$$

where f is the frequency of bunch crossings, N_p and $N_{\bar{p}}$, are the number of protons and antiprotons, respectively, per bunch, and A is the effective area of the crossing beams. The current status of the luminosity is shown in figure 2-2, and the integrated luminosity delivered to tape is shown in Fig. 2-3.

Parts of the Fermilab accelerator complex are 20 years old and there have been some setbacks since the upgrades to take the Tevatron from 1.8 TeV to 1.96 TeV. However, the initial instantaneous luminosity of stores has been steadily increasing. The

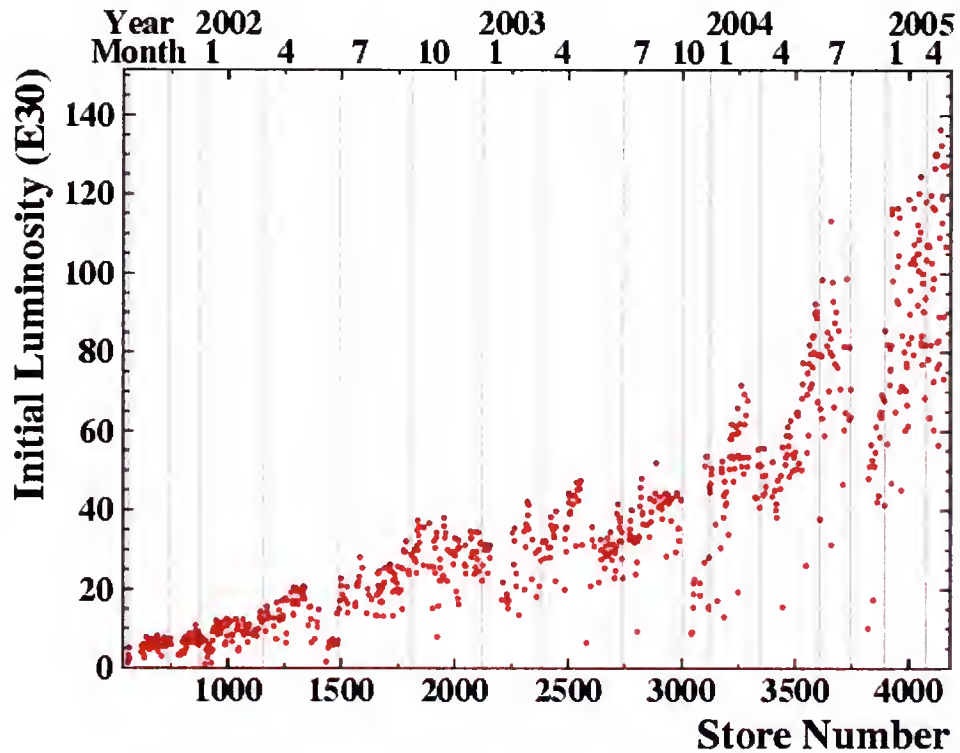


Figure 2-2: Run II instantaneous initial luminosity

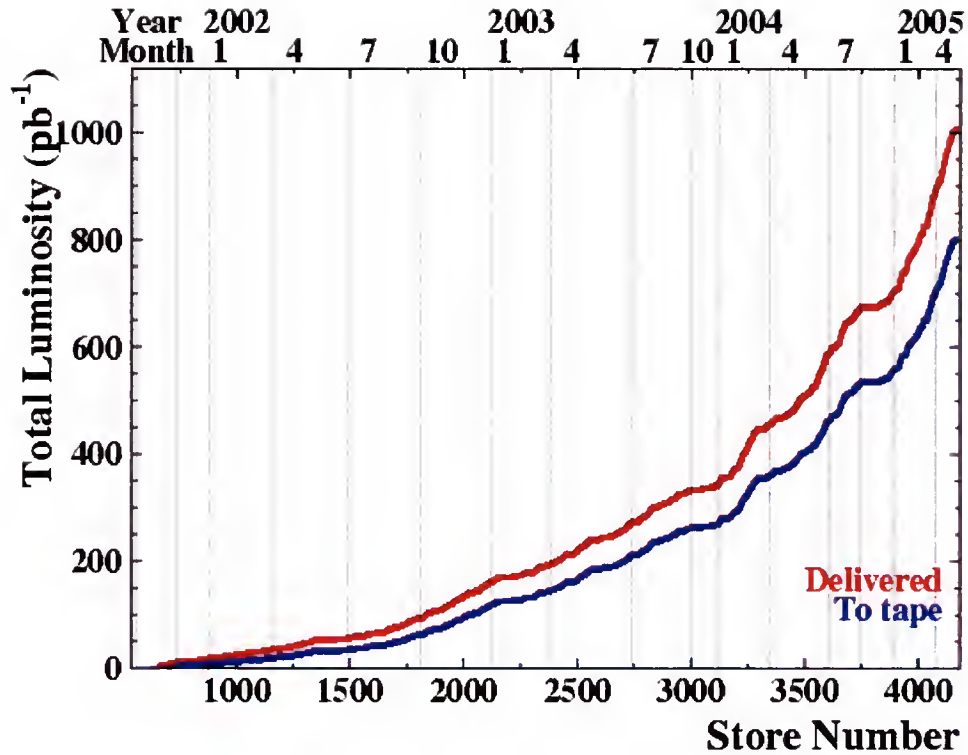


Figure 2-3: Run II integrated luminosity

projected goal for all of Run II is $4\text{--}8\text{ fb}^{-1}$ by the time LHC is ready to begin taking data (circa 2009).

The total number of events n in a scattering process is proportional to the luminosity and the cross section σ of the process,

$$n = L\sigma \quad 2-2$$

We can get a rough sense of the reach for new physics and the challenge of enhancing signal and suppressing background by considering the following examples. At a center-of-energy of 1.96 TeV, we have:

$$\sigma(p\bar{p} \rightarrow \text{anything}) \approx 75\text{mb} \quad 2-3$$

$$\sigma(p\bar{p} \rightarrow t\bar{t} + \text{anything}) \approx 6\text{pb} \quad 2-4$$

With about 1fb^{-1} of delivered luminosity we should have seen 6000 top events. However, not every second of delivered luminosity is observed. Moreover, due to finite capabilities

in data storage not every observed event can be recorded. The task of observing the events fall on the Detector and the job of selecting events to be recorded is given to the trigger system.

2.2 The Collider Detector at Fermilab

The Collider Detector at Fermilab (CDF) is a large, multilayered general purpose detector designed to study a wide range of processes occurring in proton-antiproton collisions. Figure 2-4 is a schematic drawing of the approximately 5000 ton, 10 m high, and 27 m long detector. The CDF is cylindrically symmetric about the beam axis and has a forward-backward symmetry in its tracking, calorimetric, and muon systems. Figure 2-5 shows an elevated view in which the tracking system is seen to be contained in a solenoid coil. The calorimetry and muon systems are outside the solenoid. These subsystems are described in more detail below.

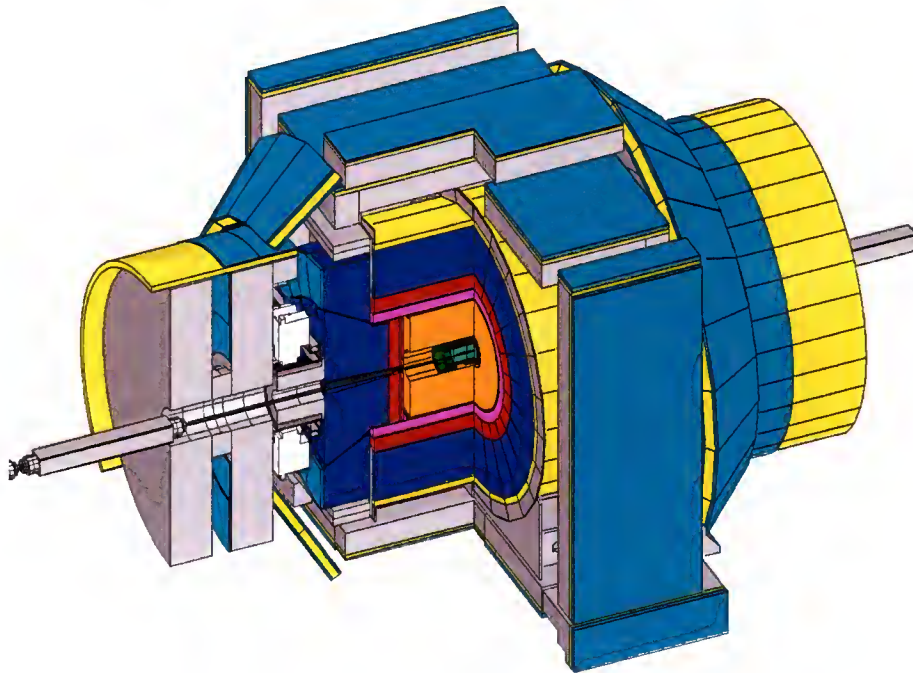


Figure 2-4: Solid cutaway view of the CDF II detector.

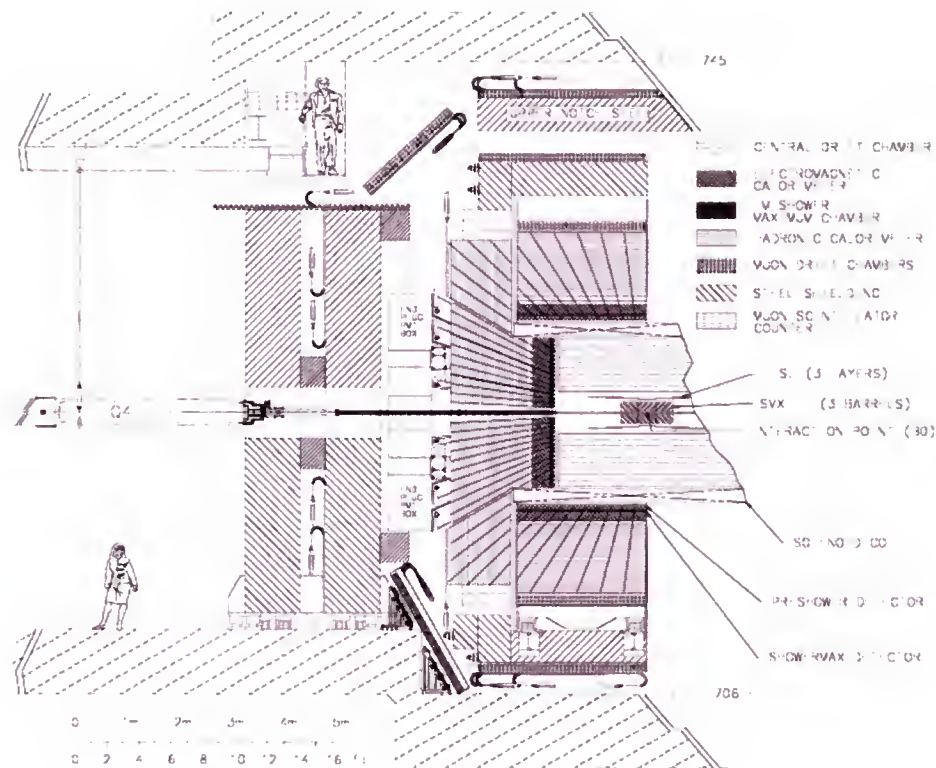


Figure 2-5: Elevation view of the CDF II detector.

2.2.1 The CDF Coordinate System

The geometric center of the detector serves as the nominal interaction point (0,0,0). Figure 2-6 shows the overall CDF coordinate frame, in both cylindrical and Rectangular systems. The positive z-axis corresponds to the proton beam direction, the positive y-axis points vertically upward, and the positive x-axis points radially outward from the center of the Tevatron ring. In the cylindrical system the azimuthal angle ϕ is measured about the beam axis from the positive x-axis. The polar angle θ is defined as the angle measured from the positive z-axis.

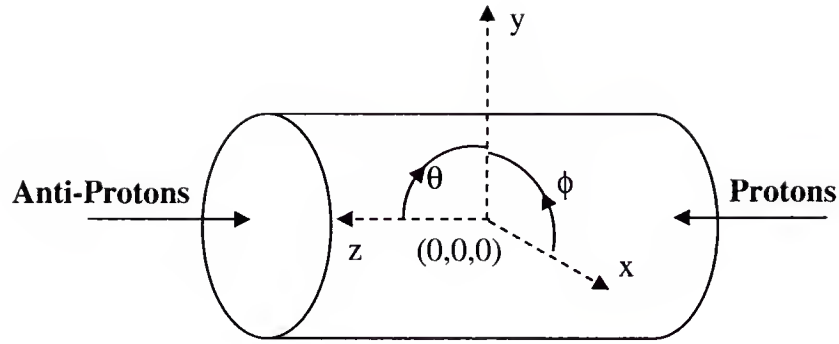


Figure 2-6: The CDF coordinate system.

The incident proton and anti-proton have no transverse momentum and they have equal and opposite longitudinal momentum, therefore the total momentum of the products of the collision would sum to zero in a full 4π solid angle experiment. However, some space must be left for the beam pipe. Those particles from the collision that travel at very small angles, two degrees or less (such as hadrons from spectator quark hadronization), will fly down the beam pipe completely missing the detectors. Such unmeasured particles will not carry much transverse momentum, but they may carry significant amounts of longitudinal momentum. For this reason, longitudinal momentum will not balance in the detector, but the transverse momentum will, to the detectors accuracy.

For these reasons, rather than using the total energy E and total momentum p , we generally use the transverse energy $E_t = E \times \sin(\theta)$ and the transverse momentum $p_t = p \times \sin(\theta)$. In the large energy collisions found at CDF, the E_t and p_t of particles in the event are nearly equally. However, by convention we use E_t when referencing energy deposited in the calorimeters, so that it is understood that the angle θ refers to the geometric center of the detector. Alternatively, p_t usually refers to the transverse momentum of a particle determined in a tracking chamber so that the angle θ

reflects the true interaction vertex. It is common to use the pseudorapidity in place of the polar angle θ .

The “natural” kinematic variables for hadron collisions are pseudorapidity, transverse momentum, and azimuthal angle since the shapes of their distributions are invariant under a Lorentz boost. Transverse momentum and azimuthal angle are invariant to Lorentz transformations along the z axis and the pseudorapidity is simply additive.

The major components of the CDF detector are arranged cylindrically around the interaction point. Closest to the beamline are the layers of silicon, providing high-precision tracking and vertexing in the r - ϕ plane. Next is a wire drift chamber that provides measurements of momentum and spatial parameters of a particle's trajectory (track). The tracking subsystem is embedded inside a superconducting solenoidal magnet that produces a 1.41 Tesla magnetic field. Energy measurements of jets, electrons, photons, and hadrons are made by the combined calorimetry systems: central, plug and forward electromagnetic (EM) and hadronic calorimeters (HAD). Muons are identified by the presence of a track in the muon chambers matched to a track in the central tracking chamber. Because of the long lifetime and high penetration of muons, the muon chambers are placed outside of the hadronic calorimeters, after a steel absorber to eliminate any electromagnetic and hadronic showers. In front of the backward and forward calorimeters is a plane of scintillation counters called “Beam-Beam Counters” (BBC). They provide a minimum bias trigger for the detector and are also used as the primary luminosity monitor. The layout of these detectors is shown in figure 2-7, which depicts one quadrant of the cross-section through the detector.

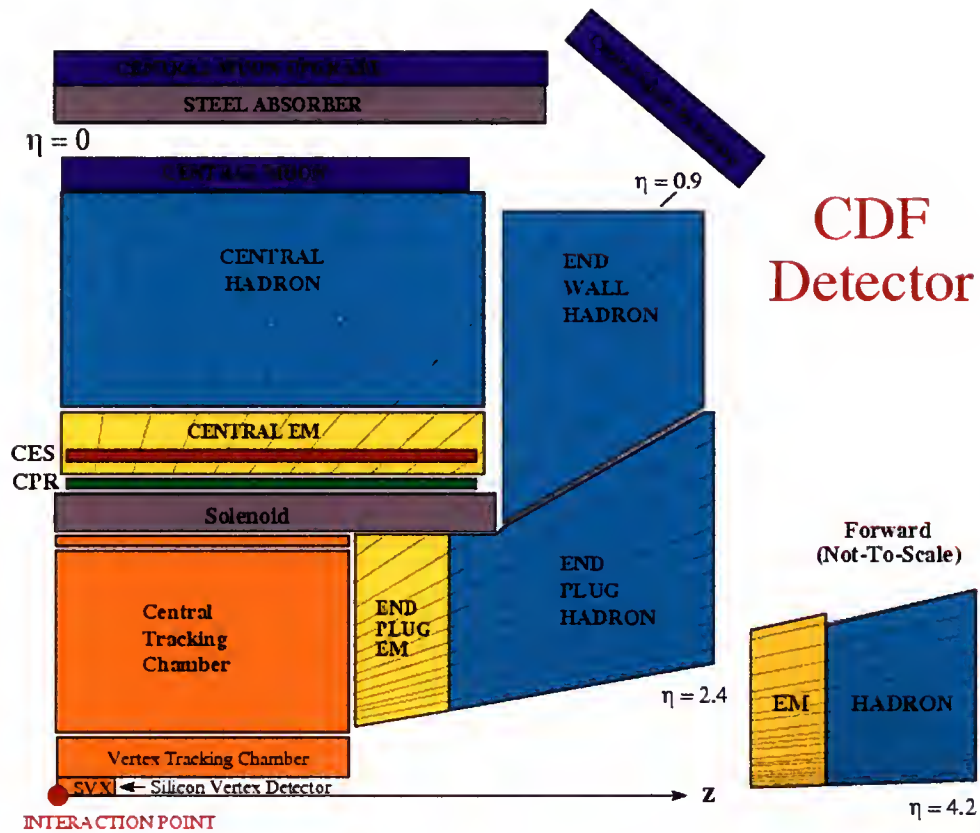


Figure 2-7: A quarter of the CDF detector. Only the central and end-plug subsystems are shown.

2.2.2 Tracking

The CDF uses silicon strip detectors (L00 + SVXII + ISL) and a drift chamber (COT) for charged-particle track reconstruction and vertex finding. The tracking systems are inside a superconducting solenoid of radius 1.5m that provides a 1.41 Tesla magnetic field parallel to the beam axis. The magnetic flux is returned through a steel yoke. The tracking volume and the endplug calorimeters are shown in figure 2-8. The yoke also functions as a support to the calorimeters located radially outside the solenoid. The silicon system and drift chambers were redesigned and completely rebuilt between Run I and Run II of the Tevatron.

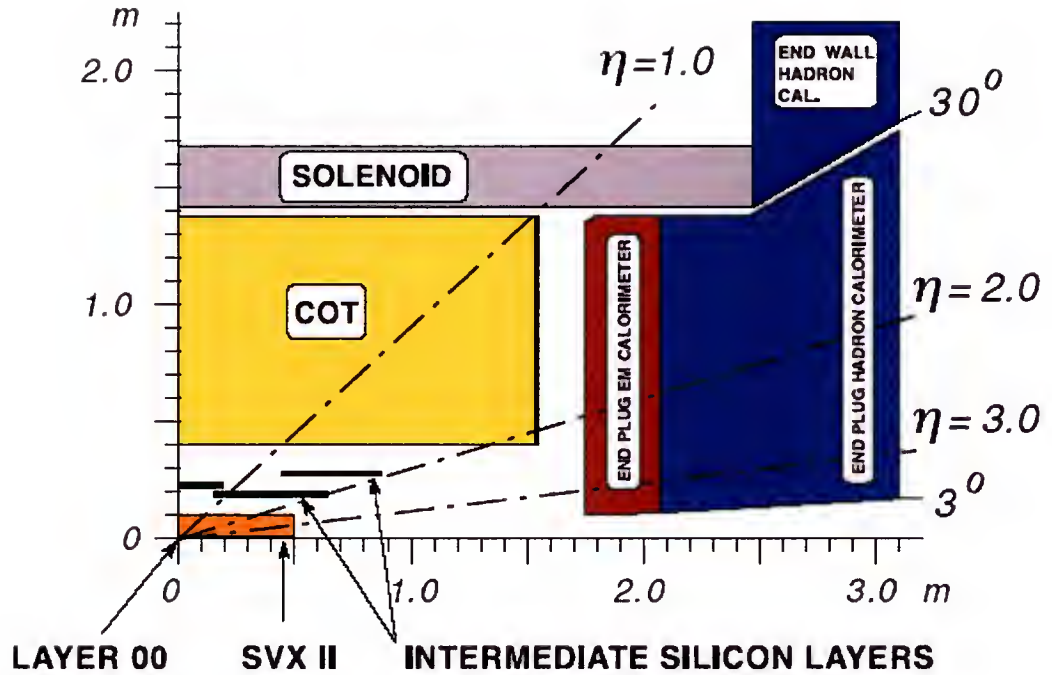


Figure 2-8: The CDF II tracking volume.

In the silicon tracker, as charged particles move through the ‘depletion layer’ created in a biased p-n semiconductor junction, they create electron-hole pairs that drift to be collected at the surfaces. This induces a signal on metal stripes that have been deposited on the surface and connected to readout amplifiers. Figure 2-9 shows a schematic layout of the silicon tracking system.

Layer 00 (L00) is mounted on the beam pipe, 1.6 cm from the beam axis, and consists of 8 single sided microstrip silicon detectors. These detectors cover the beam pipe for about 40 cm in each direction about $z = 0$ [42]. Outside the L00, the ‘Silicon Vertex Detector’ (SVXII) occupies the volume between 2.4 and 10.6 cm from the beam axis and covers a total length of 96 cm along the z coordinate. The SVXII system consists of five double sided microstrip silicon layers [40]. Three of these layers provide track position in the r - ϕ plane from the readout of one side (microstrips parallel to the

beam axis) while the z coordinate is determined by the other side (microstrip perpendicular to the beam axis). The other two other layers have their microstrips tilted in such a way as to provide a 3-D track reconstruction with an approximately uniform efficiency. The Intermediate Silicon Layers (ISL) Detector is placed in the region between SVXII and the central tracking system [40]. Figure 2-9 shows the position of the ISL detector. The layers are in the radial range $20 < r < 30$ cm and extend to $|z| = 65$ cm for the inner layer and $|z| = 87.5$ cm for the outer layer. The ISL covers the range of pseudorapidity for $|\eta| \leq 2$. Figure 2-10 shows an end view of the three components of the silicon microstrip detector system.

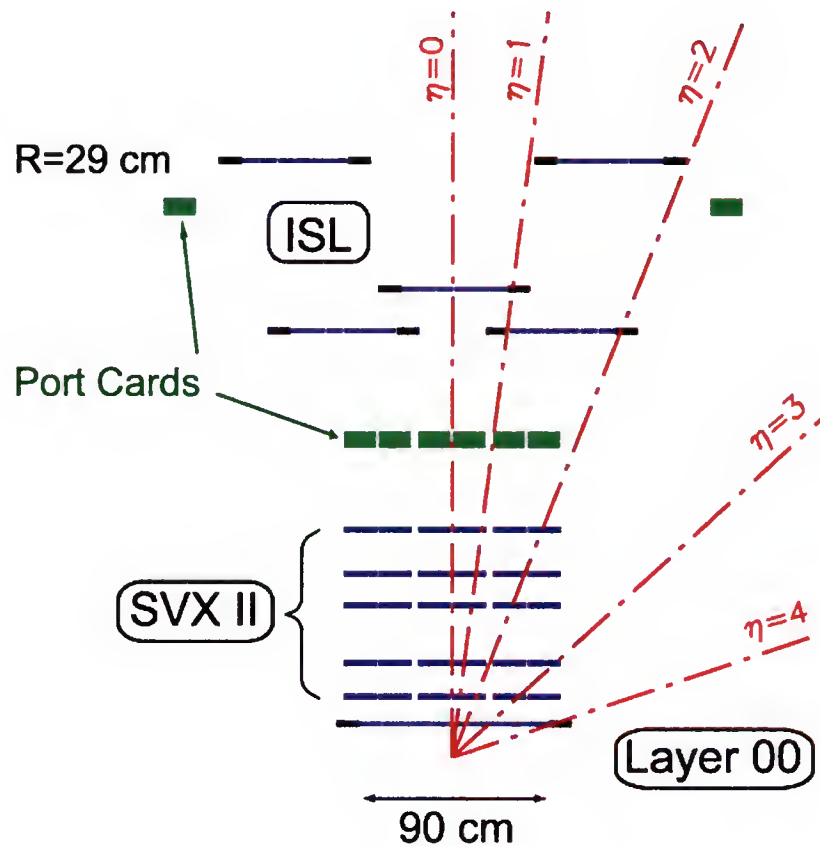


Figure 2-9: Schematic layout of the silicon tracking system. The innermost layer, Layer00 consists of 6 sensors in z .

The Central Outer Tracker (COT) is a large cylindrical drift chamber used to determine precise position measurements [40]. The tracking at large radii in the central rapidity region ($|\eta| < 1$) is done with a large open cell, cylindrical drift chamber using a readout that can record multiple hits from each sense wire. The active volume of the COT spans 310 cm in the beam (axial) direction, z ; between 43.4 cm and 132.3 cm in radius, r ; and the entire azimuth, ϕ . The COT provides 96 measurement layers, organized into alternating axial and $\pm 2^\circ$ stereo superlayers. Sense wires and potential wires are alternated and arranged in 8 ‘superlayers’ as shown in Figure 2-11, each consisting of 12 layers of sense wires. Within each superlayer are ‘cells’, bounded by field-shaping sheets. The cells are angled at 35° to the radial direction to compensate for the Lorentz

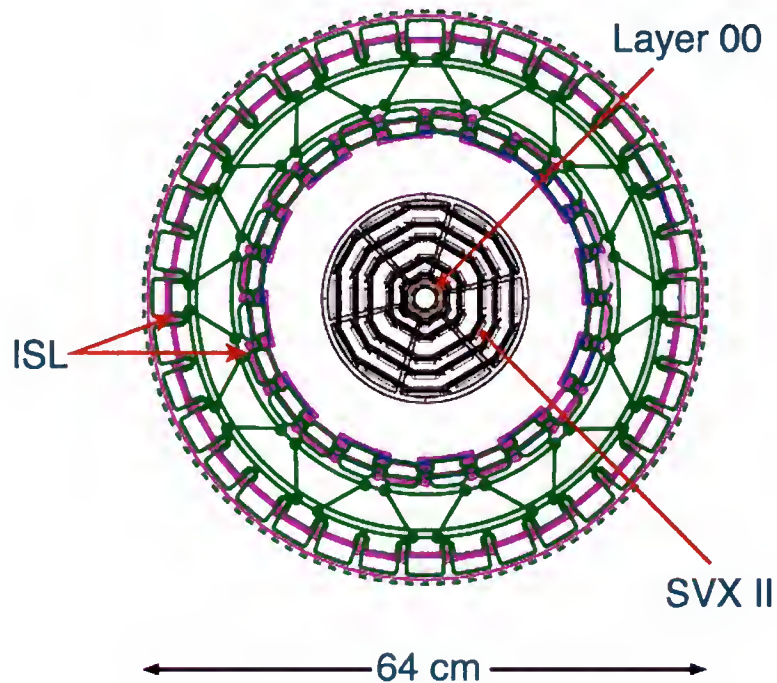


Figure 2-10: End view of the three components of the silicon microstrip detector system.

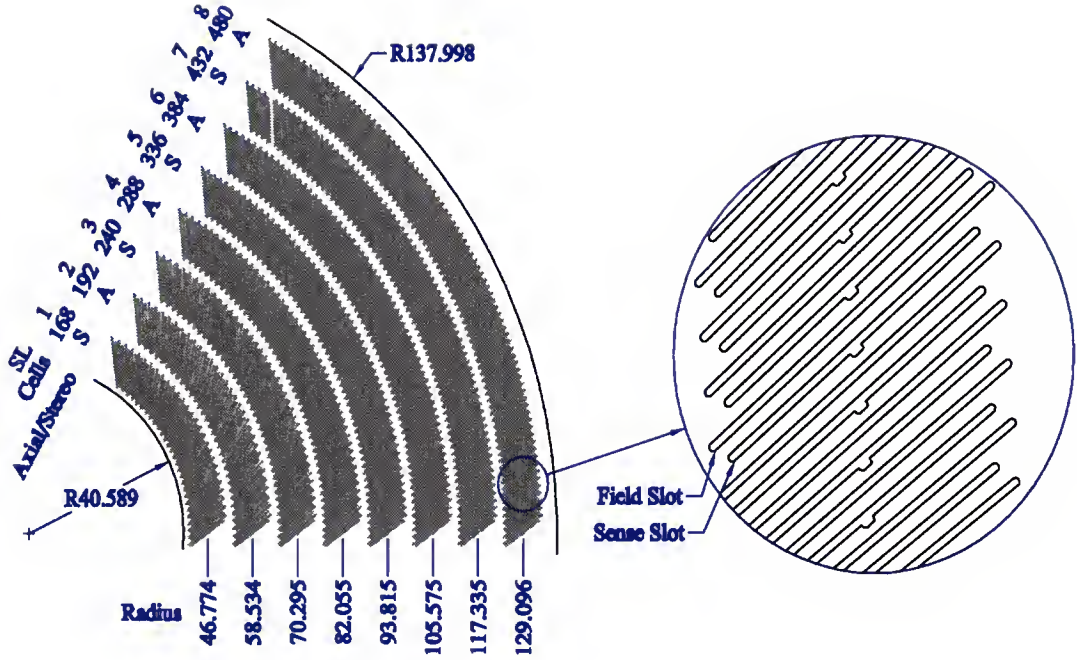


Figure 2-11: The COT sense wires and potential wires are alternated and arranged in 8 ‘superlayers’.

angle of the drifting charged particles. There is a ‘spacer’ at $z = 0$ that results in a lower tracking trigger efficiency at $\eta = 0$. The chamber is filled with a 50:50 mixture of Argon/Ethane and a small amount of alcohol. The hit position resolution is approximately $140\mu\text{m}$ and the momentum resolution $\sigma(p_T)/p_T^2 = 0.0015(\text{GeV}/c)^{-1}$. A reconstructed track provides accurate information in the r - ϕ view for measurement of transverse momentum, p_T , and substantially less accurate information in the r - z view for the measurement of η .

2.2.3 Calorimeters

As charged particles progress through the calorimeters they interact and develop characteristic ‘showers’. Different size and thickness plastic scintillator and absorber layers are alternatively stacked forming the electromagnetic calorimeters (allowing for the energy measurement of photons and electrons) and the hadronic calorimeters

(measuring hadron energies). The primary particle produces a shower of secondary particles inside the absorber. The shower particles deposit a fraction of their energy in the sampling material producing a light signal read by photomultipliers (PMTs) through wavelength shifting (WLS) light guides or optical fibers.

As can be seen in figure 2-7, the CDF calorimeters are physically separated into two sections: the central region, cylindrical about the beam line and covering $|\eta| < 1$; and the forward or ‘end plug’ regions, covering $1.1 < |\eta| < 3.6$. The principal components of the central calorimeter are the central electromagnetic (CEM) [43] and the central hadronic (CHA) [44] compartments. Both the CEM and CHA are retained from Run I. They are segmented in η and ϕ with a projective “tower” geometry, shown in action in Fig. 2-12. In each tower the electromagnetic compartment is backed by the hadronic one, both readout by different PMTs.

The central calorimeter is azimuthally arranged in 48 physically separated 15° wide wedges each segmented in η into ten towers, shown in figure 2-13. Each tower subtends $0.11 \times 15^\circ$ in $\phi \times \eta$. The central electromagnetic calorimeter (CEM) is overlapped by a hadronic section split into two parts, the central hadronic calorimeter (CHA) and the wall hadronic calorimeter (WHA). The CEM covers $0 < |\eta| < 1.1$ and uses lead sheets interspersed with polystyrene scintillator as the active medium and employs phototube readout. The CHA covers $0 < |\eta| < 0.9$ and the WHA covers $0 < |\eta| < 1.3$. Both hadronic calorimeters use steel absorbers interspersed with acrylic scintillator as the active medium.

Located six radiation lengths deep in the CEM calorimeters, corresponding to the depth at which showers typically reach their maximum transverse extent is the Central

Electromagnetic Strip Detector (CES). The CES uses proportional strip and wire counters in a fine-grained array, as shown in Figure 2-14, to provide precise position (about 2 mm resolution) and shape information for electromagnetic cascades.

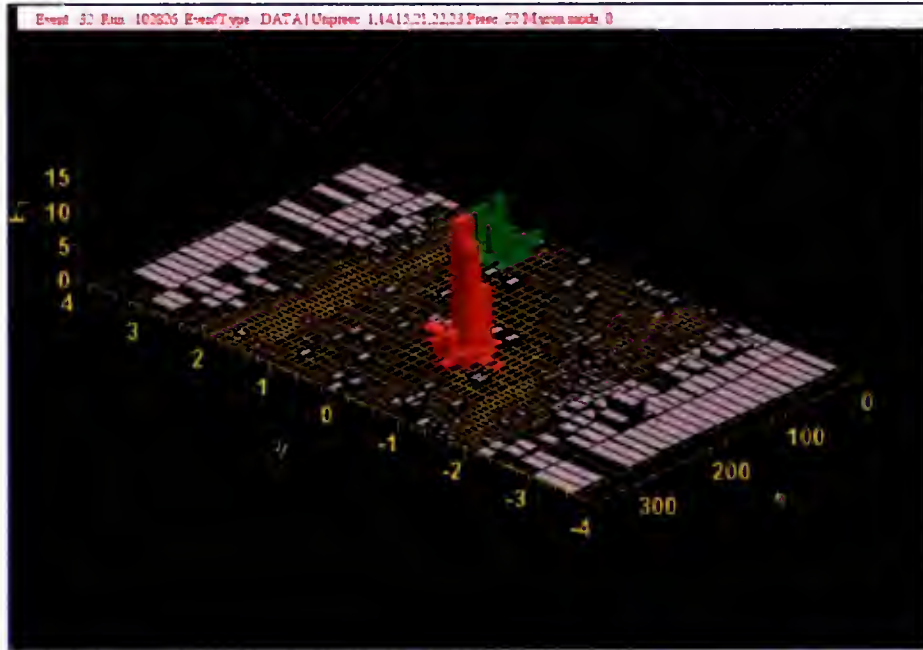


Figure 2-12: Calorimeter tower segmentation in η - ϕ space.

A further component of the central calorimeters is the central pre-radiator (CPR), a set of proportional chambers between the CEM and the magnet designed to help separate electrons and pions.

The plug calorimeters consist of the plug electromagnetic calorimeter (PEM) [45], newly built for the CDF Run II, and the plug hadronic calorimeter (PHA). Like the CEM, the PEM consists of a stack of lead and scintillator sheets read out by phototubes. At 6 times the radiation length in the PEM is the plug shower maximum detector (PES)[46].

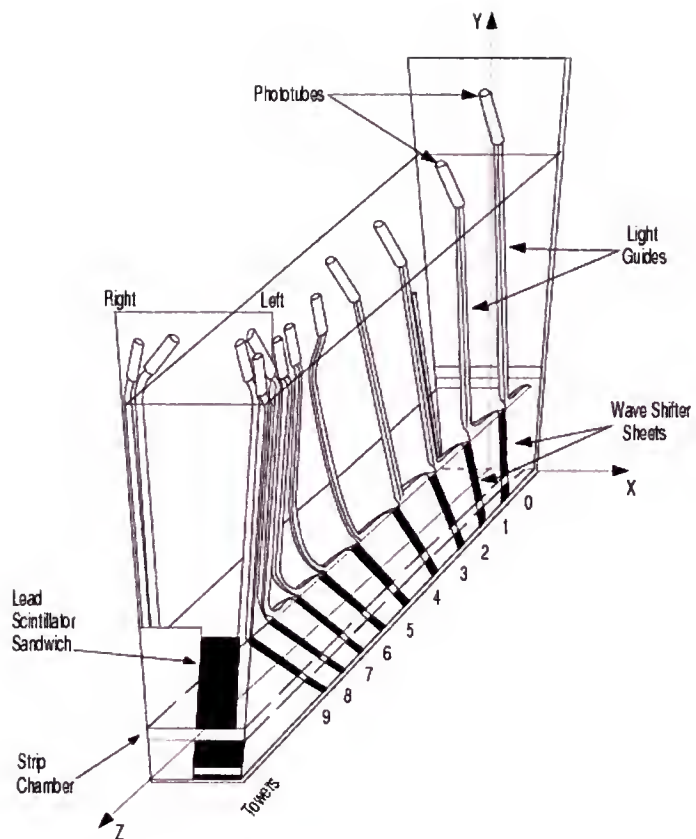


Figure 2-13: CEM/CES/CHA wedge.

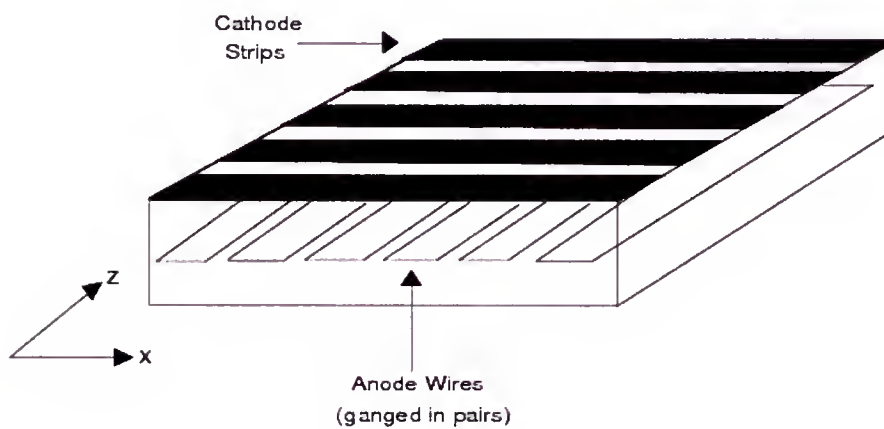


Figure 2-14: CES strip and wire.

Finally, the first layer of the PEM is read out separately and referred to as the plug pre-radiator (PPR). The PPR can help to distinguish between electron/photons and hadrons by indicating the extent to which the particle shower has already developed at the face of the calorimeter.

2.3 The CDF Trigger System

The inelastic proton-antiproton cross section at $\sqrt{s} = 1.96$ TeV is about 60 mb ($\sim 60 \times 10^{-27} \text{cm}^2$). For a typical instantaneous luminosity of about $1.2 \times 10^{32} \text{cm}^{-2}/\text{s}$ we get ~ 7.6 million inelastic collisions per second at CDF. The CDF readout electronics and event storage system is not capable of recording events at such a high rate. Moreover, most of these events do not present a significant interest for the CDF physics program. The trigger system is used to select an event rate of 75 Hz from the 7.6 MHz (132 ns crossing) beam crossing rate [40]. The event rate is such that it is necessary to filter physically interesting events to be written to tape, and this achieved through a three-level trigger system, designed to be ‘deadtimeless’.

The Level-1 trigger is achieved with hardware. Based on preliminary information from tracking, calorimetry, and muon systems, the output of the 7.6 MHz Synchronous pipeline with a 5544ns latency at the first level of the trigger is used to limit the rate of accepted events to < 50 kHz. Each next trigger level examines fewer events but in greater detail. At the next trigger, with more refined information and additional tracking information from the silicon detector, the $\sim 20 \mu\text{s}$ latency, asynchronous 2 stage pipeline, reduces the acceptance further to ~ 300 Hz. The Level 2 algorithm uses the information about high momentum tracks and clustered calorimeter energy. If the accept decision is made by the trigger, then the information from all subsystems is read out and passed on

to Level 3. At level-2 many triggers are prescaled to reduce the total acceptance rates to a maximum of about 20 Hz that is the maximum that Level-3 can handle. This means that a predefined fraction of events that passed the trigger are considered to fail it. Prescaling is sometimes preferable over making tighter trigger cuts. This method allows us to record as many rare events as possible while still accepting other data at a reasonable rate. Some triggers can be dynamically prescaled. A dynamical prescale can be changed during the course of the run depending on the instantaneous luminosity: it will be large when the luminosity is high and small when the luminosity is low.

Level-3 consists of the event builder (EVB) and the Level-3 farm. The EVB assembles event fragments from level-1 and level-2 into complete events, and then the Level-3 farm runs a version of the full offline reconstruction code. This means that for example that fully reconstructed 3-dimensional tracks are available to the trigger decision. The Level-3 output rate is ~ 75 Hz and accepted events are written to tape in eight separate ‘streams’, sorted by the Consumer-Server Logger (CSL).

CHAPTER 3 JETS AT CDF

We have studied the “underlying event” in the Run 2 jet trigger data samples using the direction of the leading calorimeter jet (Midpoint, $R = 0.7$, $f_{\text{merge}} = 0.75$) to isolate regions of η - ϕ space that are sensitive to the “underlying event”.

Hadronization of the outgoing partons forms the jets we see experimentally. Jet algorithms are employed to map data onto jets with the idea that these jets are surrogates for the underlying energetic partons. In our theoretical picture, the partons produced by the hard scattering process evolve approximately within a narrow cone based on the parton showering and hadronization models. We use the Midpoint [47-49] jet algorithm in which the properties of the constituents of the jet(J) of cone radius R are defined by the following equations

$$k \in J : (\phi_k - \phi_J)^2 + (y_k - y_J)^2 \leq R^2 \quad 3-1$$

$$\phi_J = \sum_{k \in J} \frac{E_{T,k} \phi_k}{E_{T,J}}, \quad y_J = \sum_{k \in J} \frac{E_{T,k} y_k}{E_{T,J}} \quad 3-2$$

$$E_{T,J} = \sum_{k \in J} E_{T,k} . \quad 3-3$$

The MidPoint cone algorithm is based on the so-called “Snowmass Algorithm” which defines both the stability conditions and the properties of the jets [50].

The basic jet cone idea is that the constituents are nearby each other in simple geometric fashion. That is, the 3-momenta of the hadrons or partons lie within a cone defined by a circle in the angular variables (y, ϕ) , where $y = \frac{1}{2} \ln[(E + p_z)/(E - p_z)]$ is

the true rapidity and ϕ is the azimuthal angle. A stable jet cone has the property that the geometric center of the cone coincides with the E_T weighted centroid of the particles in the cone. Jet algorithms involve two distinct steps. The first is to identify the “constituents” that comprise the stable cone that is the jet. The second involves constructing the kinematic properties that characterize the jet. However, in practice the experimental implementation of the cone algorithm is more complicated.

It was imagined that the entire particle/tower list of each event would be searched for sets of final state particle/towers which satisfy the stability conditions. In practice this is not possible because of limited computing resources so a number of compromises have had to be made.

The Midpoint algorithm starts with an E_T ordered list of seed towers ($E_{tseed} >$ threshold), and forms “protojets” from every stable cone iterated around a seed tower. Seed Towers are simply calorimeter towers in which the energy deposition exceeds a certain predefined limit (usually set to 1 GeV) which is larger than the limit defined to include a tower in a jet (typically 0.3 GeV). A search for new protojets is carried out about the Midpoints in (y, ϕ) between all pairs of protojets with $\Delta R < 2 \times R_{cone}$. The Midpoint algorithm includes an iterative splitting/merging process applied to the P_T ordered list of jets to assign each particle to only one jet. Two jets are merged if the lower P_T jet shares greater than f_{merge} of its total P_T with the higher P_T jet. Otherwise the two jets are split and the individual particles are assigned to the closest jet centroid.

CHAPTER 4 MONTE-CARLO GENERATION AND CORRECTION FACTORS

4.1 Monte-Carlo Generation

In this analysis the data are corrected back to the particle level using PYTHIA Tune A [22, 23]. The corrected data are then compared with the particle level predictions of PYTHIA Tune A and HERWIG (*i.e.* generator level) at 1.96 TeV. PYTHIA Tune A (5.3.3nt) was generated with the minimum $P_T(\text{hard})$ values shown in Table 4-1 and HERWIG (5.3.3nt) was generated with the minimum $P_T(\text{hard})$ values shown in Table 4-2. Stntuples (5.3.3nt dev242) were created for the QCD group by Anwar Bhatti, Ken Hatakeyama, and Craig Group.

Table 4-1: PYTHIA Tune A (5.3.3nt) at 1.96 TeV.

$P_T(\text{hard})$ minimum	Events
0 GeV/c	3,093,106
10 GeV/c	1,039,093
18 GeV/c	4,285,687
40 GeV/c	4,228,873
60 GeV/c	992,087
90 GeV/c	1,497,108
120 GeV/c	2,068,377
150 GeV/c	1,488,786
200 GeV/c	1,042,280
300 GeV/c	1,045,314
400 GeV/c	1,043,634
Total	21,824,345

Table 4-2: HERWIG (5.3.3nt) at 1.96 TeV.

P_T(hard) minimum	Events
3 GeV/c	1,014,070
10 GeV/c	1,018,974
18 GeV/c	5,001,261
40 GeV/c	5,071,205
60 GeV/c	1,044,202
90 GeV/c	2,057,661
120 GeV/c	2,035,473
150 GeV/c	1,922,568
200 GeV/c	968,906
300 GeV/c	885,867
400 GeV/c	858,936
Total	21,879,123

Smooth curves have been drawn through the QCD Monte-Carlo predictions to aid in comparing the theory with the data. Fig. 4-1 shows an example of the fits to the Monte-Carlo results.

4.2 Correcting the Data to the Particle Level

We consider two methods for correcting the data from the detector level to the particle level. Method 1 is a “one-step” method in which PYTHIA Tune A and HERWIG are used to calculate the observables in Table 4-3 at the particle level (in bins of particle jet#1 P_T “*GEN*”) and at the detector level (in bins of calorimeter jet#1 P_T (uncorrected) “*CDFSIM*”). The detector level data, in bins of calorimeter jet#1 P_T

(uncorrected), are corrected by multiplying by a QCD Monte-Carlo correction factor, *GEN/CDFSIM*, as described in Table 4-4.

Table 4-3: Observables examined in the “transverse” region (see Fig. 6-2) as they are defined at the particle level and the detector level. Charged tracks are considered “good” if they pass the selection criterion given in Table 5-2. The mean charged particle $\langle p_T \rangle$ and the charged fraction $PT_{\text{sum}}/ET_{\text{sum}}$ are constructed on an event-by-event basis and then averaged over the events. There is one PT_{max} per event with $PT_{\text{max}} = 0$ if there are no charged particles.

Observable	Particle Level	Detector level
$dN_{\text{chg}}/d\eta d\phi$	Number of charged particles per unit η - ϕ ($p_T > 0.5 \text{ GeV}/c$, $ \eta < 1$)	Number of “good” charged tracks per unit η - ϕ ($p_T > 0.5 \text{ GeV}/c$, $ \eta < 1$)
$dPT_{\text{sum}}/d\eta d\phi$	Scalar p_T sum of charged particles per unit η - ϕ ($p_T > 0.5 \text{ GeV}/c$, $ \eta < 1$)	Scalar p_T sum of “good” charged tracks per unit η - ϕ ($p_T > 0.5 \text{ GeV}/c$, $ \eta < 1$)
$\langle p_T \rangle$	Average p_T of charged particles ($p_T > 0.5 \text{ GeV}/c$, $ \eta < 1$)	Average p_T of “good” charged tracks ($p_T > 0.5 \text{ GeV}/c$, $ \eta < 1$)
PT_{max}	Maximum p_T charged particle ($p_T > 0.5 \text{ GeV}/c$, $ \eta < 1$) $PT_{\text{max}} = 0$ for no charged particle	Maximum p_T “good” charged tracks ($p_T > 0.5 \text{ GeV}/c$, $ \eta < 1$) $PT_{\text{max}} = 0$ for no “good” charged track
$dE_T/d\eta d\phi$	Scalar E_T sum of all particles per unit η - ϕ (all p_T , $ \eta < 1$)	Scalar E_T sum of all calorimeter towers per unit η - ϕ ($E_T > 0.1 \text{ GeV}$, $ \eta < 1$)
$PT_{\text{sum}}/ET_{\text{sum}}$	Scalar p_T sum of charged particles ($p_T > 0.5 \text{ GeV}/c$, $ \eta < 1$) divided by the scalar E_T sum of all particles (all p_T , $ \eta < 1$)	Scalar p_T sum of “good” charged tracks ($p_T > 0.5 \text{ GeV}/c$, $ \eta < 1$) divided by the scalar E_T sum of calorimeter towers ($E_T > 0.1 \text{ GeV}$, $ \eta < 1$)

Method 2 is a “two-step” method. First PYTHIA Tune A is used to correct the P_T of the leading calorimeter jet. This is done by comparing the matching leading particle jet with the leading calorimeter jet. Then PYTHIA Tune A is used to calculate the observables in Table 4-3 at the particle level in bins of particle jet#1 P_T (*GEN*) and at the detector level in bins of calorimeter jet#1 P_T (corrected) (*CDFSIMcor*). The detector level data in bins of calorimeter jet#1 P_T (corrected) are corrected by multiplying by the QCD Monte-Carlo correction factor, *GEN/CDFSIMcor*. If the QCD Monte-Carlo

described the data perfectly and the detector simulation was exact then method 1 and method 2 would yield the same result. Differences between the two methods can be used as a measure of the systematic uncertainty in correcting the data to the particle level.

Table 4-4: Correction factors for Method 1. PYTHIA Tune A and HERWIG are used to calculate the observables in Table 4-3 at the particle level in bins of particle jet#1 P_T (GEN) and at the detector level in bins of calorimeter jet#1 P_T (uncorrected). The detector level data in bins of calorimeter jet#1 P_T (uncorrected) are corrected by multiplying by QCD Monte-Carlo factor, GEN/CDFSIM.

Particle Level Observable	Detector Level Observable	Response Factor	Correction Factor
GEN = Particle Jet#1 P_T Bin	CDFSIM = Calorimeter Jet#1 P_T Bin (uncorrected)	CDFSIM/GEN	GEN/CDFSIM

Fig. 4-2 and Fig. 4-3 show the particle level predictions from PYTHIA Tune A and HERWIG for average density of particles, $dN_{all}/d\eta d\phi$, for all particles with $|\eta| < 1$ in the “transverse” region as a function of the leading particle jet P_T for “leading jet” and “Back-to-back” events, respectively (see figure 6-3). It is interesting to note that HERWIG produces more particles in the “transverse” region than PYTHIA Tune A. Fig. 4-2 and Fig. 4-3 also shows the average charged particle P_{Tsum} density, $dP_{Tsum}/d\eta d\phi$, and the average charged particle $\langle p_T \rangle$ for particles with $|\eta| < 1$ in the “transverse” region for “leading jet” events as a function of the leading particle jet P_T . It is clear from these comparisons that HERWIG produces more “soft” particles than PYTHIA Tune A which will result in different “response” factors (see Table 4-4) at low leading jet P_T .

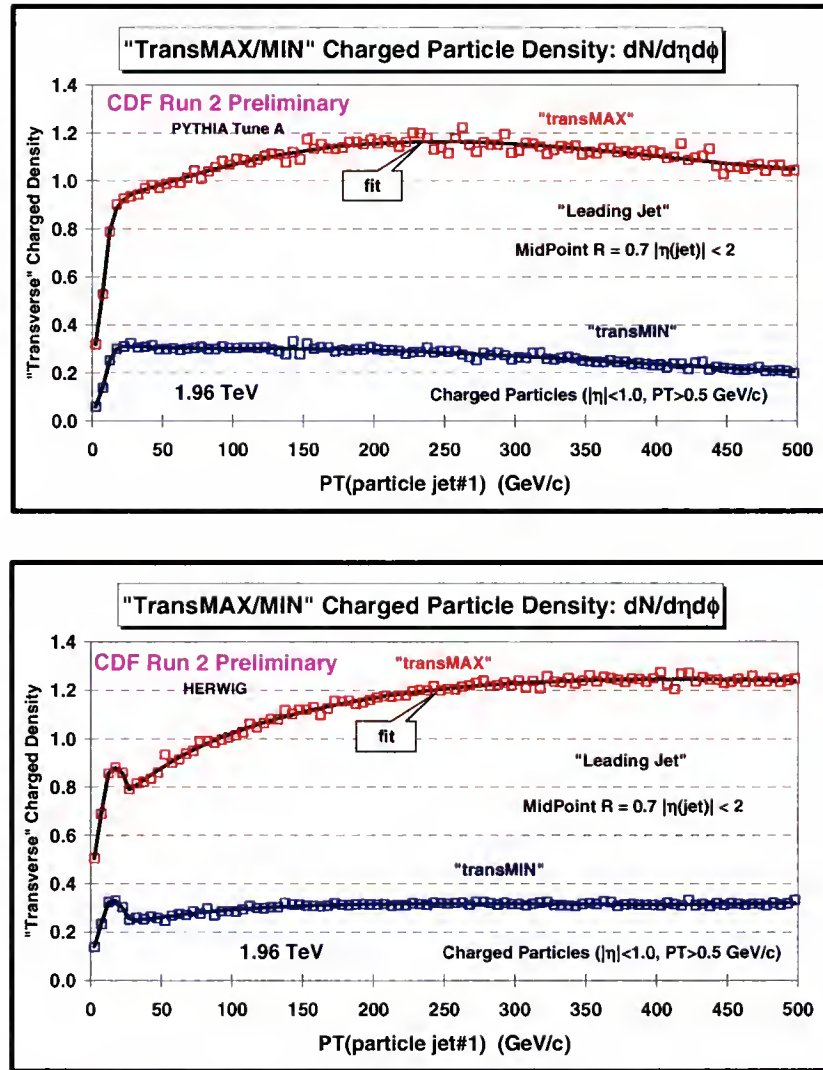


Figure 4-1: Example of fits to the QCD Monte-Carlo results. Shows the particle level predictions at 1.96 TeV for the density of charged particles, $dN_{\text{chg}}/d\eta d\phi$, with $p_T > 0.5$ GeV/c and $|\eta| < 1$ in the "transMAX" and "transMIN" regions for "leading jet" events defined in Fig. 6-3 as a function of the leading particle jet P_T for PYTHIA Tune A (*top*) and HERWIG (*bottom*).

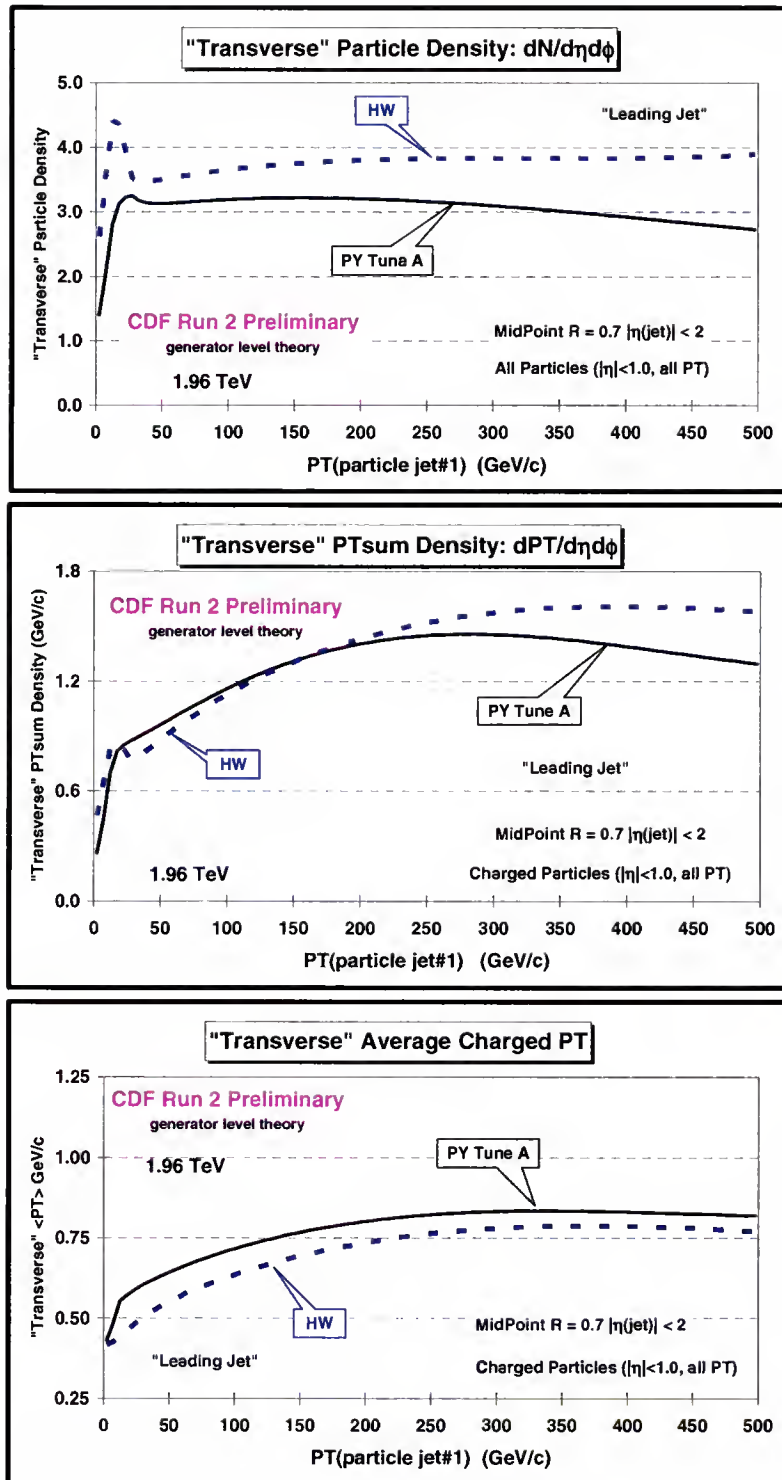


Figure 4-2: Particle level predictions from PYTHIA Tune A and HERWIG for average density of particles $dN_{all}/d\eta d\phi$ (*top*), the average charged particle P_T sum density, $dPT_{sum}/d\eta d\phi$ (*middle*), and the average charged particle $\langle p_T \rangle$ (*bottom*) for particles with $|\eta| < 1$ in the "transverse" region for "leading jet" events defined in Fig. 6-3 as a function of the leading particle jet P_T .

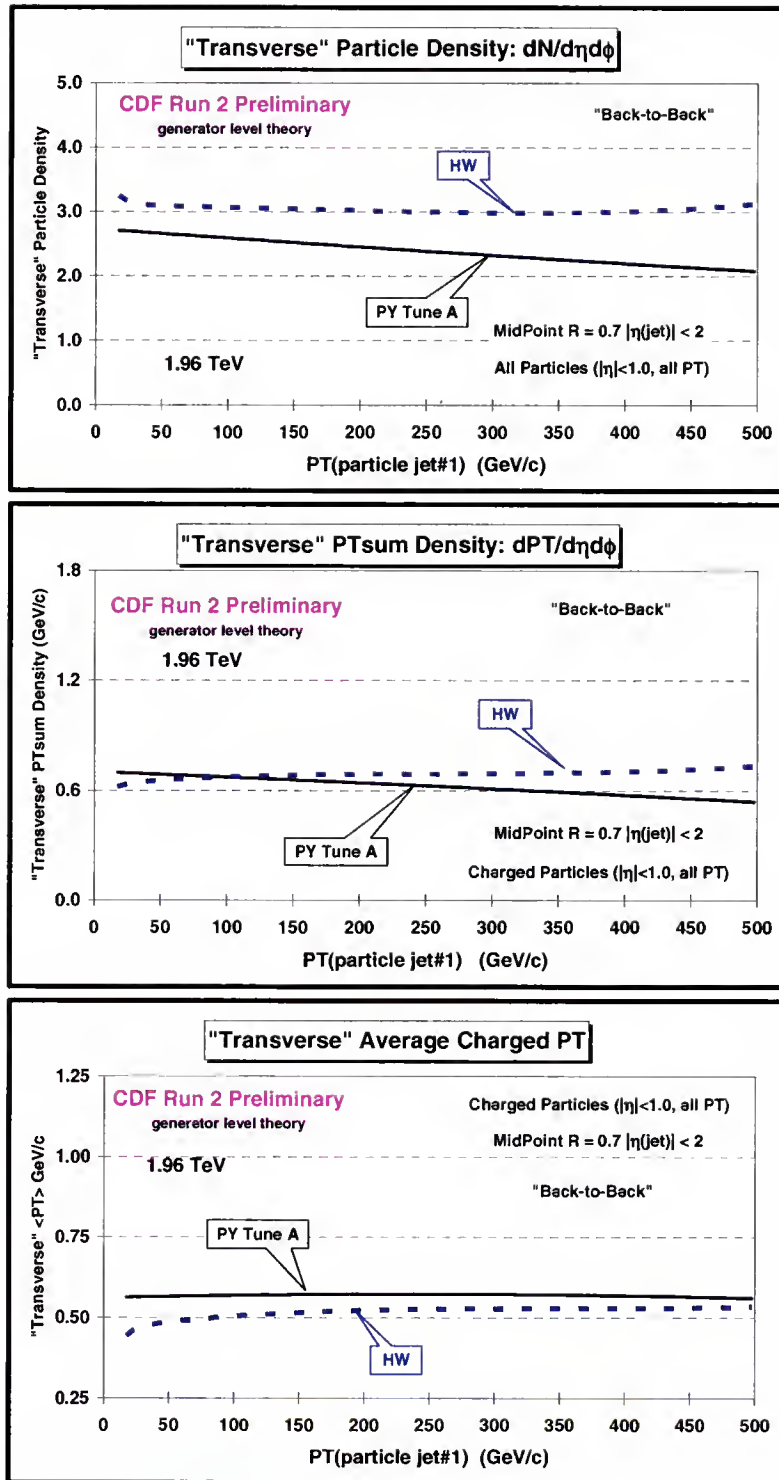


Figure 4-3: Particle level predictions from PYTHIA Tune A and HERWIG for average density of particles $dN_{all}/d\eta d\phi$ (*top*), the average charged particle PTsum density $dPT_{sum}/d\eta d\phi$ (*middle*), and the average charged particle $\langle p_T \rangle$ (*bottom*) for particles with $|\eta| < 1$ in the "transverse" region for "back-to-back" events defined in Fig. 6-3 as a function of the leading jet P_T .

Figs. 4-4 thru 4-22 show the “response” factors (see Table 4-4) from PYTHIA Tune A and HERWIG for the observables in Table 4-3 for “leading jet” and “back-to-back” events as a function of the leading jet P_T . HERWIG and PYTHIA Tune A produce similar “response” factors for leading jet P_T greater than 50 GeV/c, but for lower leading jet P_T they are quite different. This will result in large systematic errors on the corrected observables in Table 4-3 at low leading jet P_T .

Fig. 4-23 shows the leading jet P_T correction used in method 2 for “leading jet” events. Figs. 4-24 shows the method 2 “response” factors from PYTHIA Tune A for some of the observables in Table 4-3 for “leading jet” events as a function of the leading jet P_T . The observable in Table 4-3 do not depend strongly on the leading jet P_T and hence the method 1 and method 2 correction factors are similar. This can be seen in Fig. 4-25 which compares the method 1 response factors versus the leading jet P_T (uncorrected) with the method 2 response factors versus the leading jet P_T (corrected) from PYTHIA Tune A. The method 2 correction factors ($1/\text{response factor}$) are applied data after correcting the leading jet P_T , while the method 1 correction factors are applied to the data without correcting the leading jet P_T .

Method 1 can be easily applied to both the “leading jet” and “back-to-back” events. In “back-to-back” events, method 1 corrects for calorimeter response for jet#1, jet#2, and jet#3 in one step. Figures 4-4 through 4-22 show that the response factors for “back-to-back” events are different from those of the “leading jet” events. The primary source of the difference is due to the requirement that $P_T(\text{jet\#3}) < 15 \text{ GeV/c}$ for “back-to-back” events and the “back-to-back” correction factors are correcting for the calorimeter response for jet#3. In order to apply method 2 to the “back-to-back” events we would

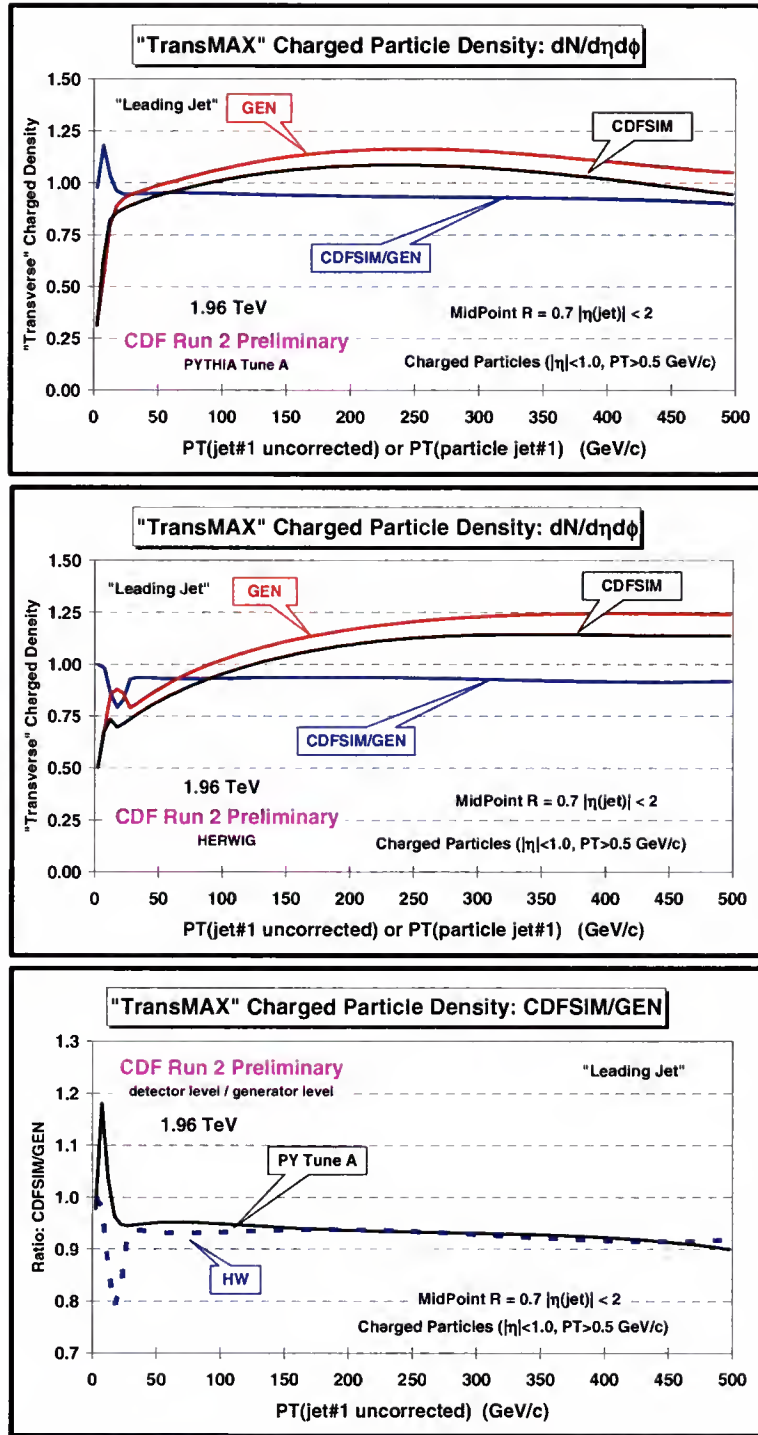


Figure 4-4: Method 1 response factors for the density of charged particles, $dN_{chg}/d\eta d\phi$, with $p_T > 0.5$ GeV/c and $|\eta| < 1$ in the "transMAX" region for "leading jet" events defined in Fig. 6-3 as a function of the leading jet P_T . Shows the particle level prediction (GEN) versus the leading particle jet P_T and the detector level result (CDFSIM) versus the leading calorimeter jet P_T (uncorrected) with $|\eta(jet\#1)| < 2$ for PYTHIA Tune A (*top*) and HERWIG (*middle*). Also shows the ratio of the detector level to the particle level, CDFSIM/GEN, versus the leading jet P_T (*i.e.* response factor).

have to first correct the P_T of jet#1, jet#2, and jet#3. Since the observables in Table 4-3 do not depend strongly on the P_T of jet#1, jet#2, and jet#3, it is much easier to use method 1 for both “leading jet” and “back-to-back” events. We will use the differences between method 1 and method 2 in “leading jet” events as a measure of the systematic uncertainty in correcting to the particle level.

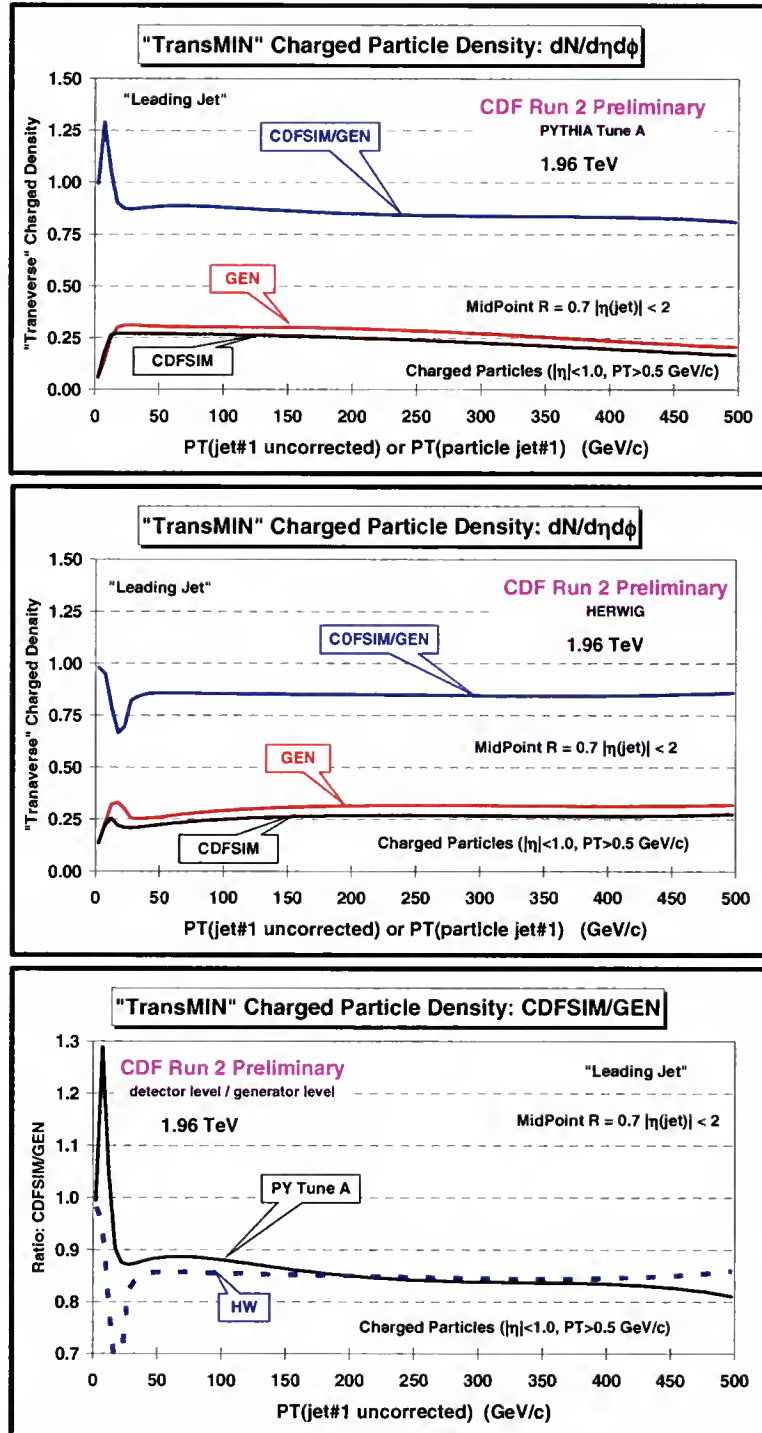


Figure 4-5: Method 1 response factors for the density of charged particles, $dN_{chg}/d\eta d\phi$, with $p_T > 0.5 \text{ GeV/c}$ and $|\eta| < 1$ in the “transMIN” region for “leading jet” events defined in Fig. 6-3 as a function of the leading jet P_T . Shows the particle level prediction (GEN) versus the leading particle jet P_T and the detector level result (CDFSIM) versus the leading calorimeter jet P_T (uncorrected) with $|\eta(jet\#1)| < 2$ for PYTHIA Tune A (*top*) and HERWIG (*middle*). Also shows the ratio of the detector level to the particle level, CDFSIM/GEN, versus the leading jet P_T (*i.e.* response factor).

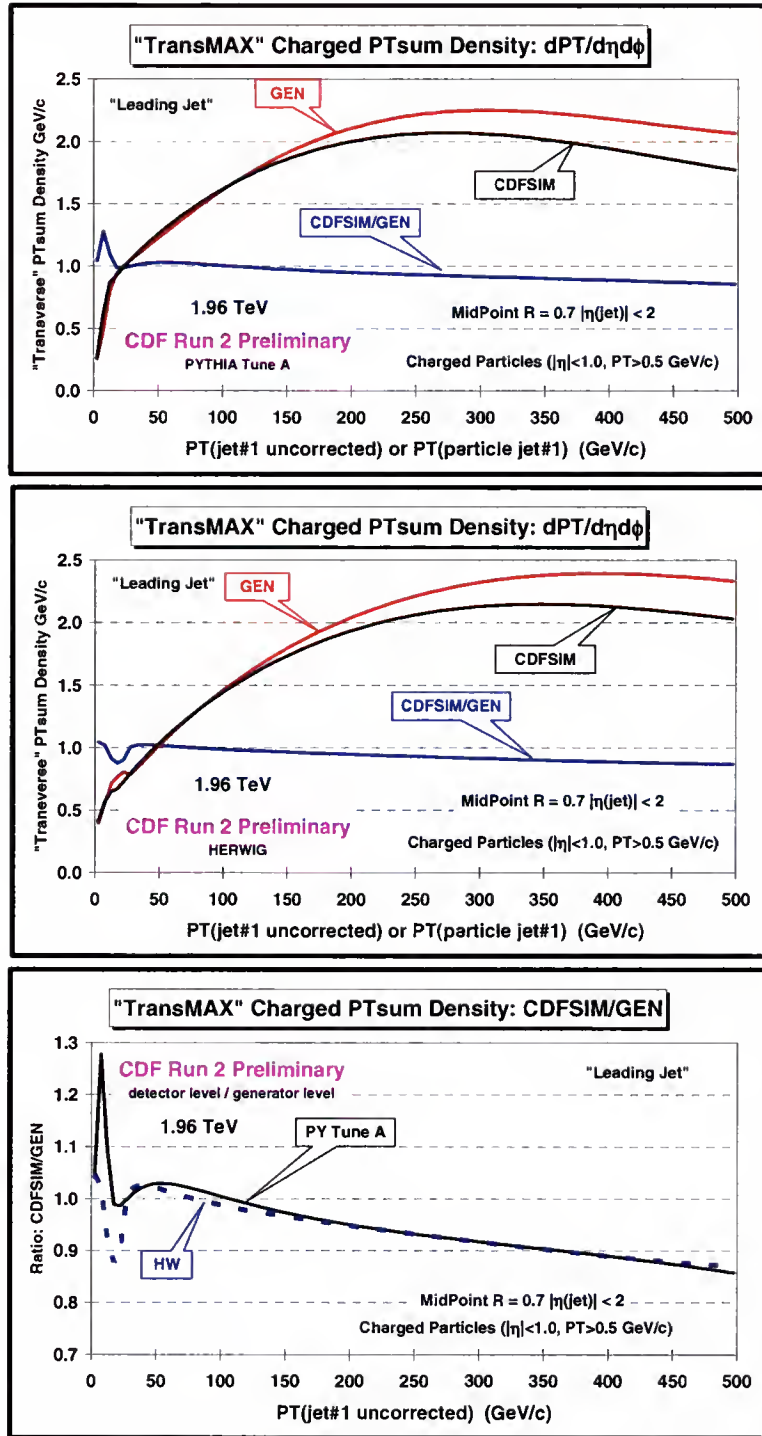


Figure 4-6: Method 1 response factors for the PTsum density of charged particles, $dPT_{sum}/d\eta d\phi$, with $p_T > 0.5$ GeV/c and $|\eta| < 1$ in the "transMAX" region for "leading jet" events defined in Fig. 6-3 as a function of the leading jet P_T . Shows the particle level prediction (GEN) versus the leading particle jet P_T and the detector level result (CDFSIM) versus the leading calorimeter jet P_T (uncorrected) with $|\eta(jet\#1)| < 2$ for PYTHIA Tune A (*top*) and HERWIG (*middle*). Also shows the ratio of the detector level to the particle level, CDFSIM/GEN, versus the leading jet P_T (*i.e.* response factor).

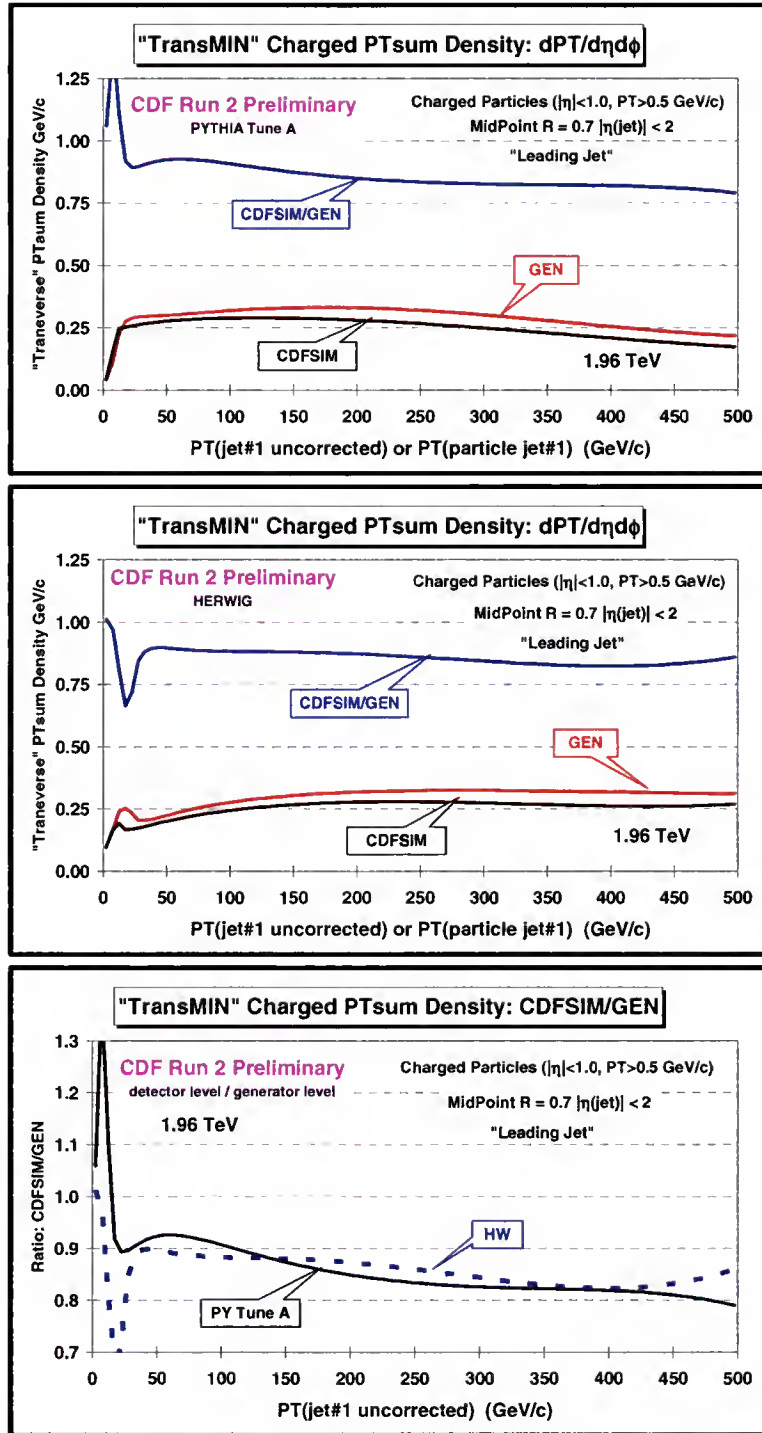


Figure 4-7: Method 1 response factors for the PTsum density of charged particles, $dPT_{sum}/d\eta d\phi$, with $p_T > 0.5 \text{ GeV/c}$ and $|\eta| < 1$ in the “transMIN” region for “leading jet” events defined in Fig. 6-3 as a function of the leading jet P_T . Shows the particle level prediction (GEN) versus the leading particle jet P_T and the detector level result (CDFSIM) versus the leading calorimeter jet P_T (uncorrected) with $|\eta(jet\#1)| < 2$ for PYTHIA Tune A (*top*) and HERWIG (*middle*). Also shows the ratio of the detector level to the particle level, CDFSIM/GEN, versus the leading jet P_T (*i.e.* response factor).

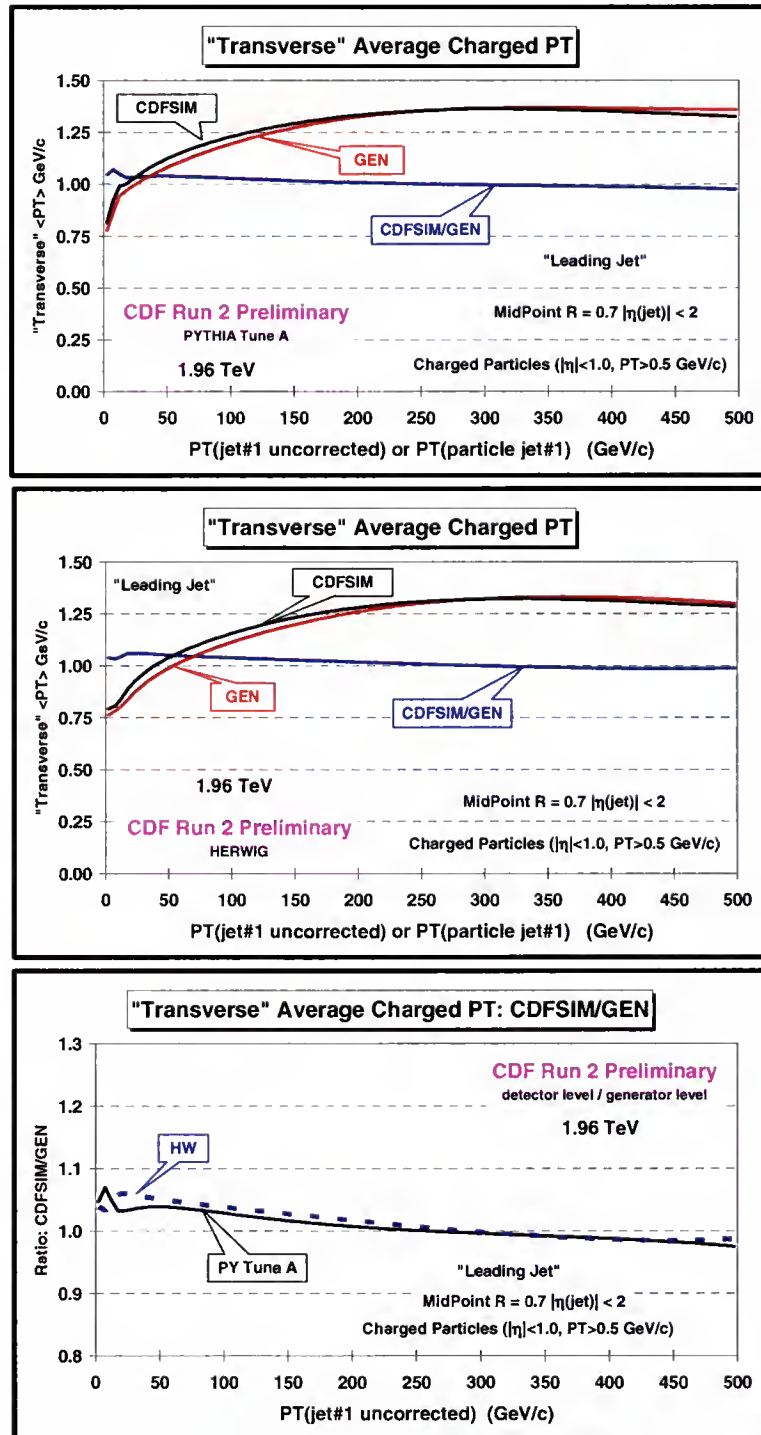


Figure 4-8: Method 1 response factors for the average $\langle p_T \rangle$ of charged particles with $p_T > 0.5$ GeV/c and $|\eta| < 1$ in the “transverse” region for “leading jet” events defined in Fig. 6-3 as a function of the leading jet P_T . Shows the particle level prediction (GEN) versus the leading particle jet P_T and the detector level result (CDFSIM) versus the leading calorimeter jet P_T (uncorrected) with $|\eta(jet\#1)| < 2$ for PYTHIA Tune A (*top*) and HERWIG (*middle*). Also shows the ratio of the detector level to the particle level, CDFSIM/GEN, versus the leading jet P_T (*i.e.* response factor).

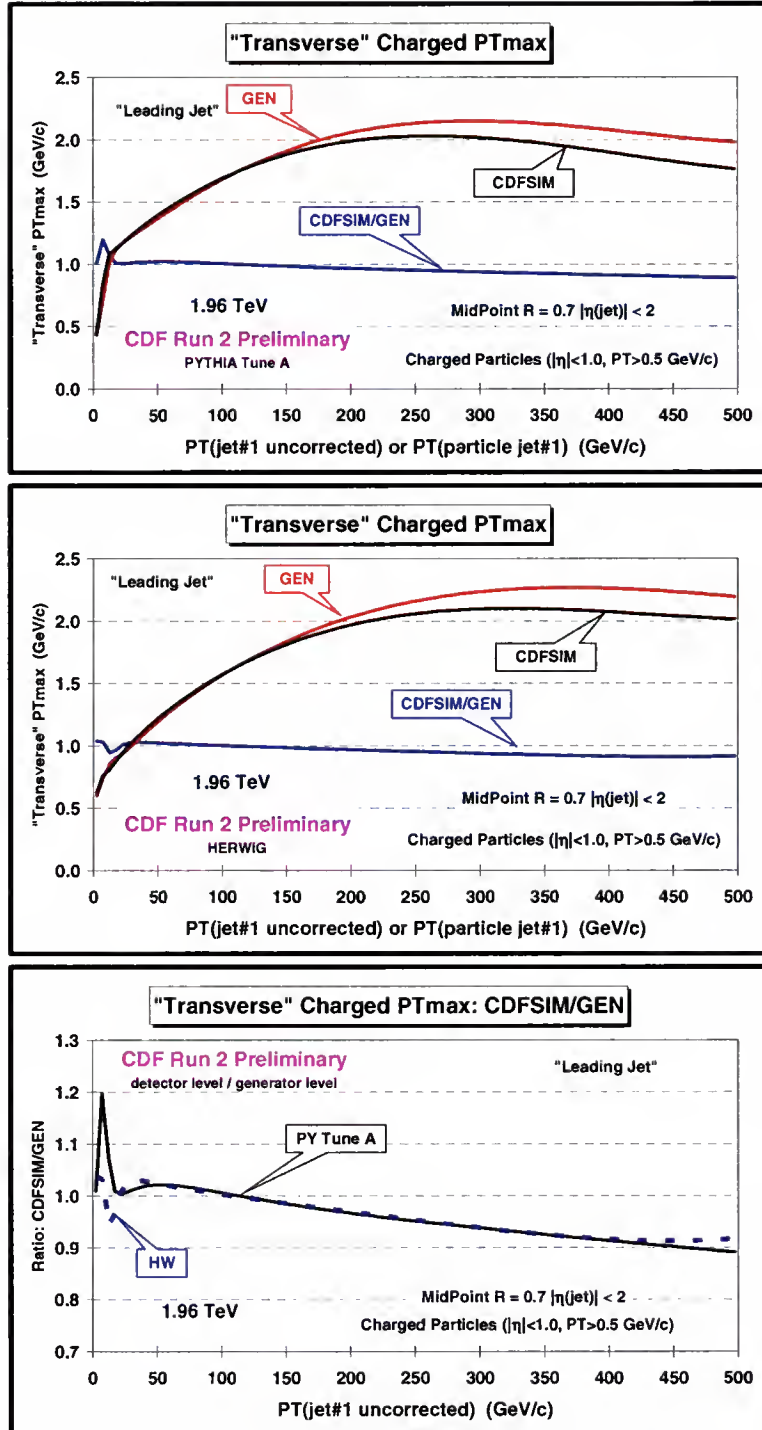


Figure 4-9: Method 1 response factors for the average maximum p_T , PT_{max} , for charged particles with $p_T > 0.5$ GeV/c and $|\eta| < 1$ in the “transverse” region for “leading jet” events defined in Fig. 6-3 as a function of the leading jet P_T . Shows the particle level prediction (GEN) versus the leading particle jet P_T and the detector level result (CDFSIM) versus the leading calorimeter jet P_T (uncorrected) with $|\eta(jet\#1)| < 2$ for PYTHIA Tune A (*top*) and HERWIG (*middle*). Also shows the ratio of the detector level to the particle level, CDFSIM/GEN, versus the leading jet P_T (*i.e.* response factor).

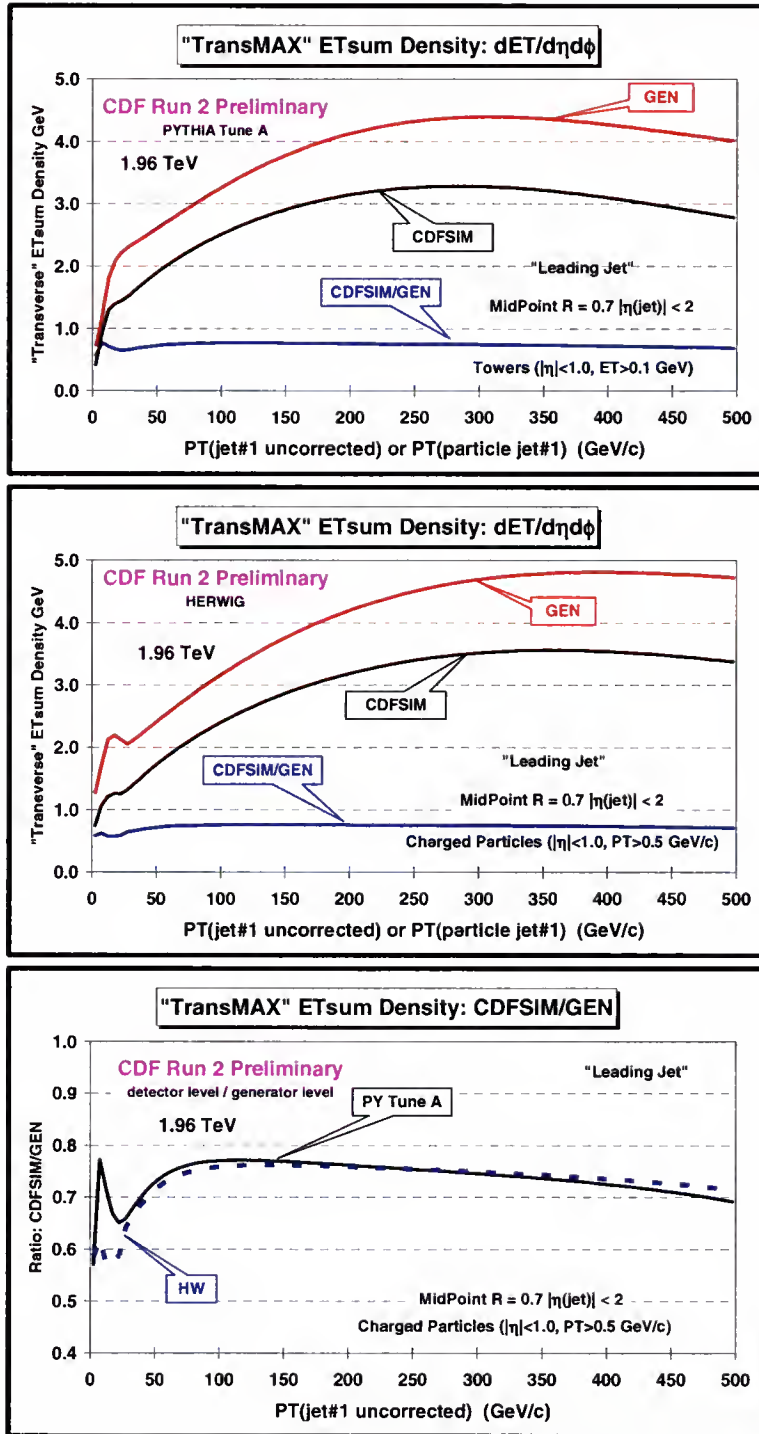


Figure 4-10: Method 1 response factors for the ETsum density of all particles, $dE_T/d\eta d\phi$, with $|\eta| < 1$ in the "transMAX" regions for "leading jet" events defined in Fig. 6-3 as a function of the leading jet P_T . Shows the particle level prediction (GEN) versus the leading particle jet P_T and the detector level result (CDFSIM) versus the leading calorimeter jet P_T (uncorrected) with $|\eta(jet\#1)| < 2$ for PYTHIA Tune A (*top*) and HERWIG (*middle*). Also shows the ratio of the detector level to the particle level, CDFSIM/GEN, versus the leading jet P_T (*i.e.* response factor).

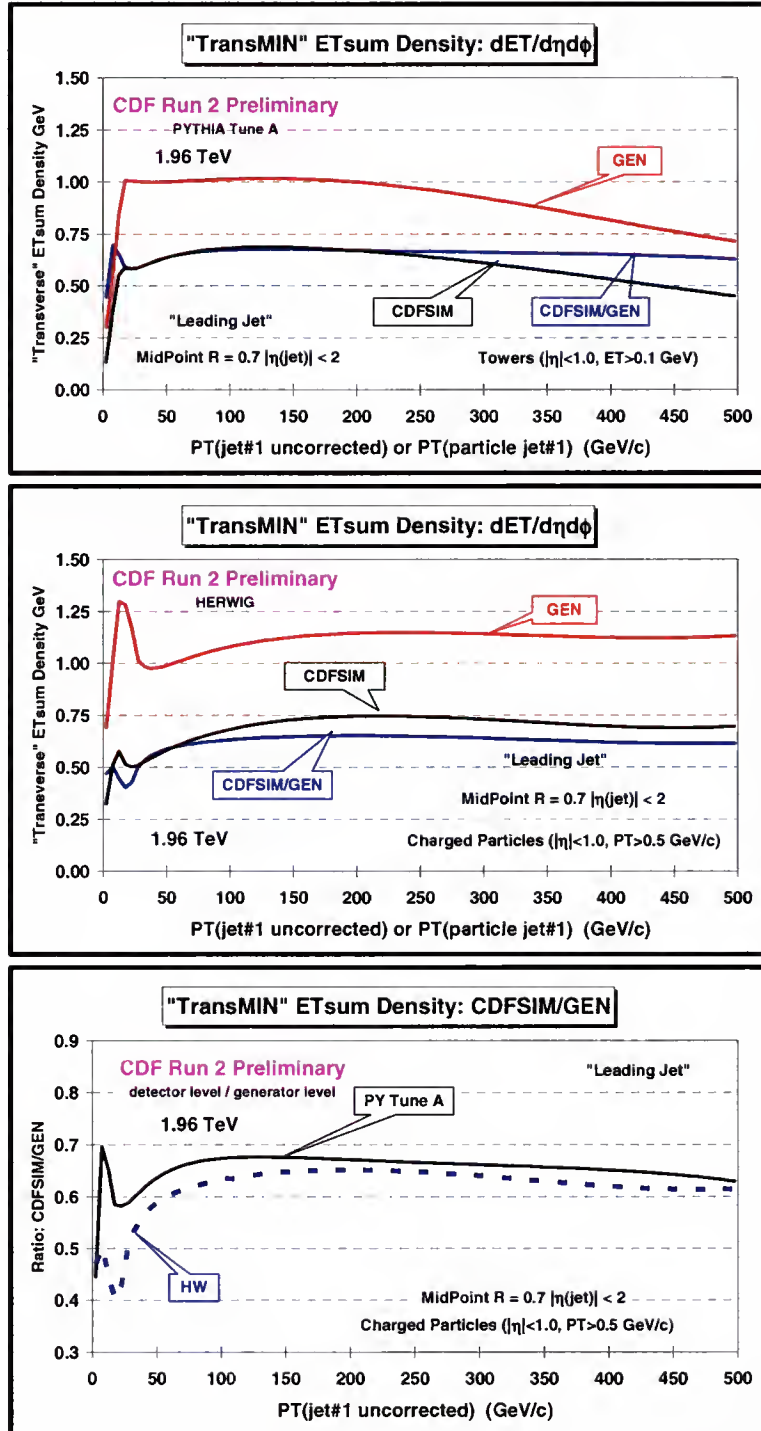


Figure 4-11: Method 1 response factors for the ETsum density of all particles, $dE_T/d\eta d\phi$, with $|\eta| < 1$ in the "transMIN" regions for "leading jet" events defined in Fig. 6-3 as a function of the leading jet P_T . Shows the particle level prediction (GEN) versus the leading particle jet P_T and the detector level result (CDFSIM) versus the leading calorimeter jet P_T (uncorrected) with $|\eta(jet\#1)| < 2$ for PYTHIA Tune A (*top*) and HERWIG (*middle*). Also shows the ratio of the detector level to the particle level, CDFSIM/GEN, versus the leading jet P_T (*i.e.* response factor).

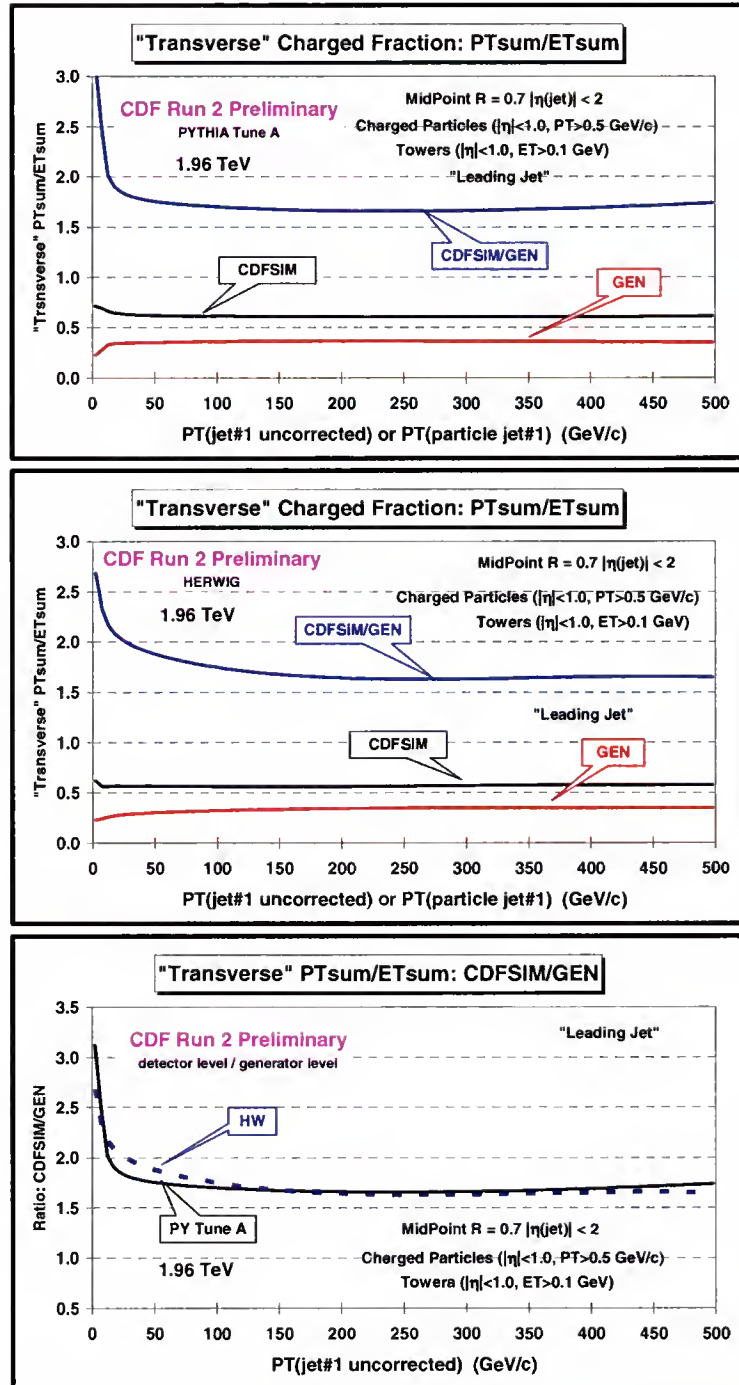


Figure 4-12: Method 1 response factors for the charged fraction, $PT_{\text{sum}}/ET_{\text{sum}}$, in the “transverse” region for “leading jet” events defined in Fig. 6-3 as a function of the leading jet P_T , where PT_{sum} includes charged particles with $p_T > 0.5 \text{ GeV/c}$ and $|\eta| < 1$ and the ET_{sum} includes all particles with $|\eta| < 1$. Shows the particle level prediction (GEN) versus the leading particle jet P_T and the detector level result (CDFSIM) versus the leading calorimeter jet P_T (uncorrected) with $|\eta(\text{jet\#1})| < 2$ for PYTHIA Tune A (*top*) and HERWIG (*middle*). Also shows the ratio of the detector level to the particle level, $CDFSIM/GEN$, versus the leading jet P_T (*i.e.* response factor).

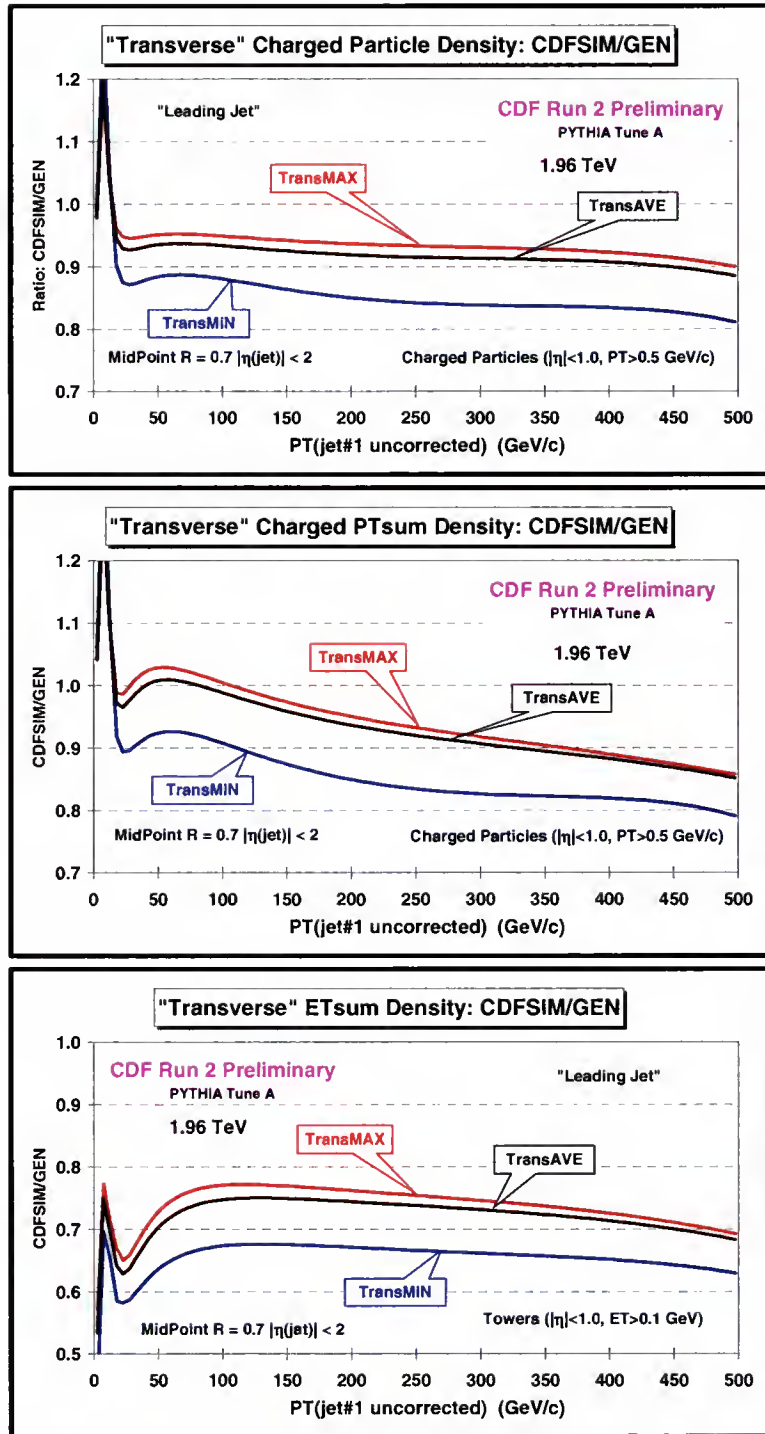


Figure 4-13: Shows the ratio of the detector level to the particle level, CDFSIM/GEN, versus the leading jet P_T (method 1 response factors) for PYTHIA Tune A for the "transMAX", "transMIN", and "transverse" regions for "leading jet" events defined in Fig. 6-3 as a function of the leading jet P_T . Shows the density of charged particles $dN_{\text{chg}}/d\eta d\phi$ with $p_T > 0.5$ GeV/c and $|\eta| < 1$ (top), the P_T sum density of charged particles $dP_T\text{sum}/d\eta d\phi$ with $p_T > 0.5$ GeV/c and $|\eta| < 1$ (middle), and E_T sum density of all particles $dE_T/d\eta d\phi$ with $|\eta| < 1$ (bottom).

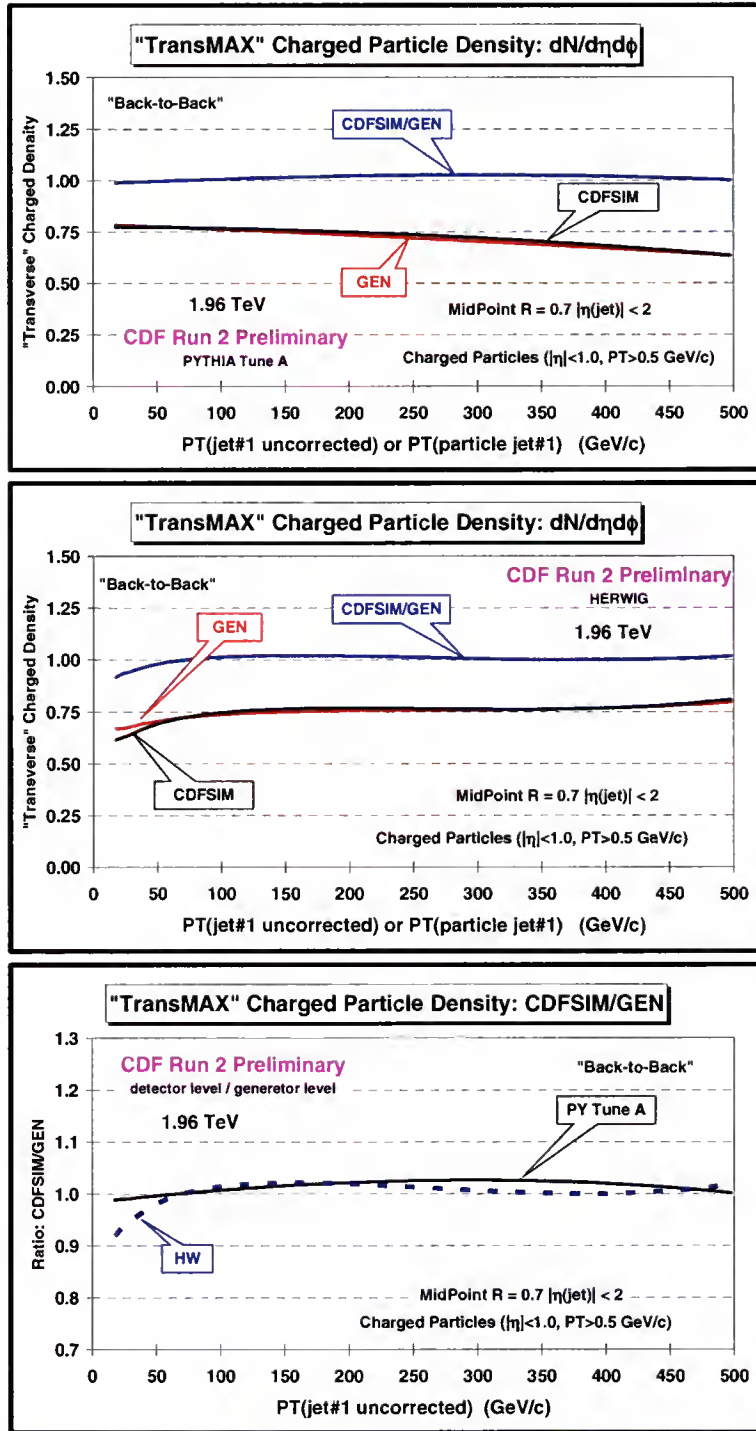


Figure 4-14: Method 1 response factors for the density of charged particles, $dN_{chg}/d\eta d\phi$, with $p_T > 0.5 \text{ GeV/c}$ and $|\eta| < 1$ in the "transMAX" region for "back-to-back" events defined in Fig. 6-3 as a function of the leading jet P_T . Shows the particle level prediction (GEN) versus the leading particle jet P_T and the detector level result (CDFSIM) versus the leading calorimeter jet P_T (uncorrected) with $|\eta(jet\#1)| < 2$ for PYTHIA Tune A (*top*) and HERWIG (*middle*). Also shows the ratio of the detector level to the particle level, CDFSIM/GEN, versus the leading jet P_T (*i.e.* response factor).

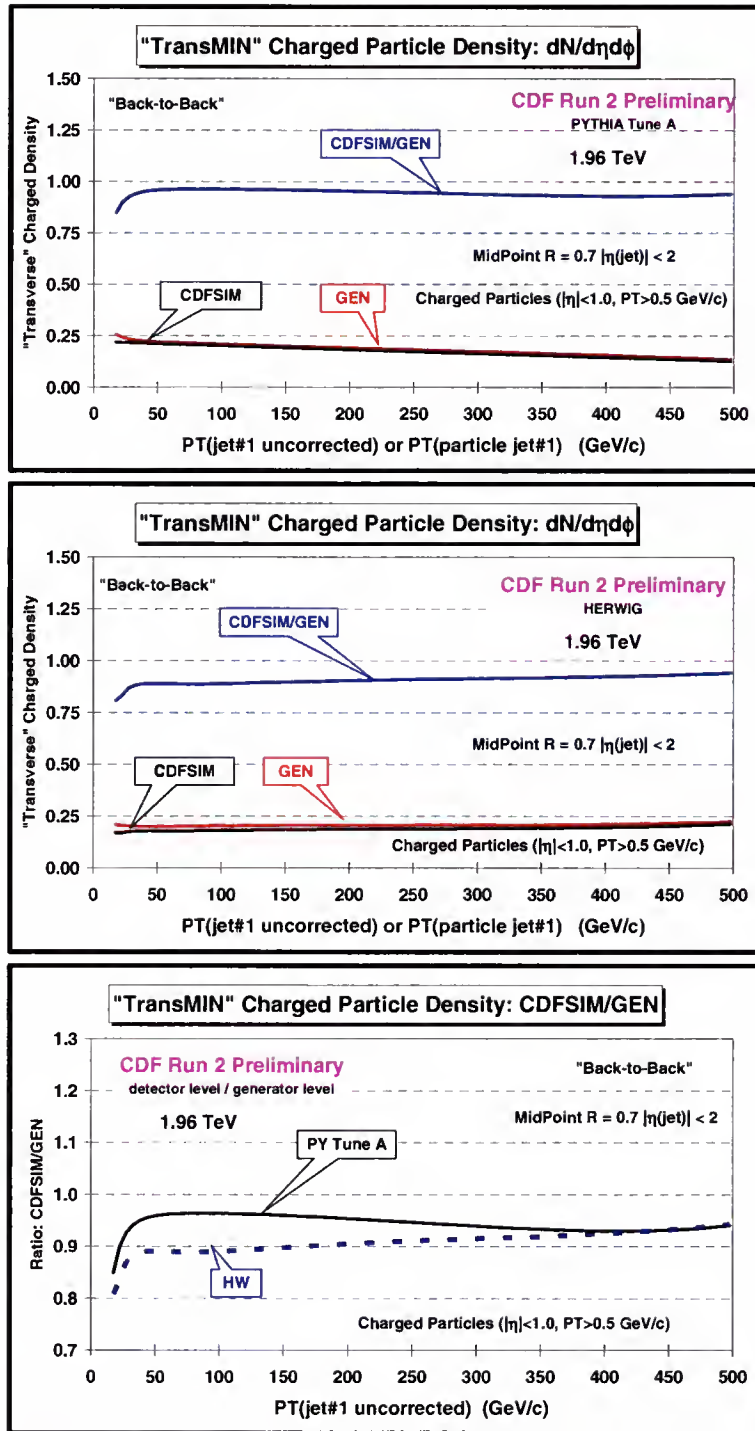


Figure 4-15: Method 1 response factors for the density of charged particles, $dN_{chg}/d\eta d\phi$, with $p_T > 0.5$ GeV/c and $|\eta| < 1$ in the "transMIN" region for "back-to-back" events defined in Fig. 6-3 as a function of the leading jet P_T . Shows the particle level prediction (GEN) versus the leading particle jet P_T and the detector level result (CDFSIM) versus the leading calorimeter jet P_T (uncorrected) with $|\eta(\text{jet\#1})| < 2$ for PYTHIA Tune A (*top*) and HERWIG (*middle*). Also shows the ratio of the detector level to the particle level, CDFSIM/GEN, versus the leading jet P_T (*i.e.* response factor).

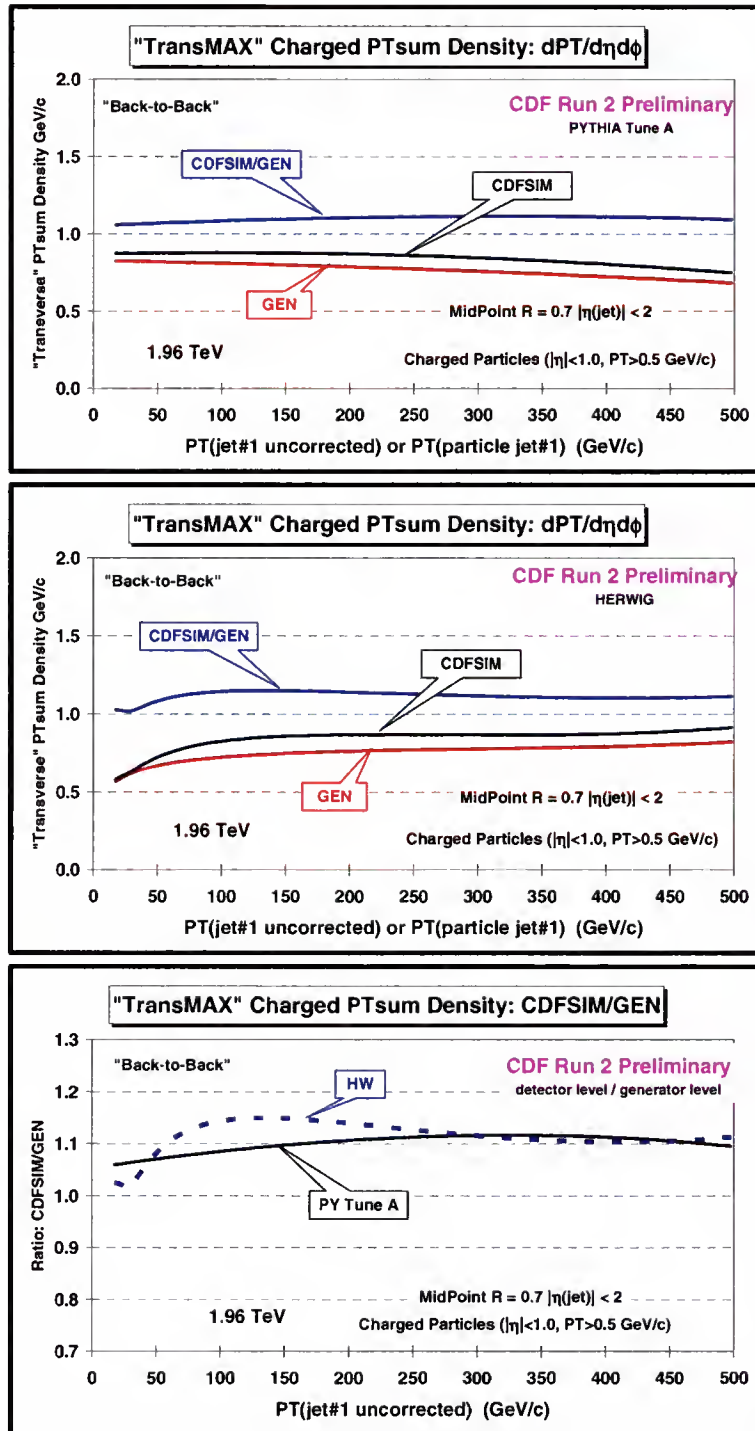


Figure 4-16: Method 1 response factors for the PTsum density of charged particles, $dPT_{sum}/d\eta d\phi$, with $p_T > 0.5$ GeV/c and $|\eta| < 1$ in the “transMAX” region for “back-to-back” events defined in Fig. 6-3 as a function of the leading jet P_T . Shows the particle level prediction (GEN) versus the leading particle jet P_T and the detector level result (CDFSIM) versus the leading calorimeter jet P_T (uncorrected) with $|\eta(jet\#1)| < 2$ for PYTHIA Tune A (*top*) and HERWIG (*middle*). Also shows the ratio of the detector level to the particle level, CDFSIM/GEN, versus the leading jet P_T (*i.e.* response factor).

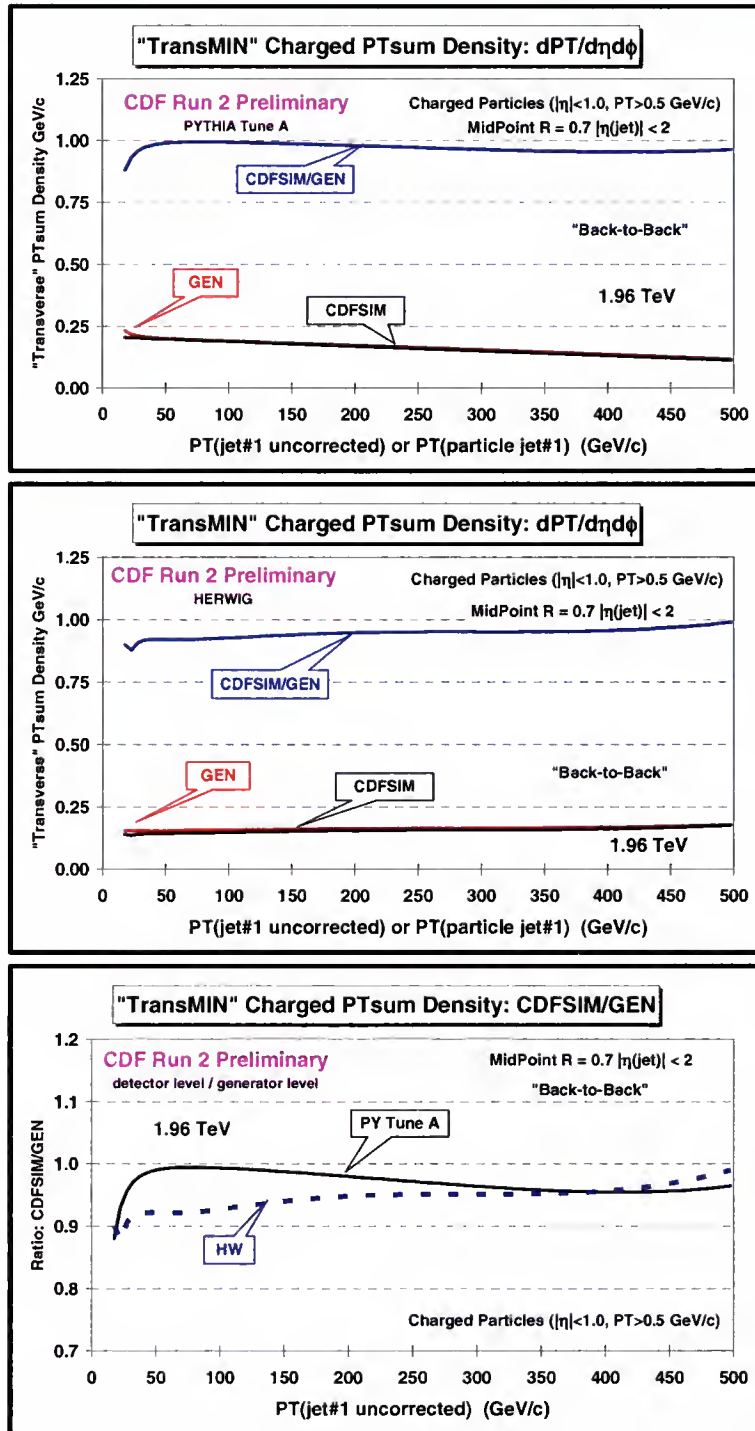


Figure 4-17: Method 1 response factors for the PTsum density of charged particles, $dPTsum/d\eta d\phi$, with $p_T > 0.5$ GeV/c and $|\eta| < 1$ in the “transMIN” region for “back-to-back” events defined in Fig. 6-3 as a function of the leading jet P_T . Shows the particle level prediction (GEN) versus the leading particle jet P_T and the detector level result (CDFSIM) versus the leading calorimeter jet P_T (uncorrected) with $|\eta(jet\#1)| < 2$ for PYTHIA Tune A (*top*) and HERWIG (*middle*). Also shows the ratio of the detector level to the particle level, CDFSIM/GEN, versus the leading jet P_T (*i.e.* response factor).

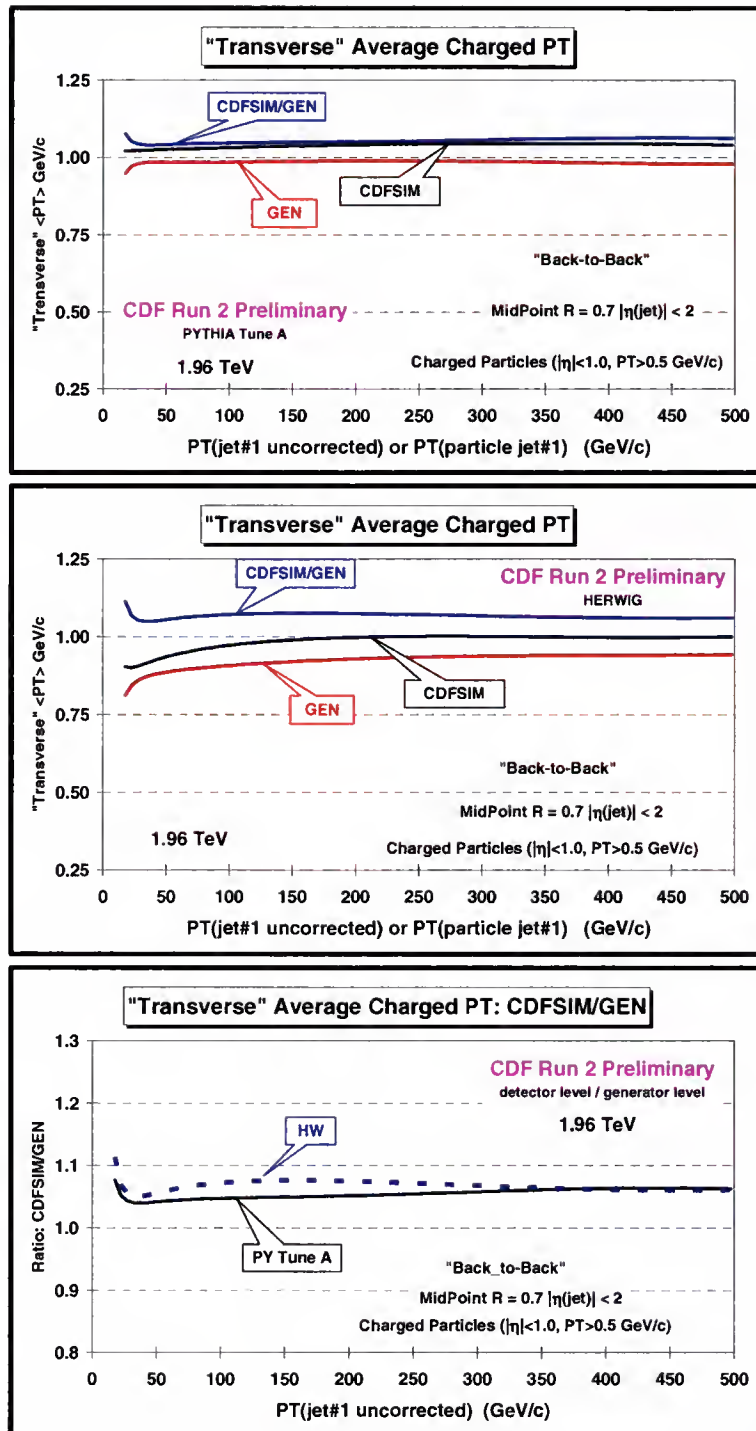


Figure 4-18: Method 1 response factors for the average $\langle p_T \rangle$ of charged particles with $p_T > 0.5$ GeV/c and $|\eta| < 1$ in the “transverse” region for “back-to-back” events defined in Fig. 6-3 as a function of the leading jet P_T . Shows the particle level prediction (GEN) versus the leading particle jet P_T and the detector level result (CDFSIM) versus the leading calorimeter jet P_T (uncorrected) with $|\eta(\text{jet\#1})| < 2$ for PYTHIA Tune A (*top*) and HERWIG (*middle*). Also shows the ratio of the detector level to the particle level, CDFSIM/GEN, versus the leading jet P_T (*i.e.* response factor).

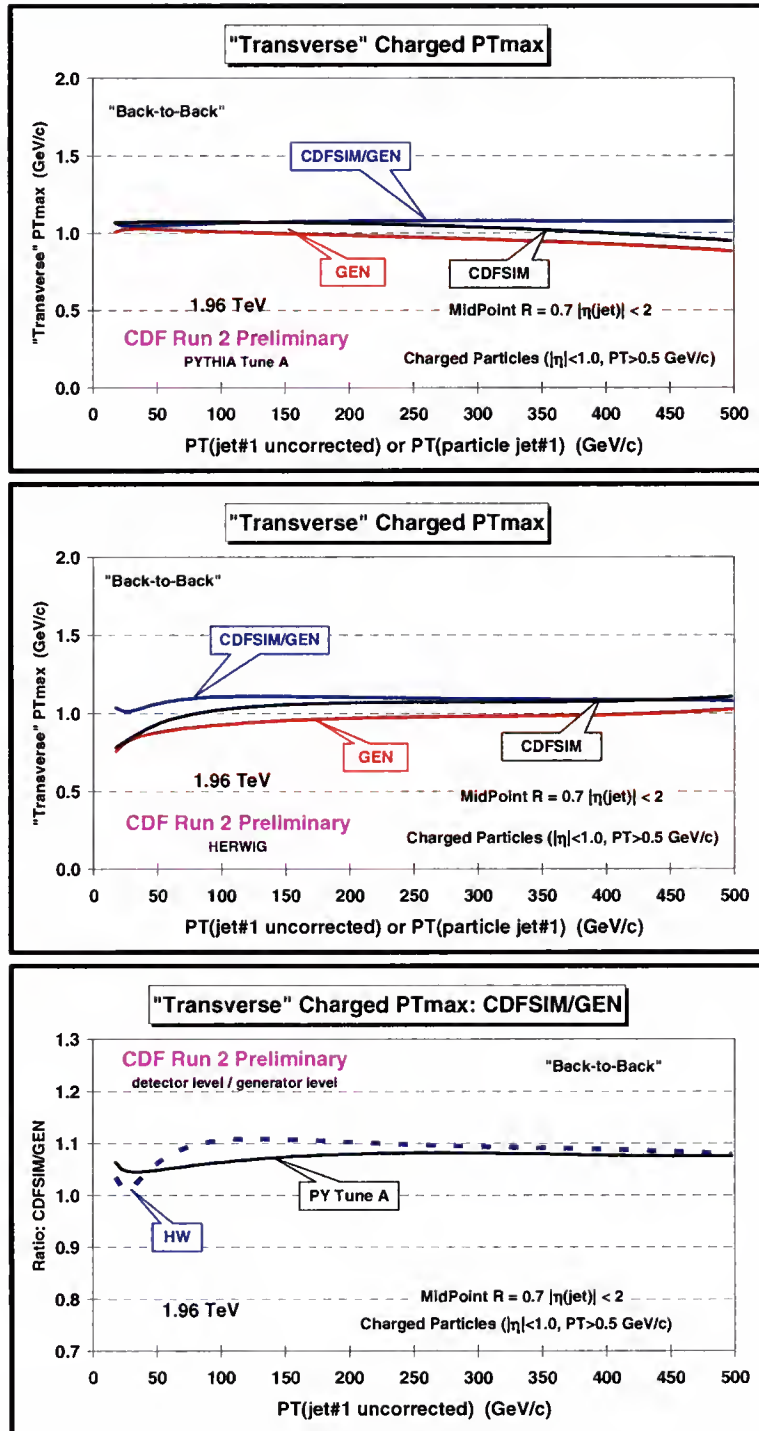


Figure 4-19: Method 1 response factors for the average maximum p_T , PT_{max} , for charged particles with $p_T > 0.5$ GeV/c and $|\eta| < 1$ in the "transverse" region for "back-to-back" events defined in Fig. 6-3 as a function of the leading jet P_T . Shows the particle level prediction (GEN) versus the leading particle jet P_T and the detector level result (CDFSIM) versus the leading calorimeter jet P_T (uncorrected) with $|\eta(jet\#1)| < 2$ for PYTHIA Tune A (*top*) and HERWIG (*middle*). Also shows the ratio of the detector level to the particle level, CDFSIM/GEN, versus the leading jet P_T (*i.e.* response factor).

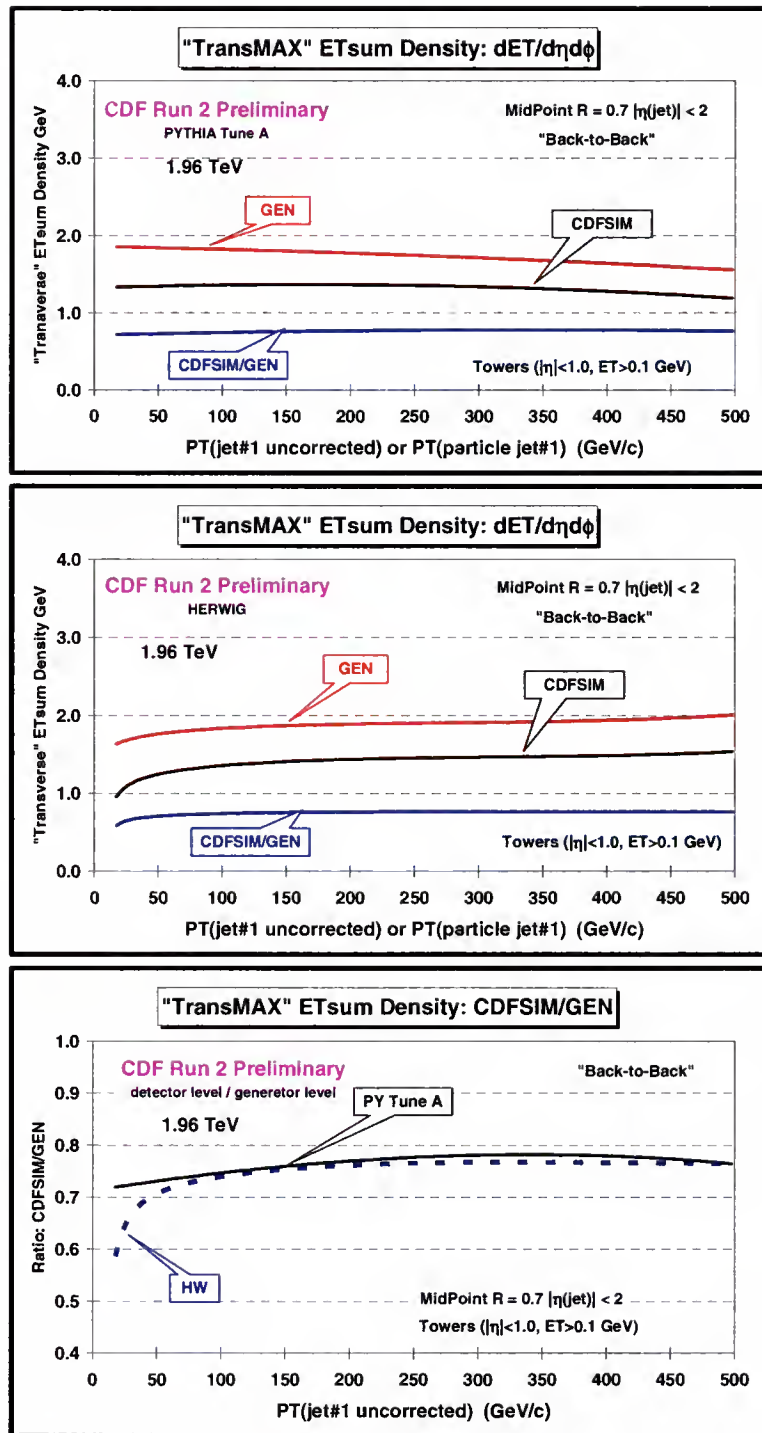


Figure 4-20: Method 1 response factors for the ETsum density of all particles, $dE_T/d\eta d\phi$, with $|\eta| < 1$ in the "transMAX" regions for "back-to-back" events defined in Fig. 6-3 as a function of the leading jet P_T . Shows the particle level prediction (GEN) versus the leading particle jet P_T and the detector level result (CDFSIM) versus the leading calorimeter jet P_T (uncorrected) with $|\eta(jet\#1)| < 2$ for PYTHIA Tune A (*top*) and HERWIG (*middle*). Also shows the ratio of the detector level to the particle level, CDFSIM/GEN, versus the leading jet P_T (*i.e.* response factor).

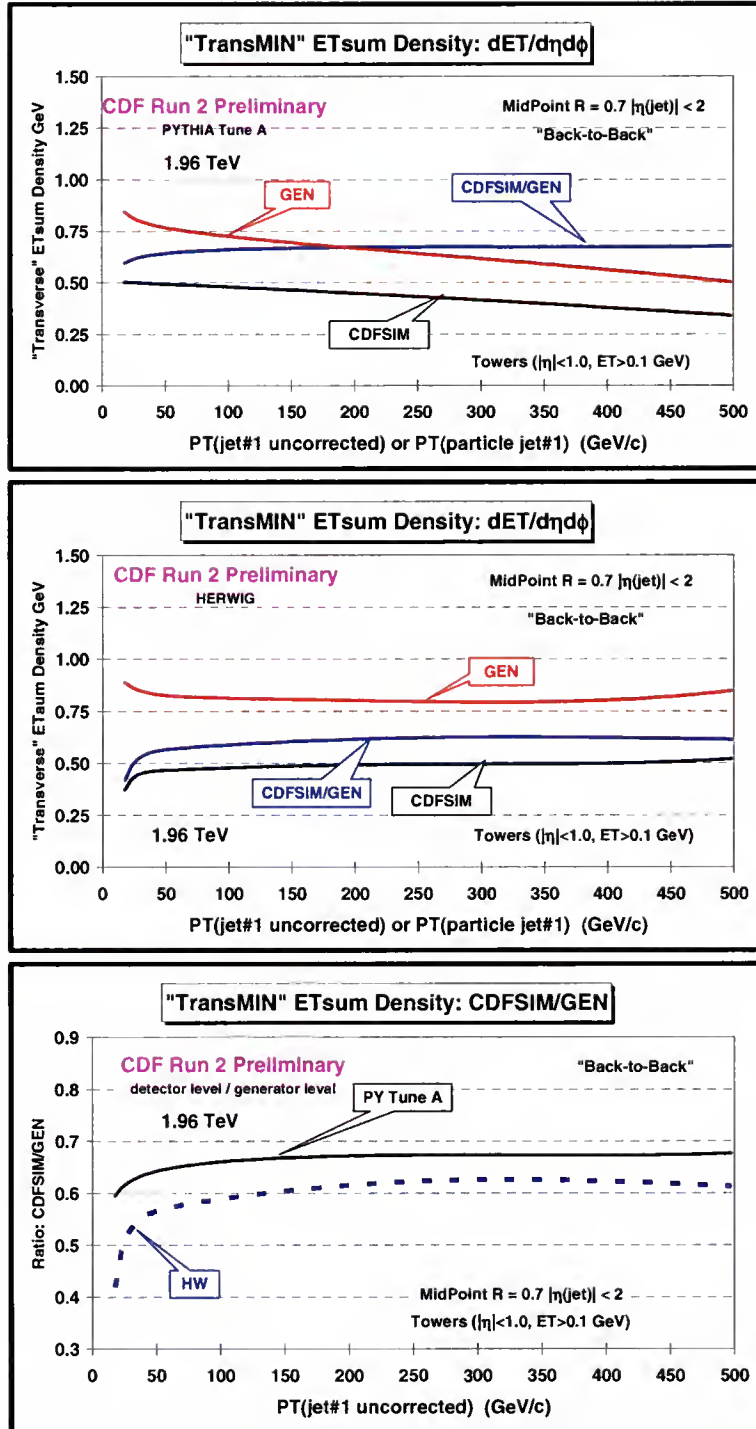


Figure 4-21: Method 1 response factors for the ETsum density of all particles, $dE_T/d\eta d\phi$, with $|\eta| < 1$ in the “transMIN” regions for “back-to-back” events defined in Fig. 6-3 as a function of the leading jet P_T . Shows the particle level prediction (GEN) versus the leading particle jet P_T and the detector level result (CDFSIM) versus the leading calorimeter jet P_T (uncorrected) with $|\eta(jet\#1)| < 2$ for PYTHIA Tune A (*top*) and HERWIG (*middle*). Also shows the ratio of the detector level to the particle level, CDFSIM/GEN, versus the leading jet P_T (*i.e.* response factor).

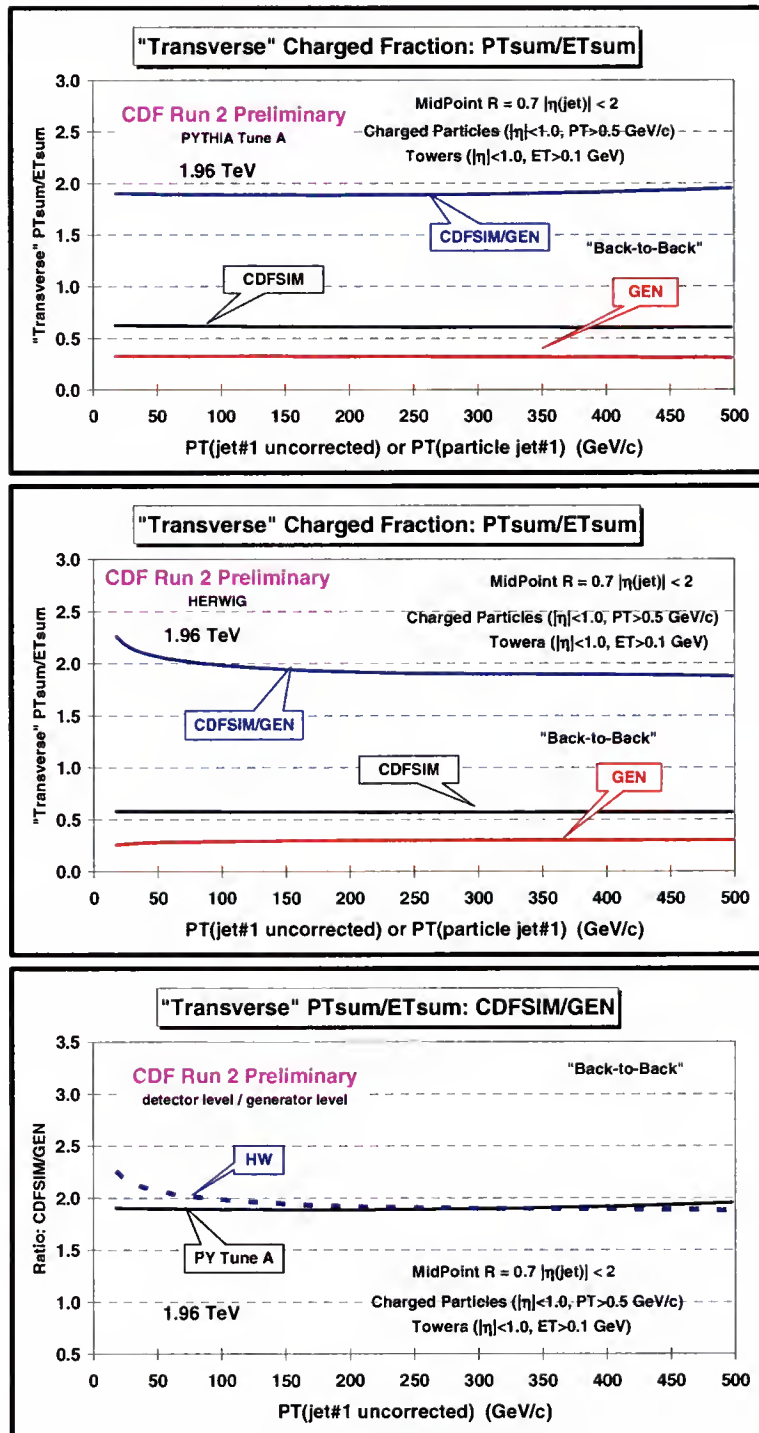


Figure 4-22: Method 1 response factors for the charged fraction, $PT_{\text{sum}}/ET_{\text{sum}}$, in the “transverse” region for “back-to-back” events defined in Fig. 6-3 as a function of the leading jet P_T , where PT_{sum} includes charged particles with $p_T > 0.5$ GeV/c and $|\eta| < 1$ and the ET_{sum} includes all particles with $|\eta| < 1$. Shows the particle level prediction (GEN) versus the leading particle jet P_T and the detector level result (CDFSIM) versus the leading calorimeter jet P_T (uncorrected) with $|\eta(\text{jet}\#1)| < 2$ for PYTHIA Tune A (*top*) and HERWIG (*middle*). Also shows the ratio of the detector level to the particle level, CDFSIM/GEN, versus the leading jet P_T (*i.e.* response factor).

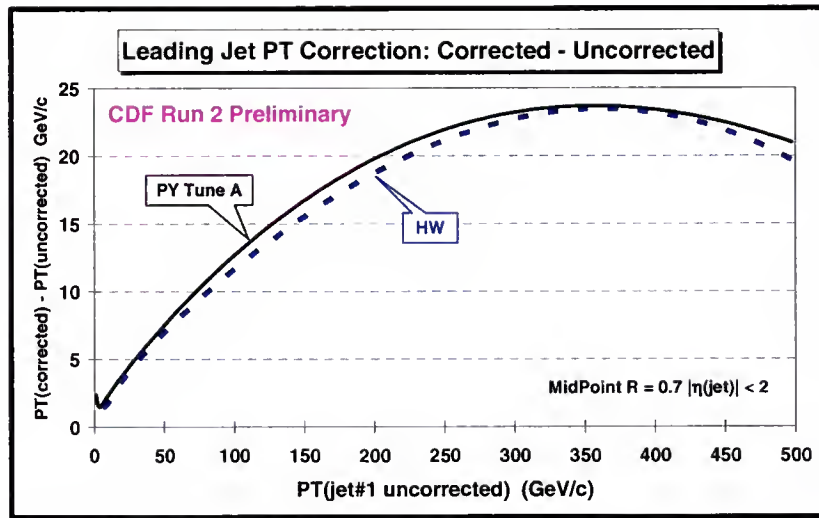


Figure 4-23: Leading jet P_T correction used in method 2 for “leading jet” events. Shows the difference in the observed leading jet P_T at the detector level (*i.e.* in the calorimeter) compared with the true P_T (*i.e.* corrected) of matched leading particle jets using PYTHIA Tune A and HERWIG.

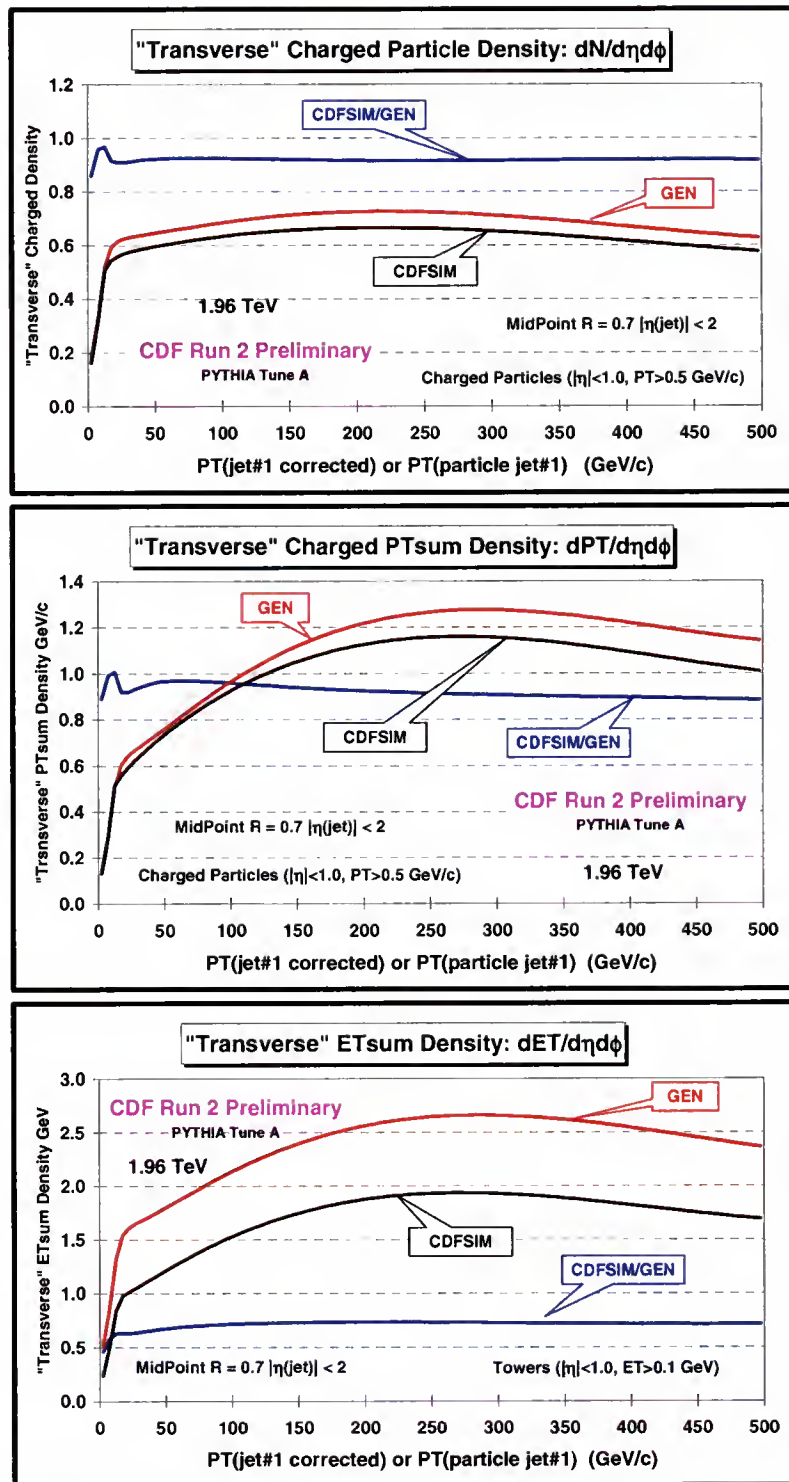


Figure 4-24: Method 2 response factors from PYTHIA Tune A for “leading jet” events defined in Fig. 6-3 as a function of the leading jet P_T . Shows the particle level prediction (GEN) versus the leading particle jet P_T and the detector level result (CDFSIMcor) versus the leading calorimeter jet P_T (corrected) with $|\eta(jet\#1)| < 2$. Also shows the ratio of the detector level to the particle level, CDFSIMcor/GEN, versus the leading jet P_T (*i.e.* response factor).

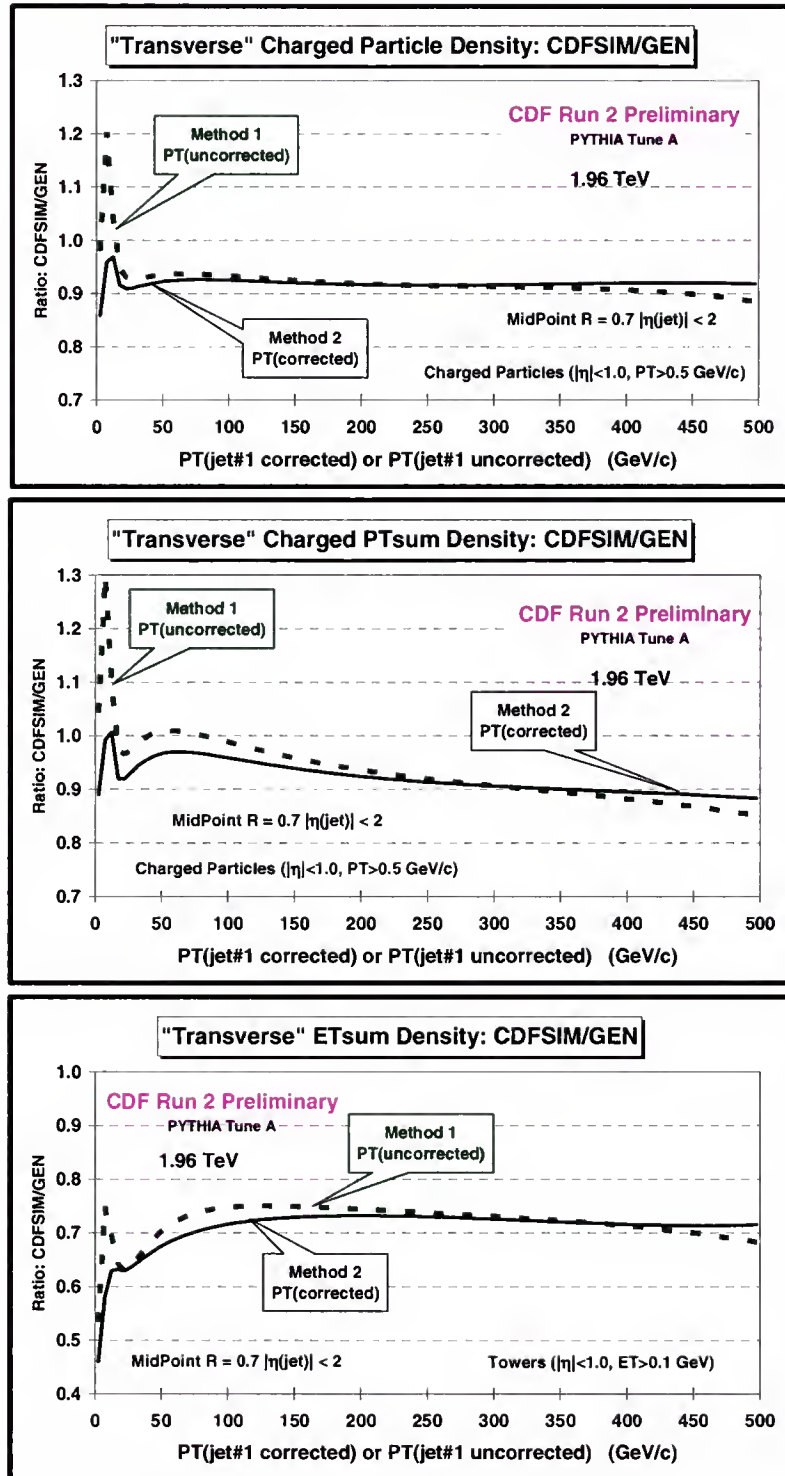


Figure 4-25: Compares the method 1 response factors versus the leading jet P_T (uncorrected) with the method 2 response factors versus the leading jet P_T (corrected) from PYTHIA Tune A.

CHAPTER 5 DATA SELECTION AND SYSTEMATIC ERRORS

5.1 Data Selection

The data used in this analysis arise from the set of Stntuples created for the QCD group by Anwar Bhatti, Ken Hatakeyama, and Craig Group (see Table 5-1). Events are required to be on the “goodrun” list (version 7). They are also required to have a missing E_T significance less than $5 \text{ GeV}^{1/2}$ and to have a $\text{sumET} < 1.5 \text{ TeV}$. Except for the Min-Bias data we require events to have one and only one quality 12 vertex with $|z| < 60 \text{ cm}$. For the Min-Bias data we allow zero or one quality 12 vertices. This only affects the observables in Table 4-3 for leading jet P_T below $10 \text{ GeV}/c$. Above $P_T(\text{jet}\#1) = 10 \text{ GeV}/c$ the fraction of events with no quality 12 vertex is negligible.

Table 5-1: Data sets (5.3.3nt) and event selection criterion used in this analysis ($L \sim 380 \text{ pb}^{-1}$).

Event Selection	Min-Bias	JET20	JET50	JET70	JET100
Total Events	20,586,733	30,470,383	9,908,366	4,641,247	5,366,515
“Good” Events (version 7)	18,180,015	19,835,681	6,868,114	3,432,992	4,031,324
MetSig $< 5 \text{ GeV}^{1/2}$, sumET $< 1.5 \text{ TeV}$	18,179,280	19,818,879	6,785,357	3,316,514	3,602,989
1 Q12 ZVtx, $ z < 60 \text{ cm}$	15,416,180	10,851,963	3,745,616	1,794,739	1,939,382
“Leading Jet” $ \eta(\text{jet}\#1) < 2$	3,712,407	7,679,594	3,200,065	1,648,764	1,884,353
“Back-to-Back” $P_T(\text{jet}\#3) < 15 \text{ GeV}/c$	2,474	1,462,547	878,014	491,930	602,256
“Back-to-Back”/“Leading Jet”	0.07%	19.04%	27.44%	29.84%	31.96%

As in a Run 1 analysis [13] only charged particles in the region $p_T > 0.5 \text{ GeV}/c$ and $|\eta| < 1$ where the COT efficiency is high are considered. Our track selection criterion shown in Table 5-2 is the same as the Run 1 analysis.

Table 5-2: Track Selection criterion.

Track Selection
COT measured tracks
$ z-z_0 < 2 \text{ cm}$
$ d_0 < 1 \text{ cm}$
$p_T > 0.5 \text{ GeV}/c, \eta < 1$

In forming the observables in Table 4-3 the five trigger sets shown in Table 5-1 are pieced together as shown in Table 5-3. The “looser” trigger set is used until it overlaps the next trigger set and then that trigger set is used until it overlaps the next trigger set etc.

Table 5-3: Range of $P_T(\text{jet\#1})$ used for each data set.

Trigger Set	Calorimeter Jets
Min-Bias	$P_T(\text{jet\#1}) < 30 \text{ GeV}$
JET20	$30 < P_T(\text{jet\#1}) < 70 \text{ GeV}$
JET50	$70 < P_T(\text{jet\#1}) < 95 \text{ GeV}$
JET70	$95 < P_T(\text{jet\#1}) < 130 \text{ GeV}$
JET100	$P_T(\text{jet\#1}) > 130 \text{ GeV}$

5.2 Systematic Uncertainty

The systematic uncertainty in correcting to the particle level is estimated by combining the two factors shown in Table 5-4. The first factor, σ_1 , comes from correcting the observables in Table 4-3 to the particle level using method 1 and examining the bin-by-bin difference between PYTHIA Tune A and HERWIG for each observable. The second factor, σ_2 , is set large enough to include the differences between method 1 and method 2 and pile-up (only affects the transverse energy).

Figure 5-1 shows the data at 1.96 TeV corrected to the particle level using method 1 and method 2. The open red squares are the data corrected to the particle level using method 1 with errors that include both the statistical error and the systematic uncertainty

(see Table 5-4). The black dots are the data corrected to the particle level using method 2 (with no errors). The method 2 points lie within the errors of the method 1 data points.

Table 5-4: The errors on the corrected observables in Table 4-3 include both the statistical error and the systematic uncertainty (added in quadrature). The systematic uncertainty consists of σ_1 and σ_2 (added in quadrature).

Uncertainty	Origin
σ_1	Bin by bin difference between the data corrected by PYTHIA Tune A and HERWIG using method 1.
σ_2	Difference between method 1 and method 2 and pile-up and miscellaneous (3% for charged particle, 5% for energy)

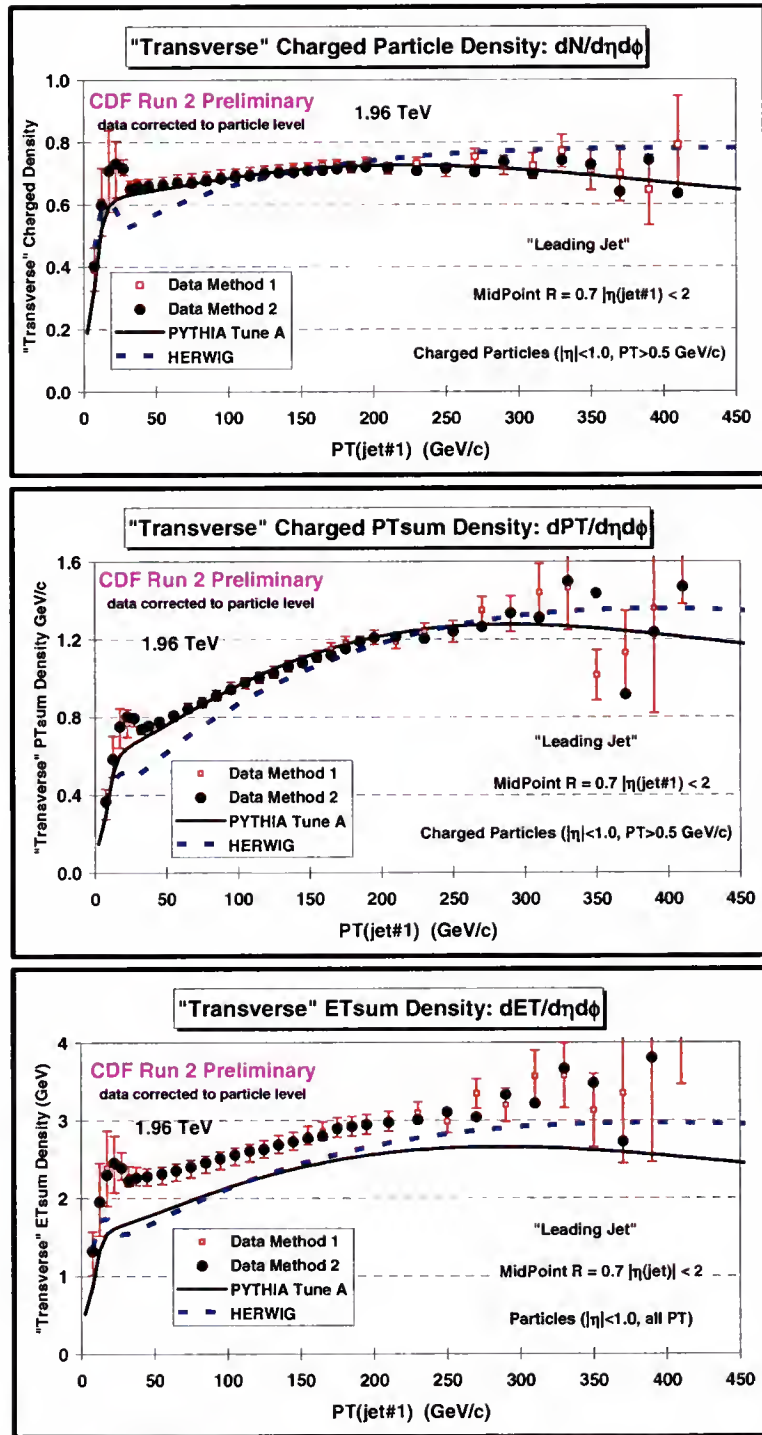


Figure 5-1: Data at 1.96 TeV corrected to the particle level using method 1 and method 2 compared with PYTHIA Tune A and HERWIG at the particle level. Shows the density of charged particles, $dN_{\text{chg}}/d\eta d\phi$ (*top*), the PTsum density of charged particles, $dP_{T\text{sum}}/d\eta d\phi$ (*middle*), ($p_T > 0.5$ GeV/c and $|\eta| < 1$), and the ETsum density, $dE_T/d\eta d\phi$ (*bottom*), for particles with $|\eta| < 1$ in the “transverse” region (average of “transMAX” and “transMIN”) for “leading jet” events defined in Fig. 6-3 as a function of the leading jet P_T .

CHAPTER 6

DISCUSSION OF RESULTS

We study the behavior of the charged particles ($P_T > 0.5$ GeV/c, $|\eta| < 1$) in the “underlying event” for hard scattering $p\bar{p}$ collisions at the Tevatron ($\sqrt{s} = 1.96$ TeV). These results are compared to QCD Monte-Carlo models (PYTHIA Tune A and HERWIG) that simulate $p\bar{p}$ collisions. The topology of a hard scattering jet event serves to define a frame of reference. The direction of the leading calorimeter jet, jet#1, is used to define correlations in the azimuthal angle, $\Delta\phi$. The angle $\Delta\phi = \phi - \phi_{\text{jet}\#1}$ is the relative angle between a charged particle and the leading jet direction. Figure 6-1 shows how we partition η - ϕ space on an event-by-event basis.

In figure 6-2 we define “transverse 1” and “transverse 2” so that we may compare these regions on an event-by-event basis. This allows us the flexibility to redefine how the regions are characterized for different analyses. Here we will refer to events in which there are no restrictions placed on the second highest E_T jet, jet#2, as “leading jet” events. Additionally, we define a subset of these as “back-to-back” events in which the leading two jets are nearly “back-to-back” ($\Delta\phi_{12} > 150^\circ$) and with $E_T(\text{jet}\#2)/E_T(\text{jet}\#1) > 0.8$. Within this subset, the hard component of the “underlying event” should be suppressed, thus increasing the sensitivity of the “transverse” region to the “beam-beam remnant” and multiple parton scattering components.

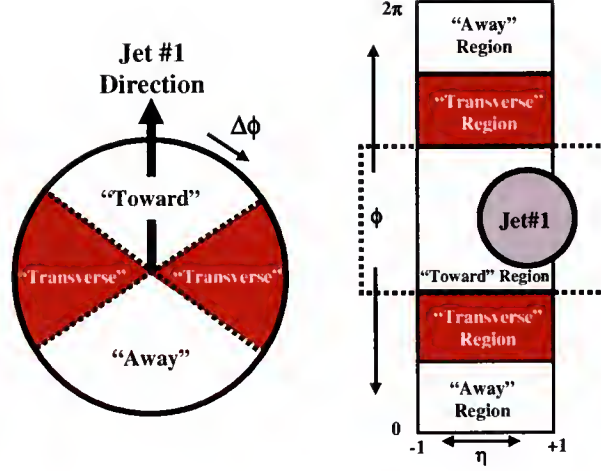


Figure 6-1: Illustration of correlations in azimuthal angle $\Delta\phi$ relative to the direction of the leading jet (MidPoint, $R = 0.7$, $f_{\text{merge}} = 0.75$) in the event, jet#1. The angle $\Delta\phi = \phi - \phi_{\text{jet}\#1}$ is the relative azimuthal angle between charged particles (or calorimeter towers) and the direction of jet#1. The “toward” region is defined by $|\Delta\phi| < 60^\circ$ and $|\eta| < 1$, while the “away” region is $|\Delta\phi| > 120^\circ$ and $|\eta| < 1$. The “transverse” region is defined by $60^\circ < |\Delta\phi| < 120^\circ$ and $|\eta| < 1$. Each of the three regions “toward”, “transverse”, and “away” and has an overall area in η - ϕ space of $\Delta\eta\Delta\phi = 4\pi/3$. We examine charged particles in the range $p_T > 0.5$ GeV/c and $|\eta| < 1$ and calorimeter towers with $E_T > 0.1$ GeV and $|\eta| < 1$, but allow the leading jet to be in the region $|\eta(\text{jet}\#1)| < 2$.

As in figure 6-3, we use the direction of jet#1 to define the two “transverse” regions, $60^\circ \leq |\Delta\phi| \leq 120^\circ$. On an event-by-event basis, we define the “transMAX” (“transMIN”) to be the maximum (minimum) of these two regions. When looking at multiplicities MAX and MIN refer to the number of charged particles, but when considering $P_{T\text{sum}}$ then MAX and MIN refer to the scalar $P_{T\text{sum}}$ of the charged particles.

Figure 6-4 illustrates the topology of a $p\bar{p}$ collision in which a “hard” parton-parton scattering has occurred. The contribution from the hardest initial or final-state radiation should be found in the “transMAX” region. Since both regions should receive “beam-beam remnant” contributions, the difference between “transMAX” and “transMIN” should be very sensitive to the “hard scattering” component of the “underlying event”.

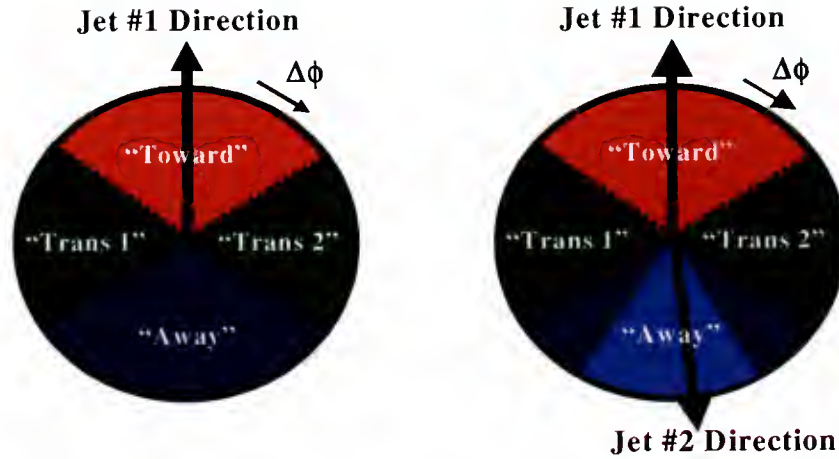


Figure 6-2: Illustration of correlations in azimuthal angle $\Delta\phi$ relative to the direction of the leading jet (highest P_T jet) in the event, jet#1. The angle $\Delta\phi = \phi - \phi_{\text{jet}\#1}$ is the relative azimuthal angle between charged particles and the direction of jet#1. The “toward” region is defined by $|\Delta\phi| < 60^\circ$ and $|\eta| < 1$, while the “away” region is $|\Delta\phi| > 120^\circ$ and $|\eta| < 1$. The two “transverse” regions $60^\circ < \Delta\phi < 120^\circ$ and $60^\circ < -\Delta\phi < 120^\circ$ are referred to as “transverse 1” and “transverse 2”. Each of the two “transverse” regions have an area in η - ϕ space of $\Delta\eta\Delta\phi = 4\pi/6$. The overall “transverse” region defined in Fig. 3 corresponds to combining the “transverse 1” and “transverse 2” regions. Events in which there are no restrictions placed on the second highest P_T jet, jet#2, are referred to as “leading jet” events (*left*). Events with at least two jets where the leading two jets are nearly “back-to-back” ($\Delta\phi_{12} > 150^\circ$) with $P_T(\text{jet}\#2)/P_T(\text{jet}\#1) > 0.8$ and $P_T(\text{jet}\#3) < 15 \text{ GeV}/c$ are referred to as “back-to-back” events (*right*).

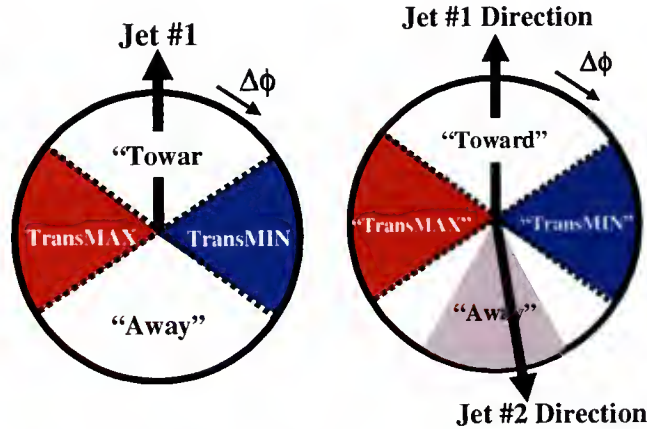


Fig. 6-3: Illustration of correlations in azimuthal angle $\Delta\phi$ relative to the direction of the leading jet (highest P_T jet) in the event, jet#1 for “leading jet” events (*left*) and “back-to-back” events (*right*) as defined in Fig. 6-2. The angle $\Delta\phi = \phi - \phi_{\text{jet}\#1}$ is the relative azimuthal angle between charged particles (or calorimeter towers) and the direction of jet#1. On an event by event basis, we define “transMAX” (“transMIN”) to be the maximum (minimum) of the two “transverse” regions, $60^\circ < \Delta\phi < 120^\circ$ and $60^\circ < -\Delta\phi < 120^\circ$. “TransMAX” and “transMIN” each have an area in η - ϕ space of $\Delta\eta\Delta\phi = 4\pi/6$. The overall “transverse” region defined in Fig. 3 includes both the “transMAX” and the “transMIN” region.

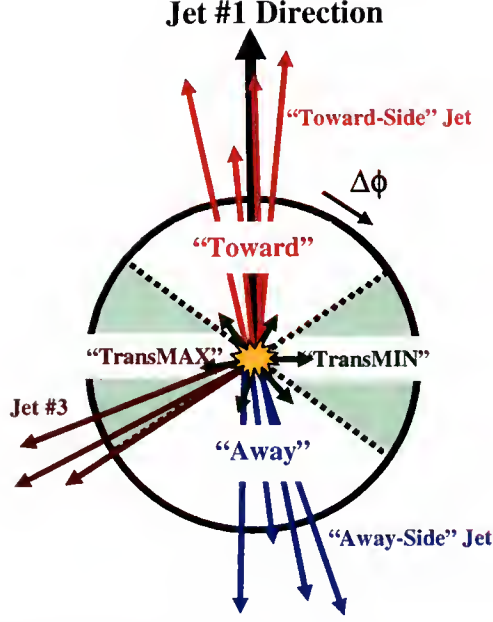


Figure 6-4: Illustration of the topology of a proton-antiproton collision in which a “hard” parton-parton collision has occurred. The “toward” region as defined in Fig. 6-1 contains the leading “jet”, while the “away” region, on the average, contains the “away-side” “jet”. The “transverse” region is perpendicular to the plane of the hard 2-to-2 scattering and is very sensitive to the “underlying event”. For events with large initial or final-state radiation the “transMAX” region defined in Fig.6-3 would contain the third jet while both the “transMAX” and “transMIN” regions receive contributions from the beam-beam remnants (see Fig. 1-1). Thus the “transMIN” region is very sensitive to the beam-beam remnants, while the “transMAX” minus the “transMIN” is very sensitive to initial and final-state radiation.

6.1 The MAX/MIN Transverse Regions

As shown in Figure 6-3 we use the direction of the highest P_T jet in the region $|\eta| < 2$, jet#1, to define the two “transverse” regions, $60^\circ < |\Delta\phi| < 120^\circ$ and $60^\circ < -|\Delta\phi| < 120^\circ$. On an event-by-event basis, we define “transMAX” and “transMIN” to be the maximum and minimum of these two regions. “TransMAX” and “transMIN” each have an area in η - ϕ space of $\Delta\eta\Delta\phi = 4\pi/6$. When looking at multiplicities MAX and MIN refer to the number of charged particles. When we consider P_{Tsum} , then MAX and MIN refer to the scalar p_T sum of charged particles and when we consider E_{Tsum} , then MAX and MIN

refer to the scalar E_T sum of particles (or calorimeter towers). The overall “transverse” region corresponds to the average of the “transMAX” and “transMIN” densities.

As illustrated in Fig. 6-4, one expects that “transMAX” will pick up the hardest initial or final-state radiation while both “transMAX” and “transMIN” should receive “beam-beam remnant” contributions. Hence one expects “transMIN” to be more sensitive to the “beam-beam remnant” component of the “underlying event”. This idea, was first suggested by Bryan Webber, and implemented by in a paper by Jon Pumplin [7,51-53]. Also, Valaria Tano [54, 55] studied this in her Run 1 analysis of maximum and minimum transverse cones ($R = 0.7$).

6.2 “Leading Jet” Events

Figures 6-5 thru 6-13 show the data on the observables in Table 4-3 at 1.96 TeV for “leading jet” events defined in Fig. 6-3 as a function of the leading jet P_T compared with PYTHIA Tune A and HERWIG. The plots show the uncorrected data (with statistical errors only) compared with the theory after detector simulation (CDFSIM). The plots also shows the data corrected to the particle level (with errors that include both the statistical error and the systematic uncertainty as described in Table 5-4) compared with the theory at the particle level (*i.e.* generator level).

Figures 6-5 thru 6-8 reflect a common trend in the data. HERWIG is consistently below the data and PYTHIA Tune A for leading jet P_T less than about 150 GeV. It is interesting, however, that HERWIG agrees well for $P_T(\text{jet}\#1) > 150$ GeV for the average density of charged particles and average charged PT_{sum} density. The “transMIN” densities are more sensitive to the “beam-beam remnant” and multiple parton interaction

components of the “underlying event” and PYHTIA Tune A (with multiple parton interactions) does a better job describing the data than HERWIG (without multiple parton interactions).

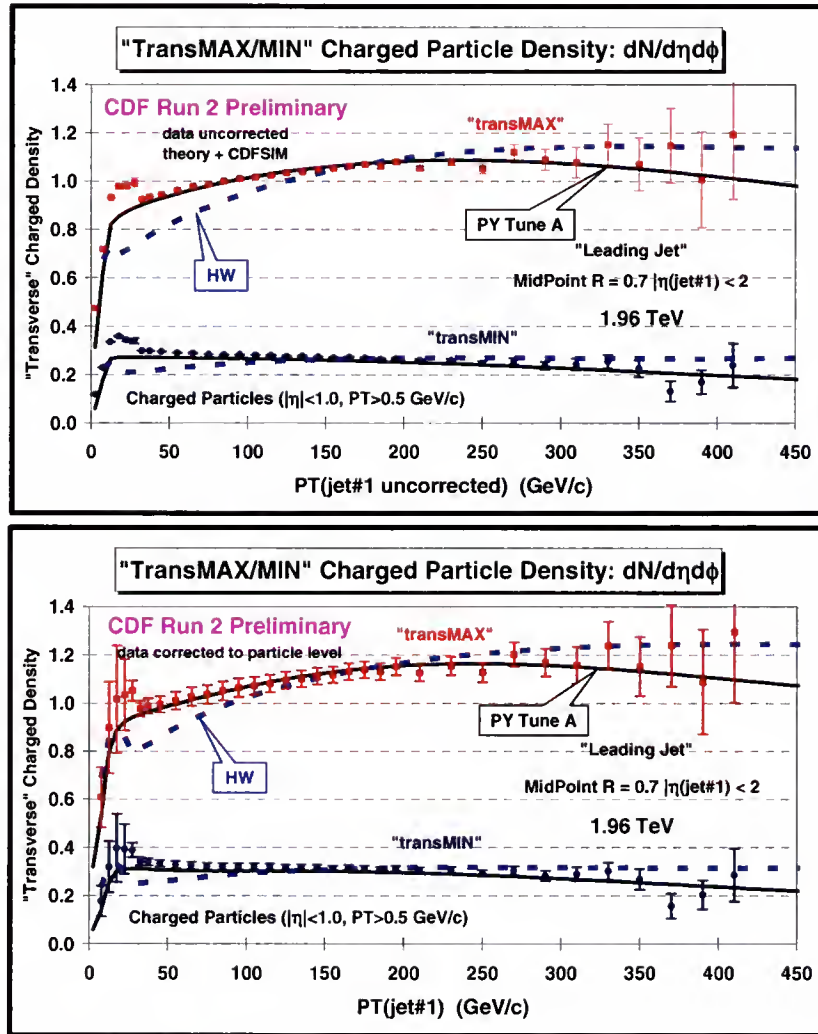


Figure 6-5: Data at 1.96 TeV on the density of charged particles, $dN_{\text{chg}}/d\eta d\phi$, with $p_T > 0.5$ GeV/c and $|\eta| < 1$ in the “transMAX” and “transMIN” regions for “leading jet” events defined in Fig. 6-3 as a function of the leading jet P_T compared with PYTHIA Tune A and HERWIG. (*top*) Shows the uncorrected data (with statistical errors only) compared with the theory after detector simulation (CDFSIM). (*bottom*) Shows the data corrected to the particle level (with errors that include both the statistical error and the systematic uncertainty) compared with the theory at the particle level (*i.e.* generator level).

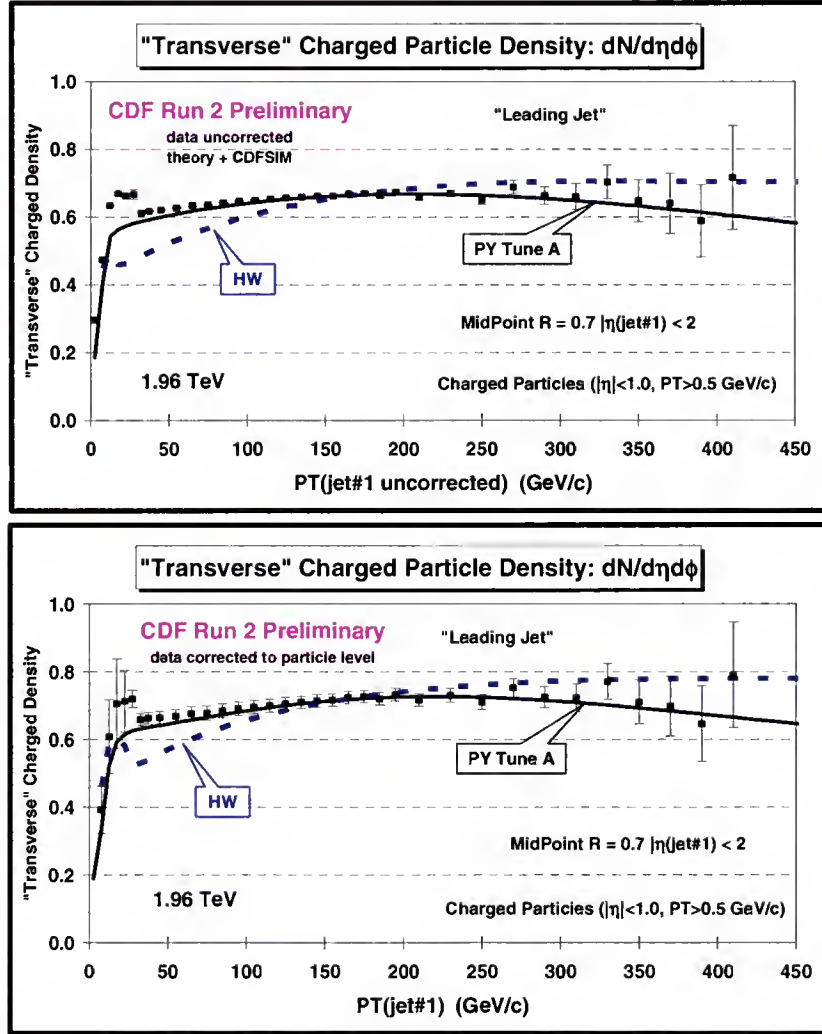


Figure 6-6: Data at 1.96 TeV on the density of charged particles, $dN_{\text{chg}}/d\eta d\phi$, with $p_T > 0.5$ GeV/c and $|\eta| < 1$ in the “transverse” region (average of “transMAX” and “transMIN”) for “leading jet” events defined in Fig. 6-3 as a function of the leading jet P_T compared with PYTHIA Tune A and HERWIG. (*top*) Shows the uncorrected data (with statistical errors only) compared with the theory after detector simulation (CDFSIM). (*bottom*) Shows the data corrected to the particle level (with errors that include both the statistical error and the systematic uncertainty) compared with the theory at the particle level (*i.e.* generator level).

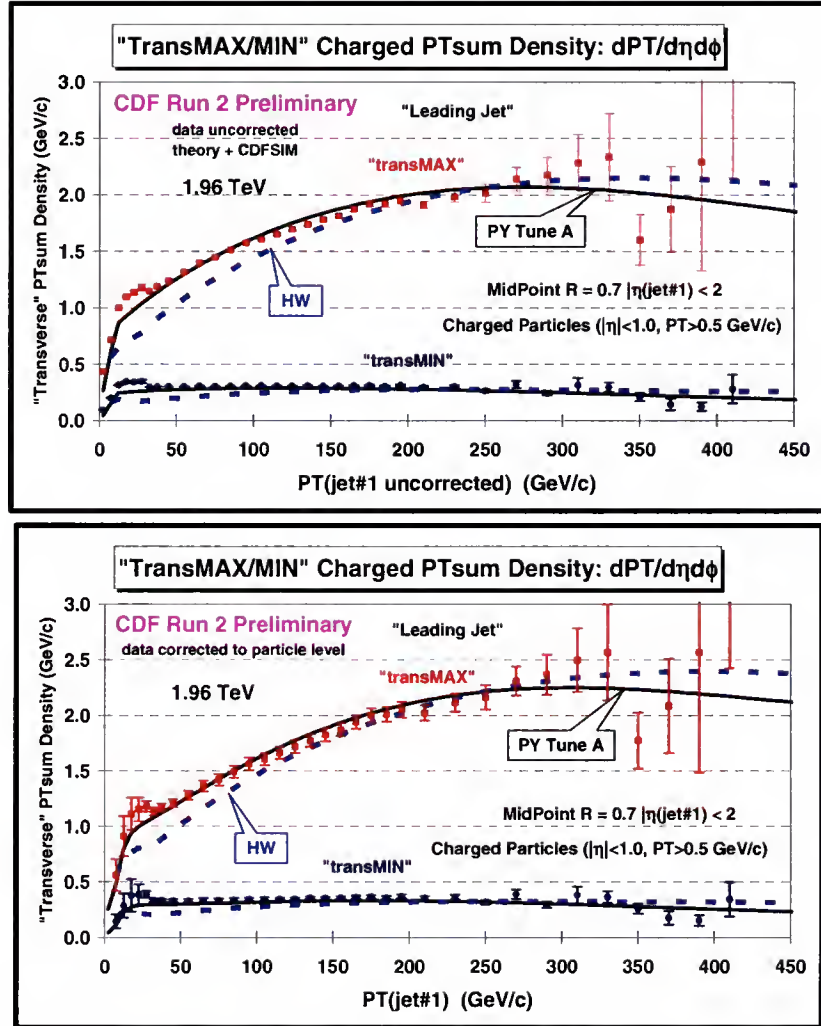


Figure 6-7: Data at 1.96 TeV on the PTsum density of charged particles, $dPT_{\text{sum}}/d\eta d\phi$, with $p_T > 0.5 \text{ GeV/c}$ and $|\eta| < 1$ in the "transMAX" and "transMIN" regions for "leading jet" events defined in Fig. 6-3 as a function of the leading jet P_T compared with PYTHIA Tune A and HERWIG. (*top*) Shows the uncorrected data (with statistical errors only) compared with the theory after detector simulation (CDFSIM). (*bottom*) Shows the data corrected to the particle level (with errors that include both the statistical error and the systematic uncertainty) compared with the theory at the particle level (*i.e.* generator level).

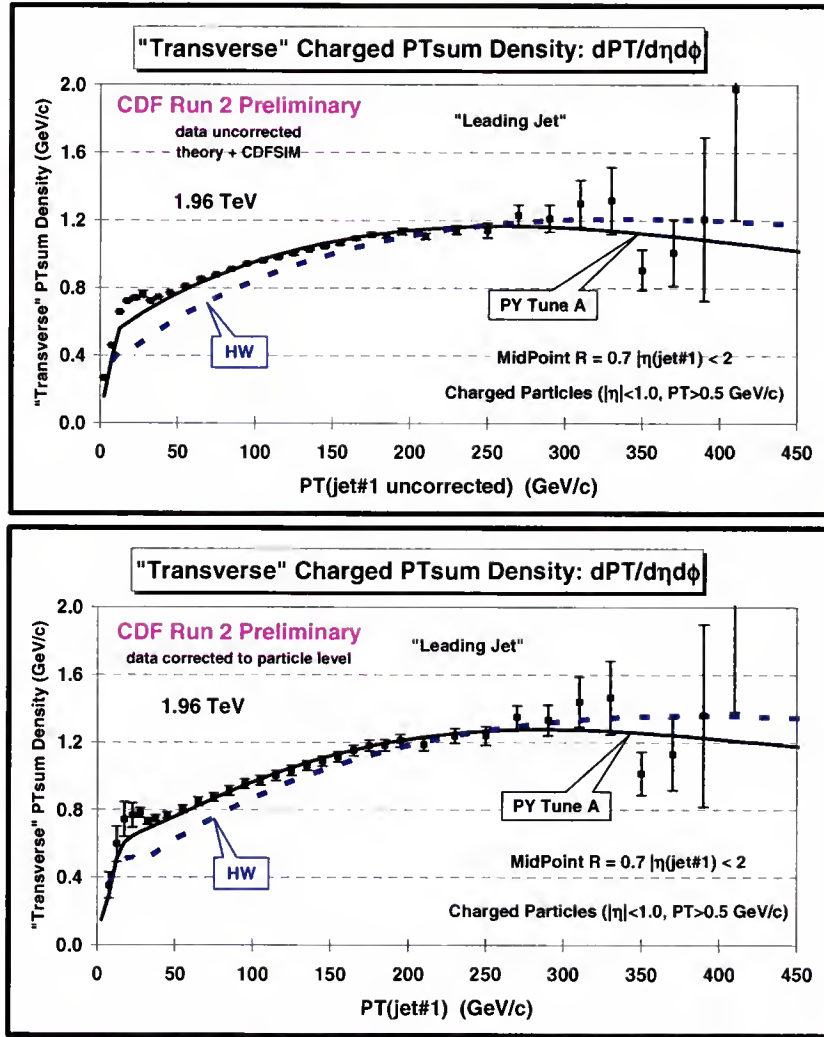


Figure 6-8: Data at 1.96 TeV on the charged PTsum density, $dPT_{sum}/d\eta d\phi$, with $p_T > 0.5$ GeV/c and $|\eta| < 1$ in the “transverse” region (average of “transMAX” and “transMIN”) for “leading jet” events defined in Fig. 6-3 as a function of the leading jet P_T compared with PYTHIA Tune A and HERWIG. (*top*) Shows the uncorrected data (with statistical errors only) compared with the theory after detector simulation (CDFSIM). (*bottom*) Shows the data corrected to the particle level (with errors that include both the statistical error and the systematic uncertainty) compared with the theory at the particle level (*i.e.* generator level).

Figure 6-9 compares PYTHIA Tune A and HERWIG with the data on the average $\langle p_T \rangle$ of charged particles in the “transverse” region for “leading jet” events defined in Fig. 6-3 as a function of the leading jet P_T . The top shows the uncorrected data (with statistical errors only) compared with the theory after detector simulation (CDFSIM),

while the bottom shows the data corrected to the particle level (with errors that include both the statistical error and the systematic uncertainty) compared with the theory at the particle level (*i.e.* generator level). HERWIG, even after the data is corrected, predicts a softer average $\langle p_T \rangle$ of charged particles in the “transverse” region for “leading jet” events defined in Fig. 6-3 as a function of the leading jet P_T .

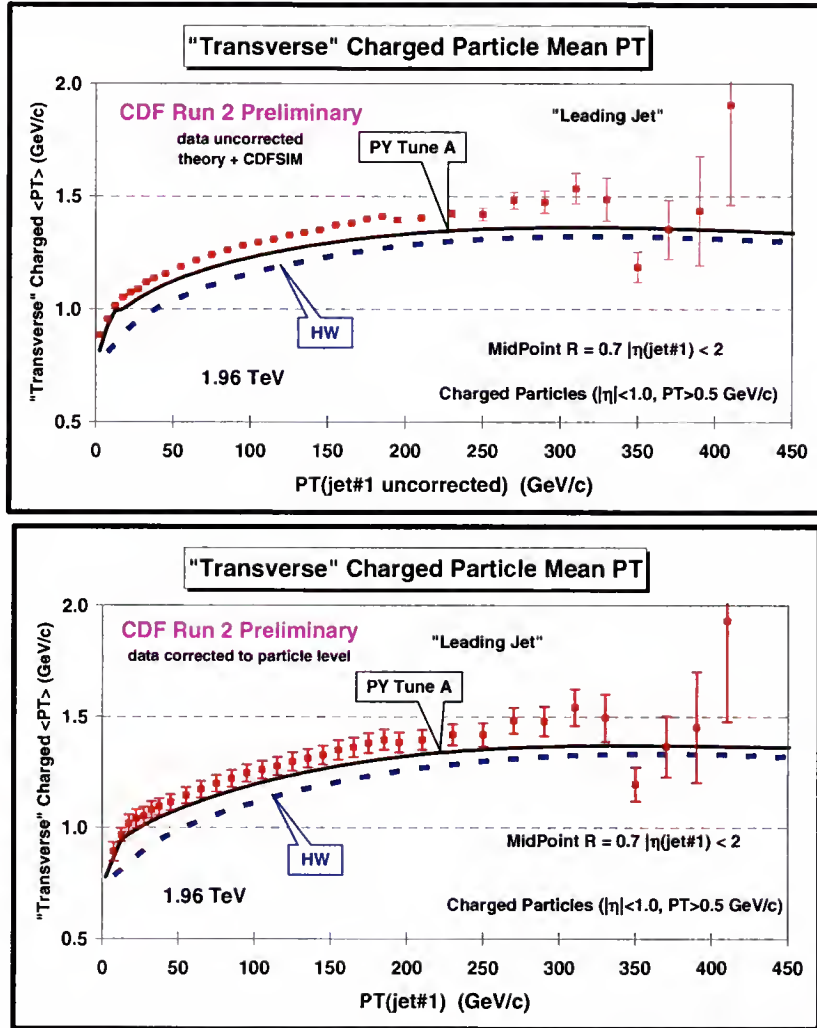


Figure 6-9: Data at 1.96 TeV on the average $\langle p_T \rangle$ of charged particles with $p_T > 0.5$ GeV/c and $|\eta| < 1$ in the “transverse” region for “leading jet” events defined in Fig. 6-3 as a function of the leading jet P_T compared with PYTHIA Tune A and HERWIG. (*top*) Shows the uncorrected data (with statistical errors only) compared with the theory after detector simulation (CDFSIM). (*bottom*) Shows the data corrected to the particle level (with errors that include both the statistical error and the systematic uncertainty) compared with the theory at the particle level (*i.e.* generator level).

Figure 6-10 compares PYTHIA Tune A and HERWIG with the data on the average maximum p_T , PT_{max} , for charged particles in the “transverse” region for “leading jet” events defined in Fig. 6-3 as a function of the leading jet P_T . The top shows the uncorrected data (with statistical errors only) compared with the theory after detector simulation (CDFSIM), while the bottom shows the data corrected to the particle level (with errors that include both the statistical error and the systematic uncertainty) compared with the theory at the particle level (*i.e.* generator level). The agreement is better than for the average $\langle p_T \rangle$, but HERWIG is still too soft for leading jet P_T less than about 150 GeV.

Figures 6-11 and 6-12 compare PYTHIA Tune A and HERWIG with the data on the the ETsum density, $dE_T/d\eta d\phi$, for particles with $|\eta| < 1$ in the transverse region for “leading jet” events defined in Fig. 6-3 as a function of the leading jet P_T . The top shows the uncorrected data (with statistical errors only) compared with the theory after detector simulation (CDFSIM), while the bottom shows the data corrected to the particle level (with errors that include both the statistical error and the systematic uncertainty) compared with the theory at the particle level (*i.e.* generator level). Both PYTHIA Tune A and HERWIG fall below the data throughout the energy range.

Figure 6-13 compares PYTHIA Tune A and HERWIG with the data at on the charged fraction, PT_{sum}/ET_{sum} , in the “transverse” region for “leading jet” events defined in Fig. 6-3 as a function of the leading jet P_T , where PT_{sum} includes charged particles with $p_T > 0.5$ GeV/c and $|\eta| < 1$ and the ET_{sum} includes all particles with $|\eta| < 1$. The top shows the uncorrected data (with statistical errors only) compared with the theory after detector simulation (CDFSIM), while the bottom shows the data corrected to

the particle level (with errors that include both the statistical error and the systematic uncertainty) compared with the theory at the particle level (*i.e.* generator level). Both MC generators predict a larger charged fraction in the transverse region than is indicated by the data.

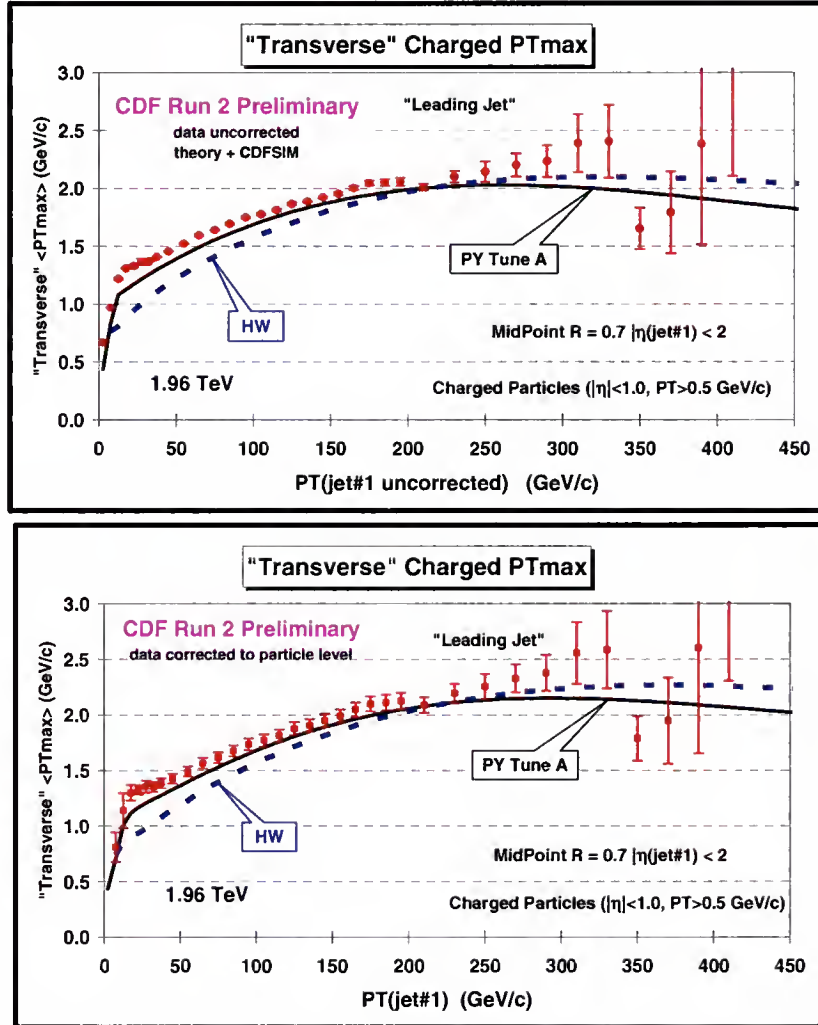


Figure 6-10: Data at 1.96 TeV on the average maximum p_T , PT_{max} , for charged particles with $p_T > 0.5$ GeV/c and $|\eta| < 1$ in the "transverse" region for "leading jet" events defined in Fig. 6-3 as a function of the leading jet P_T compared with PYTHIA Tune A and HERWIG. (*top*) Shows the uncorrected data (with statistical errors only) compared with the theory after detector simulation (CDFSIM). (*bottom*) Shows the data corrected to the particle level (with errors that include both the statistical error and the systematic uncertainty) compared with the theory at the particle level (*i.e.* generator level).

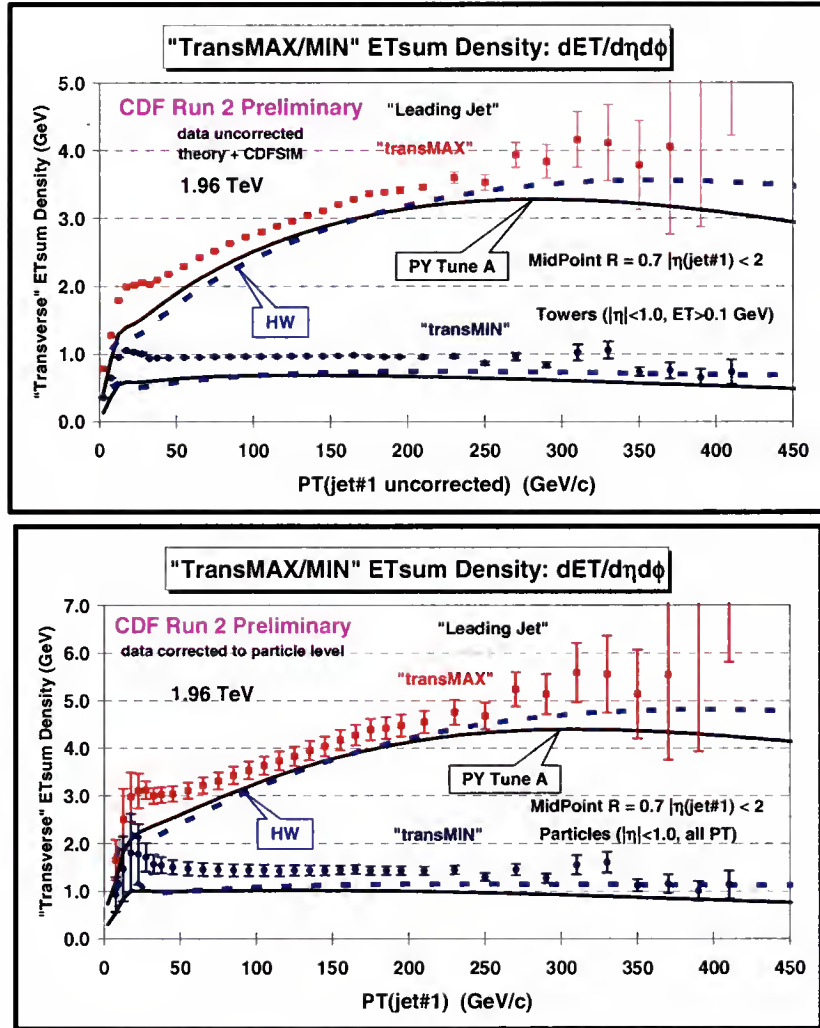


Figure 6-11: Data at 1.96 TeV on the ETsum density, $dE_T/d\eta d\phi$, for particles with $|\eta| < 1$ in the "transMAX" and "transMIN" regions for "leading jet" events defined in Fig. 6-3 as a function of the leading jet P_T compared with PYTHIA Tune A and HERWIG. (top) Shows the uncorrected data (with statistical errors only) compared with the theory after detector simulation (CDFSIM). (bottom) Shows the data corrected to the particle level (with errors that include both the statistical error and the systematic uncertainty) compared with the theory at the particle level (*i.e.* generator level).

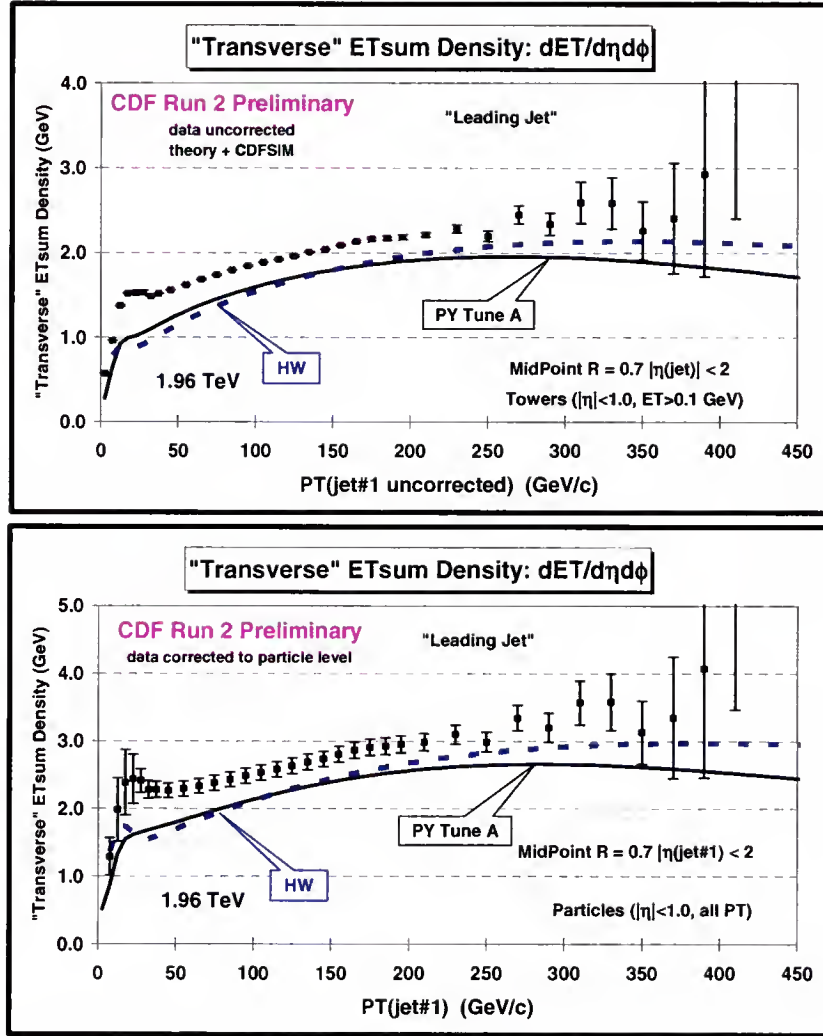


Figure 6-12: Data at 1.96 TeV on the ETsum density, $dE_T/d\eta d\phi$, for particles with $|\eta| < 1$ in the “transverse” region (average of “transMAX” and “transMIN”) for “leading jet” events defined in Fig. 6-3 as a function of the leading jet P_T compared with PYTHIA Tune A and HERWIG. (*top*) Shows the uncorrected data (with statistical errors only) compared with the theory after detector simulation (CDFSIM). (*bottom*) Shows the data corrected to the particle level (with errors that include both the statistical error and the systematic uncertainty) compared with the theory at the particle level (*i.e.* generator level).

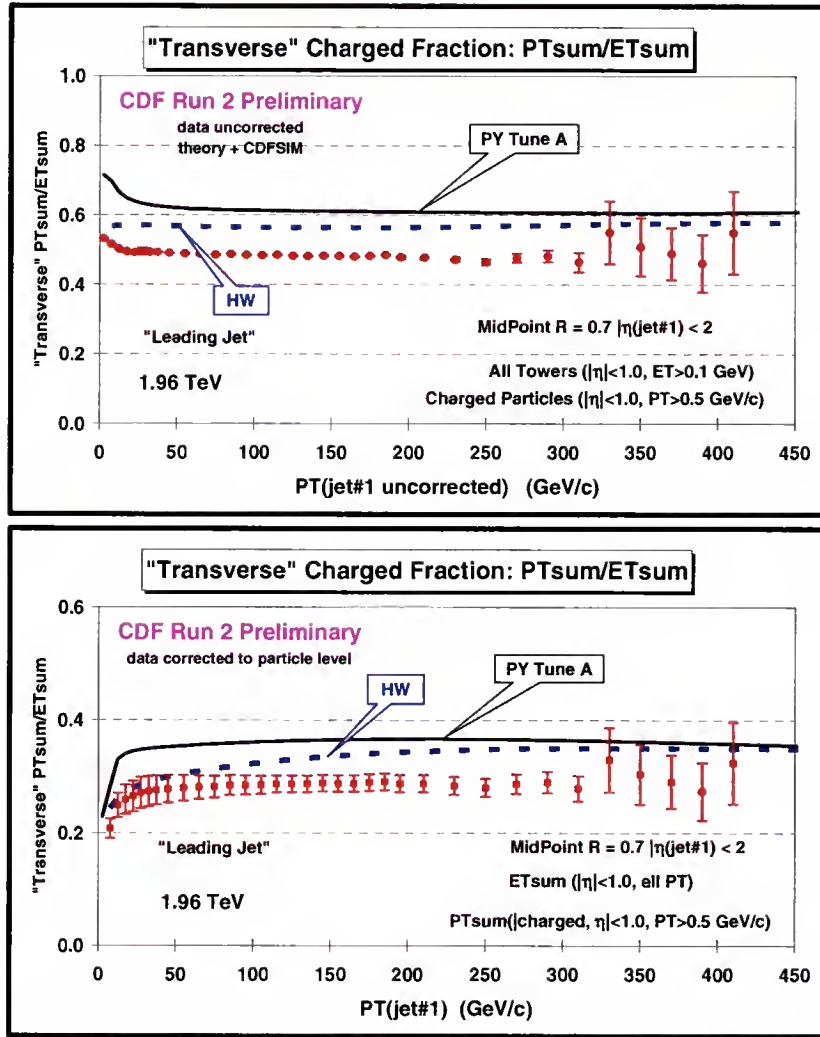


Figure 6-13: Data at 1.96 TeV on the charged fraction, $PT_{\text{sum}}/ET_{\text{sum}}$, in the “transverse” region for “leading jet” events defined in Fig. 6-3 as a function of the leading jet P_T , where PT_{sum} includes charged particles with $p_T > 0.5$ GeV/c and $|\eta| < 1$ and the ET_{sum} includes all particles with $|\eta| < 1$. The data are compared with PYTHIA Tune A and HERWIG. (*top*) Shows the uncorrected data (with statistical errors only) compared with the theory after detector simulation (CDFSIM). (*bottom*) Shows the data corrected to the particle level (with errors that include both the statistical error and the systematic uncertainty) compared with the theory at the particle level (*i.e.* generator level).

6.3 “Back-to-Back” Events

Figure 6-14 thru 6-22 show the data on the observables in Table 4-3 at 1.96 TeV for “back-to-back” events defined in Fig. 6-3 as a function of the leading jet P_T compared with PYTHIA Tune A and HERWIG. The plots show the uncorrected data (with

statistical errors only) compared with the theory after detector simulation (CDFSIM). The plots also shows the data corrected to the particle level (with errors that include both the statistical error and the systematic uncertainty as described in Table 5-4) compared with the theory at the particle level (*i.e.* generator level).

Figures 6-14 thru 6-17 continue to exhibit the trend that HERWIG is consistently below the data and PYTHIA Tune A for leading jet P_T less than about 150 GeV. However, the back-to-back data reveal that the densities fall with increasing $P_T(\text{jet\#1})$. Since the hard initial and final-state radiation is suppressed in back-to-back events the differences between PYHTIA Tune A and HERWIG in the “beam-beam remnant” and multiple parton scattering component of the “underlying event” are more evident. PYHTIA Tune A (with multiple parton interactions) does a better job describing the scale and slope of the data than HERWIG (without multiple parton interactions).

Figure 6-18 compares PYTHIA Tune A and HERWIG with the data on the average $\langle p_T \rangle$ of charged particles with $p_T > 0.5 \text{ GeV}/c$ and $|\eta| < 1$ in the “transverse” region for “back-to-back” events defined in Fig. 6-3 as a function of the leading jet P_T . The top shows the uncorrected data (with statistical errors only) compared with the theory after detector simulation (CDFSIM), while the bottom shows the data corrected to the particle level (with errors that include both the statistical error and the systematic uncertainty) compared with the theory at the particle level (*i.e.* generator level). Both PYTHIA Tune A and HERWIG predict a softer average $\langle p_T \rangle$ of charged particles than is exhibited by the data.

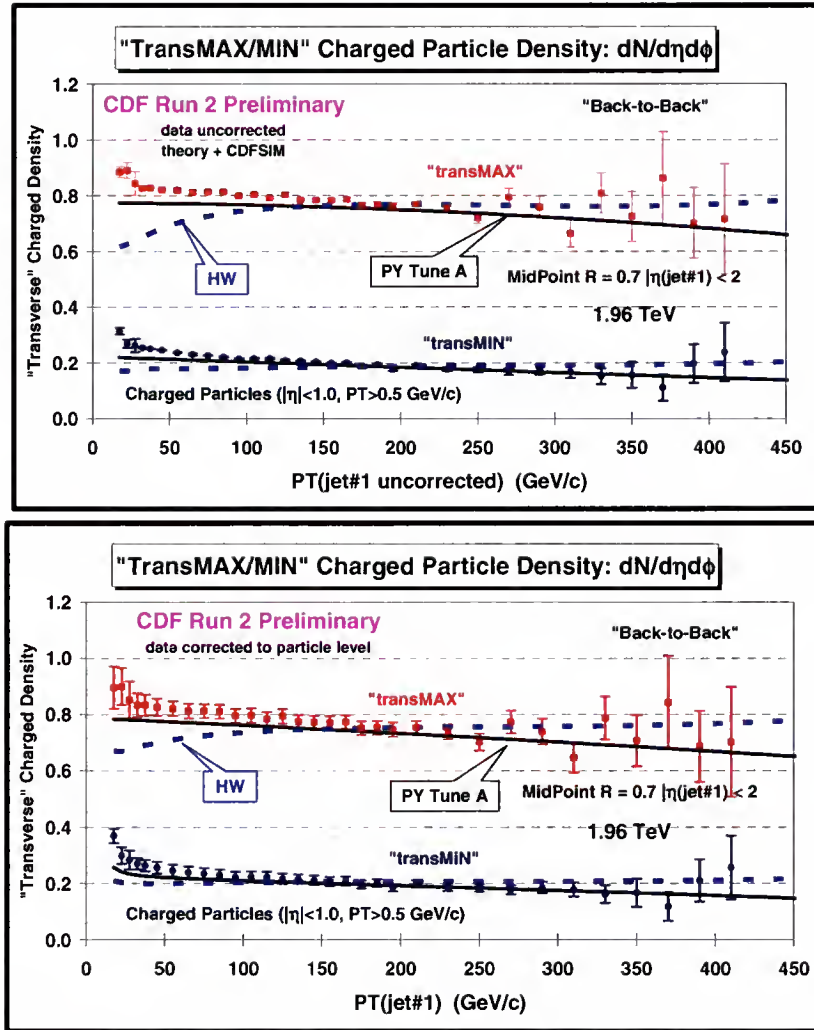


Figure 6-14: Data at 1.96 TeV on the density of charged particles, $dN_{chg}/d\eta d\phi$, with $p_T > 0.5$ GeV/c and $|\eta| < 1$ in the "transMAX" and "transMIN" regions for "back-to-back" events defined in Fig. 6-3 as a function of the leading jet P_T compared with PYTHIA Tune A and HERWIG. (top) Shows the uncorrected data (with statistical errors only) compared with the theory after detector simulation (CDFSIM). (bottom) Shows the data corrected to the particle level (with errors that include both the statistical error and the systematic uncertainty) compared with the theory at the particle level (*i.e.* generator level).

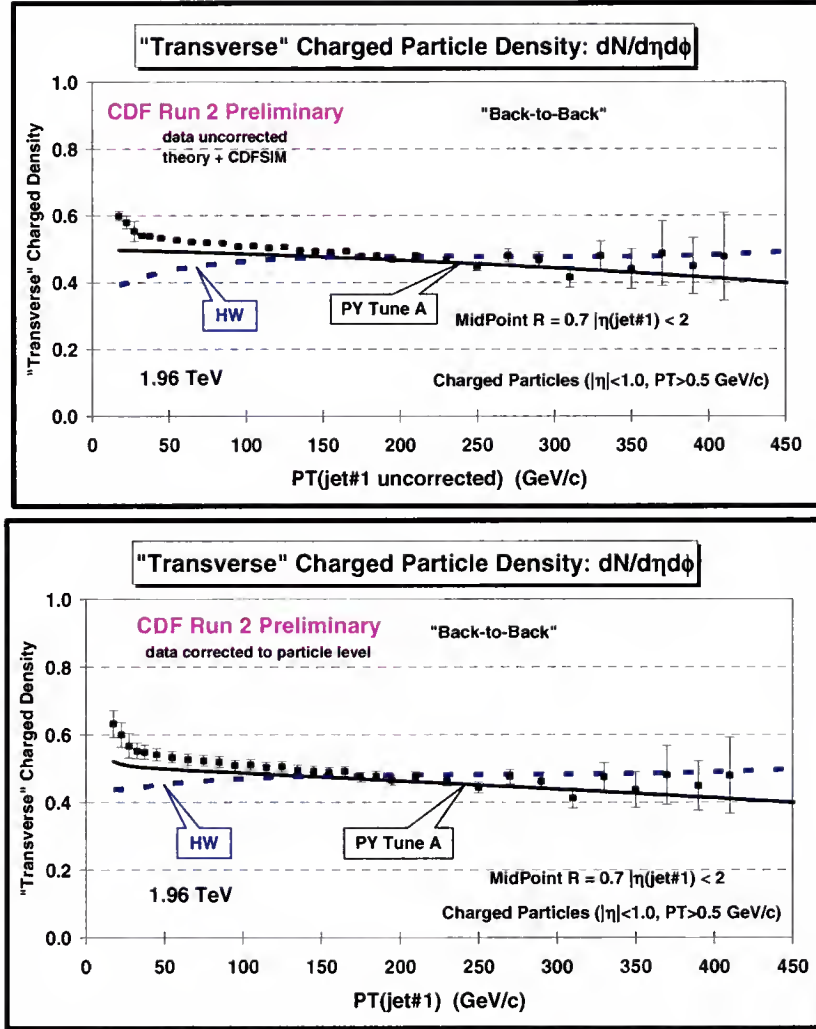


Figure 6-15: Data at 1.96 TeV on the density of charged particles, $dN_{chg}/d\eta d\phi$, with $p_T > 0.5$ GeV/c and $|\eta| < 1$ in the “transverse” region (average of “transMAX” and “transMIN”) for “back-to-back” events defined in Fig. 6-3 as a function of the leading jet P_T compared with PYTHIA Tune A and HERWIG. (top) Shows the uncorrected data (with statistical errors only) compared with the theory after detector simulation (CDFSIM). (bottom) Shows the data corrected to the particle level (with errors that include both the statistical error and the systematic uncertainty) compared with the theory at the particle level (*i.e.* generator level).

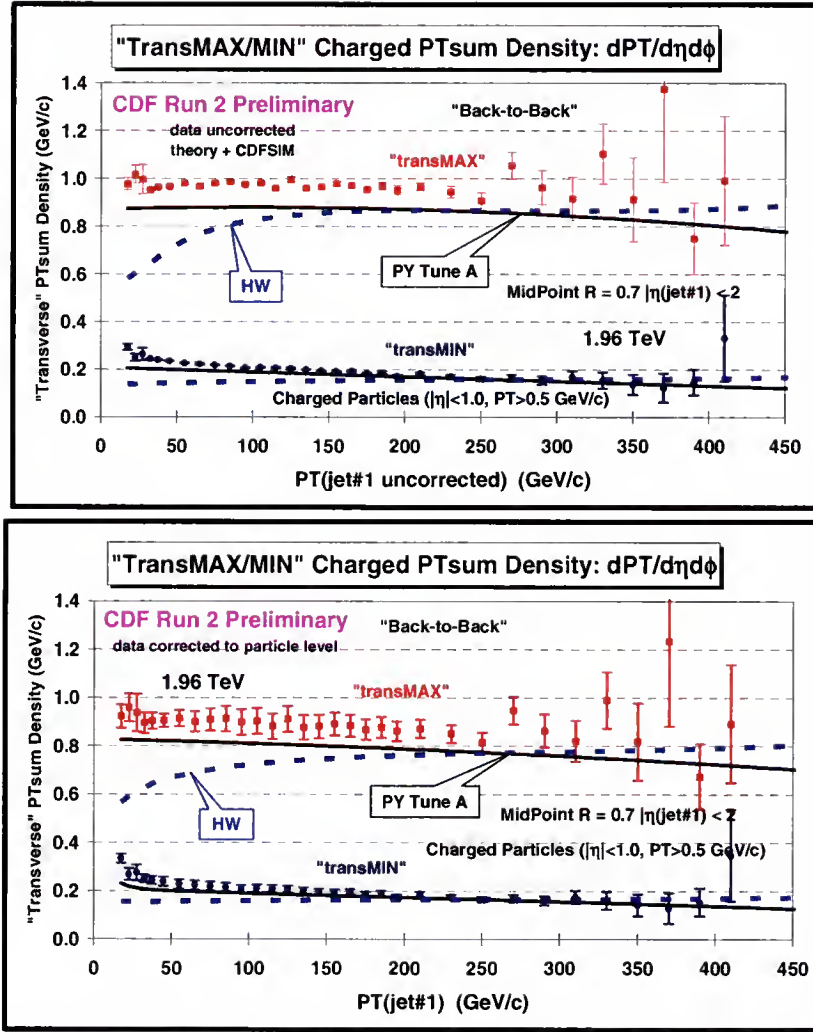


Figure 6-16: Data at 1.96 TeV on the PTsum density of charged particles, $dPT_{\text{sum}}/d\eta d\phi$, with $p_T > 0.5$ GeV/c and $|\eta| < 1$ in the "transMAX" and "transMIN" regions for "back-to-back" events defined in Fig. 6-3 as a function of the leading jet P_T compared with PYTHIA Tune A and HERWIG. (*top*) Shows the uncorrected data (with statistical errors only) compared with the theory after detector simulation (CDFSIM). (*bottom*) Shows the data corrected to the particle level (with errors that include both the statistical error and the systematic uncertainty) compared with the theory at the particle level (*i.e.* generator level).

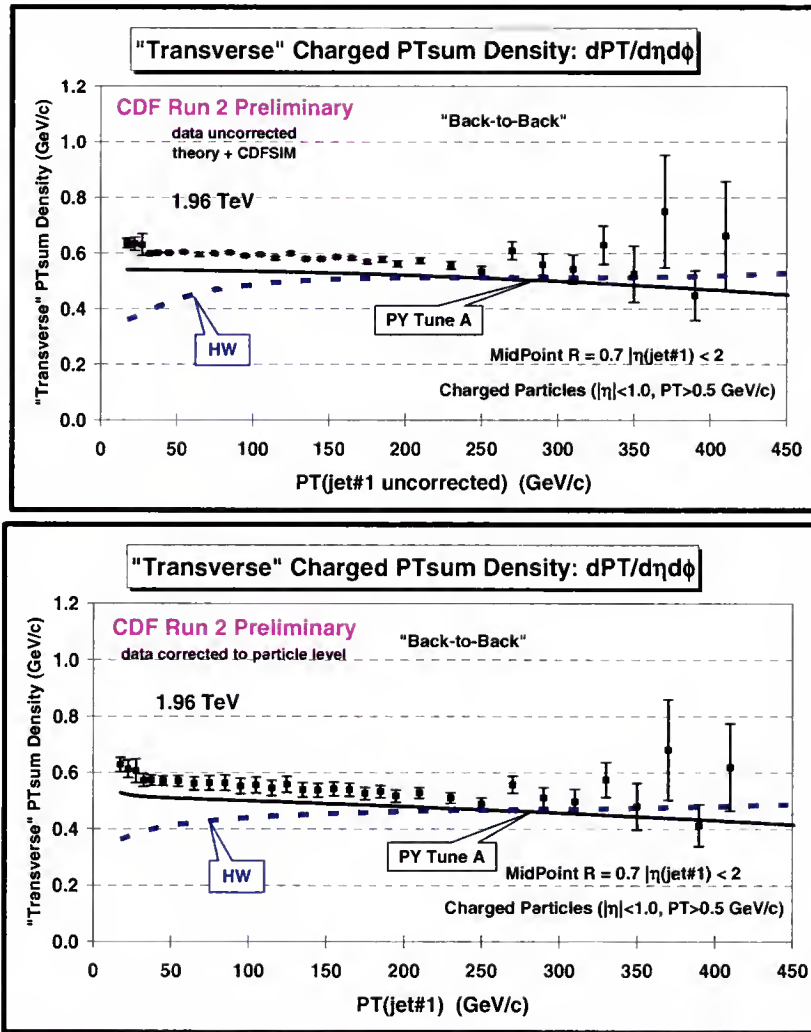


Figure 6-17: Data at 1.96 TeV on the PTsum density, $dPT_{\text{sum}}/d\eta d\phi$, with $p_T > 0.5$ GeV/c and $|\eta| < 1$ in the “transverse” region (average of “transMAX” and “transMIN”) for “back-to-back” events defined in Fig. 6-3 as a function of the leading jet P_T compared with PYTHIA Tune A and HERWIG. (top) Shows the uncorrected data (with statistical errors only) compared with the theory after detector simulation (CDFSIM). (bottom) Shows the data corrected to the particle level (with errors that include both the statistical error and the systematic uncertainty) compared with the theory at the particle level (i.e. generator level).

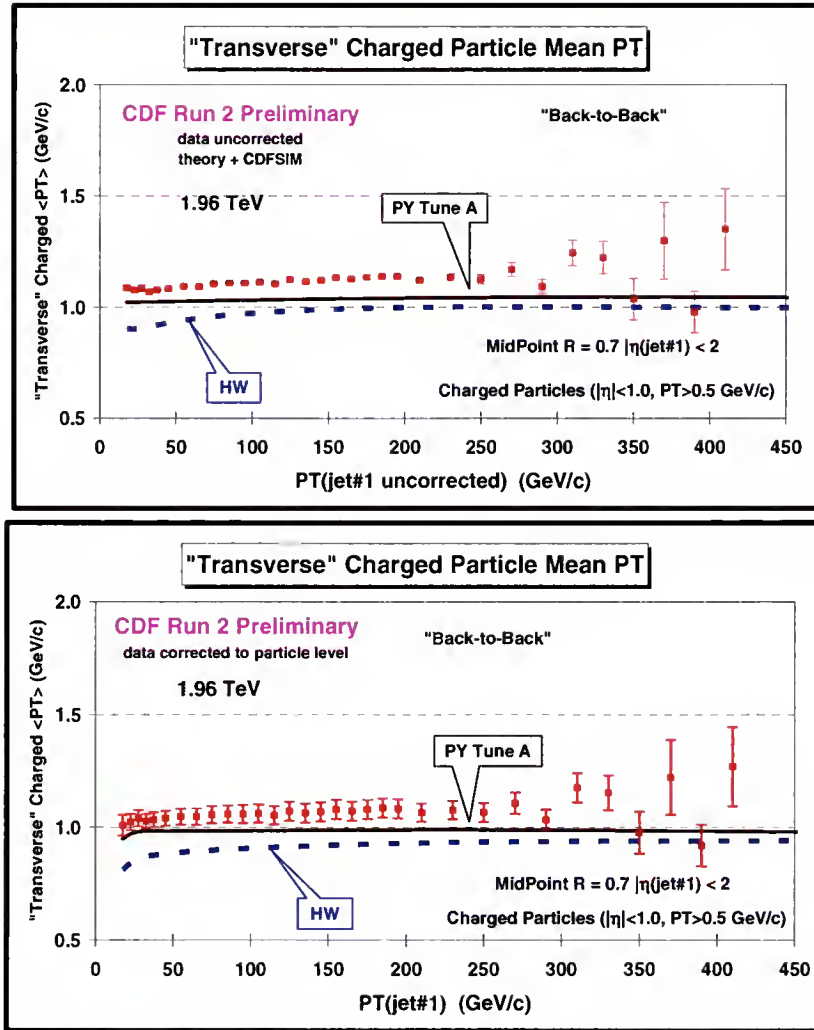


Figure 6-18: Data at 1.96 TeV on the average $\langle p_T \rangle$ of charged particles with $p_T > 0.5$ GeV/c and $|\eta| < 1$ in the “transverse” region for “back-to-back” events defined in Fig. 6-3 as a function of the leading jet P_T compared with PYTHIA Tune A and HERWIG. (*top*) Shows the uncorrected data (with statistical errors only) compared with the theory after detector simulation (CDFSIM). (*bottom*) Shows the data corrected to the particle level (with errors that include both the statistical error and the systematic uncertainty) compared with the theory at the particle level (*i.e.* generator level).

Figure 6-19 compares PYTHIA Tune A and HERWIG with the data on the average maximum p_T , PT_{max} , for charged particles with $p_T > 0.5$ GeV/c and $|\eta| < 1$ in the “transverse” region for “back-to-back” events defined in Fig. 6-3 as a function of the leading jet P_T . The top shows the uncorrected data (with statistical errors only) compared with the theory after detector simulation (CDFSIM), while the bottom shows the data

corrected to the particle level (with errors that include both the statistical error and the systematic uncertainty) compared with the theory at the particle level (*i.e.* generator level). Both MC generators predict a too soft average maximum p_T , but only PYTHIA Tune A correctly reproduces the decreasing slope of the observable.

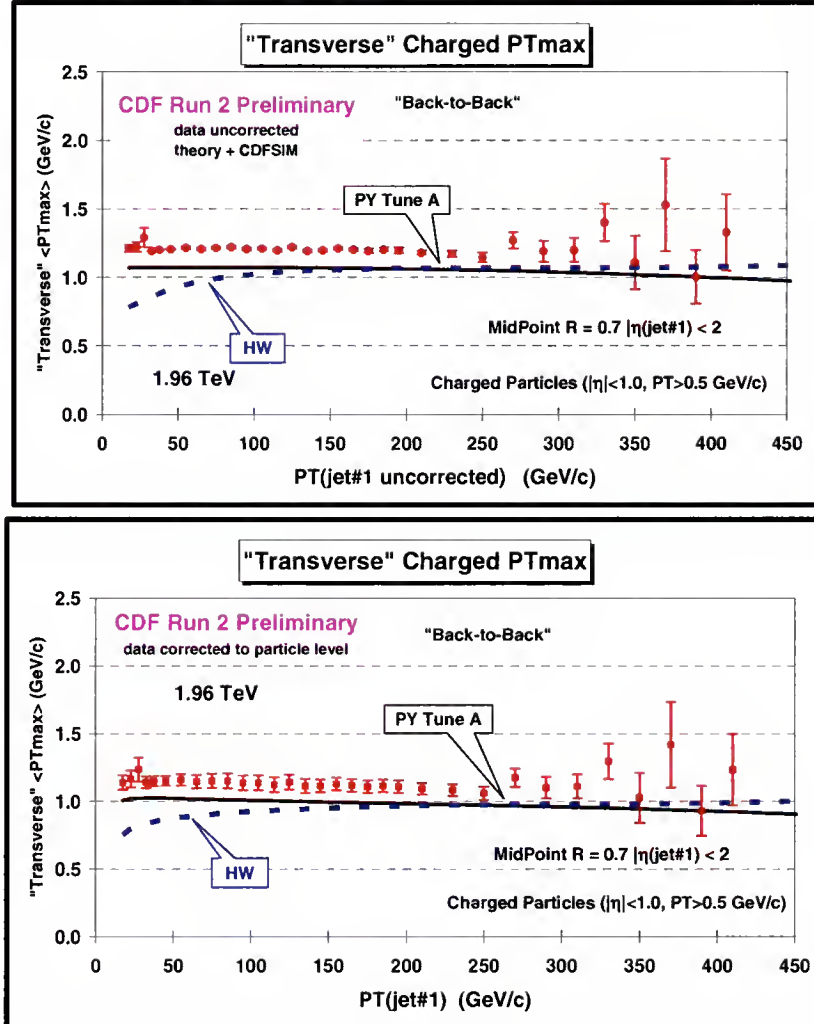


Figure 6-19: Data at 1.96 TeV on the average maximum p_T , PT_{max} , for charged particles with $p_T > 0.5$ GeV/c and $|\eta| < 1$ in the “transverse” region for “back-to-back” events defined in Fig. 6-3 as a function of the leading jet P_T compared with PYTHIA Tune A and HERWIG. (*top*) Shows the uncorrected data (with statistical errors only) compared with the theory after detector simulation (CDFSIM). (*bottom*) Shows the data corrected to the particle level (with errors that include both the statistical error and the systematic uncertainty) compared with the theory at the particle level (*i.e.* generator level).

Figures 6-20 and 6-21 compare PYTHIA Tune A and HERWIG with the data on the ETsum density, $dE_T/d\eta d\phi$, for particles with $|\eta| < 1$ in the transverse region for “back-to-back” events defined in Fig. 6-3 as a function of the leading jet P_T . The top shows the uncorrected data (with statistical errors only) compared with the theory after detector simulation (CDFSIM), while the bottom shows the data corrected to the particle level (with errors that include both the statistical error and the systematic uncertainty) compared with the theory at the particle level (*i.e.* generator level). Both MC generators predict too little ETsum density, but only PYTHIA Tune A correctly reproduces the decreasing slope of the observable.

Figure 6-22 compares PYTHIA Tune A and HERWIG with the data on the charged fraction, $PT_{\text{sum}}/ET_{\text{sum}}$, in the “transverse” region for “back-to-back” events defined in Fig. 6-3 as a function of the leading jet P_T , where PT_{sum} includes charged particles with $p_T > 0.5 \text{ GeV}/c$ and $|\eta| < 1$ and the ET_{sum} includes all particles with $|\eta| < 1$. The top shows the uncorrected data (with statistical errors only) compared with the theory after detector simulation (CDFSIM), while the bottom shows the data corrected to the particle level (with errors that include both the statistical error and the systematic uncertainty) compared with the theory at the particle level (*i.e.* generator level). Both MC generators predict a larger charged fraction in the transverse region than is indicated by the data.

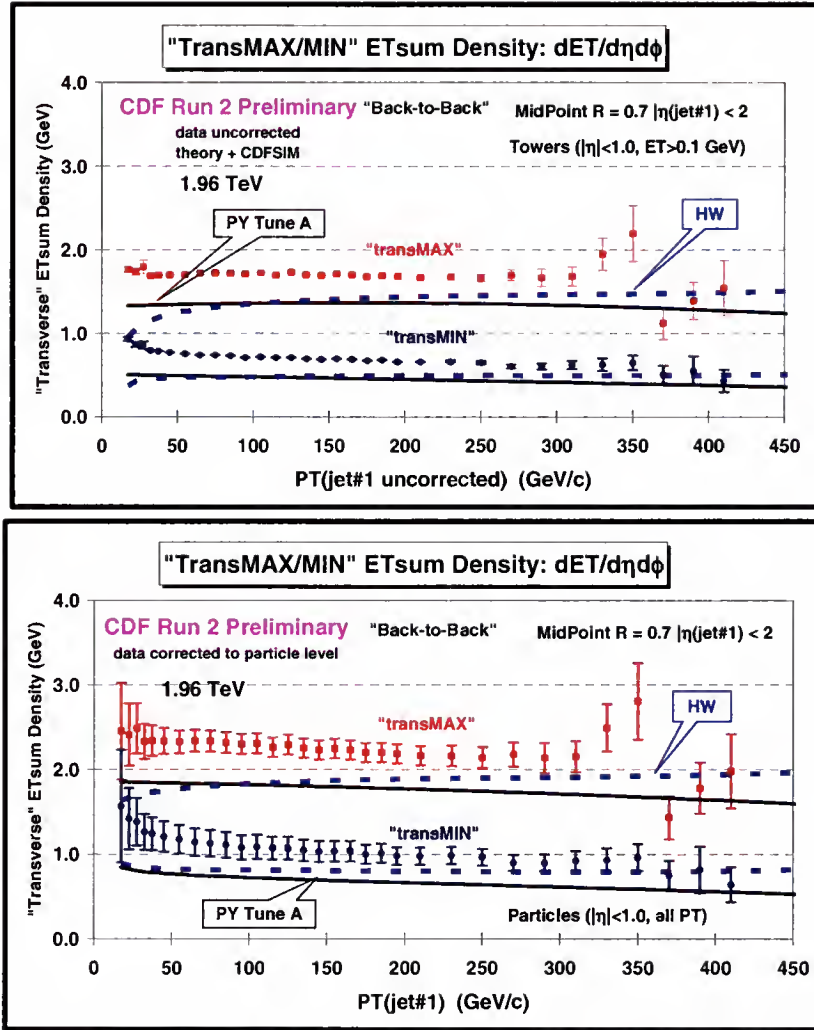


Figure 6-20: Data at 1.96 TeV on the ETsum density, $dE_T/d\eta d\phi$, for particles with $|\eta| < 1$ in the "transMAX" and "transMIN" regions for "back-to-back" events defined in Fig. 6-3 as a function of the leading jet P_T compared with PYTHIA Tune A and HERWIG. (*top*) Shows the uncorrected data (with statistical errors only) compared with the theory after detector simulation (CDFSIM). (*bottom*) Shows the data corrected to the particle level (with errors that include both the statistical error and the systematic uncertainty) compared with the theory at the particle level (*i.e.* generator level).

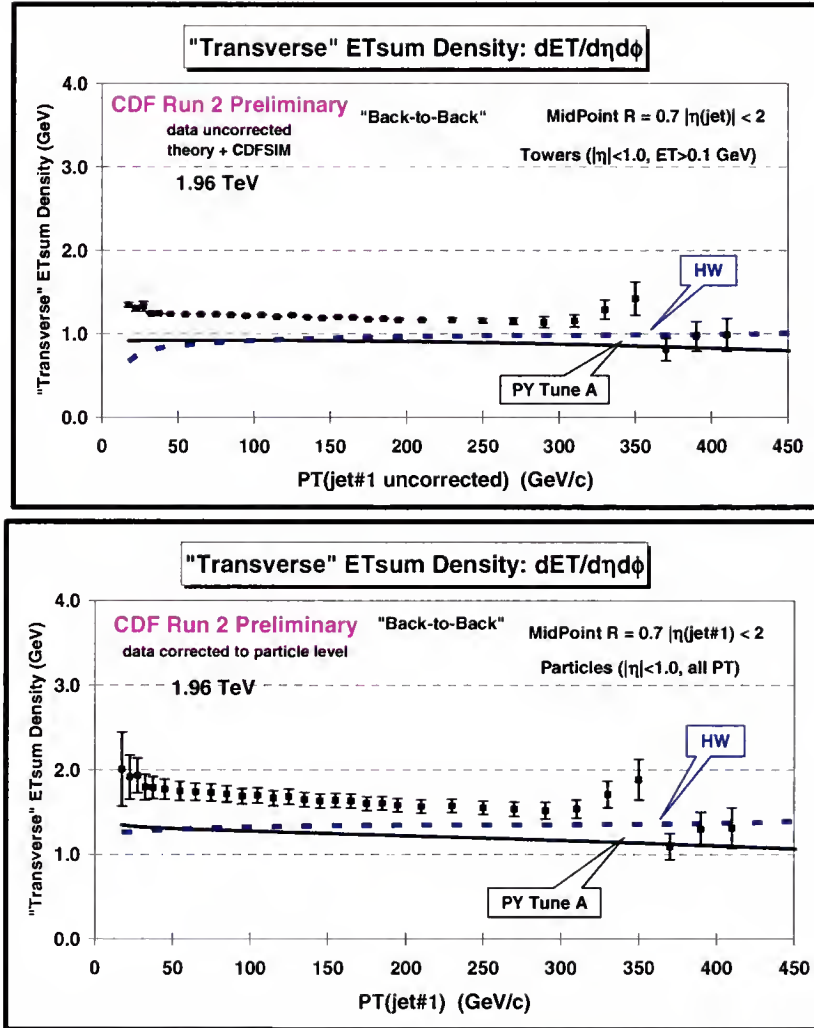


Figure 6-21: Data at 1.96 TeV on the ETsum density, $dE_T/d\eta d\phi$, for particles with $|\eta| < 1$ in the “transverse” region (average of “transMAX” and “transMIN”) for “back-to-back” events defined in Fig. 6-3 as a function of the leading jet P_T compared with PYTHIA Tune A and HERWIG. (top) Shows the uncorrected data (with statistical errors only) compared with the theory after detector simulation (CDFSIM). (bottom) Shows the data corrected to the particle level (with errors that include both the statistical error and the systematic uncertainty) compared with the theory at the particle level (i.e. generator level).

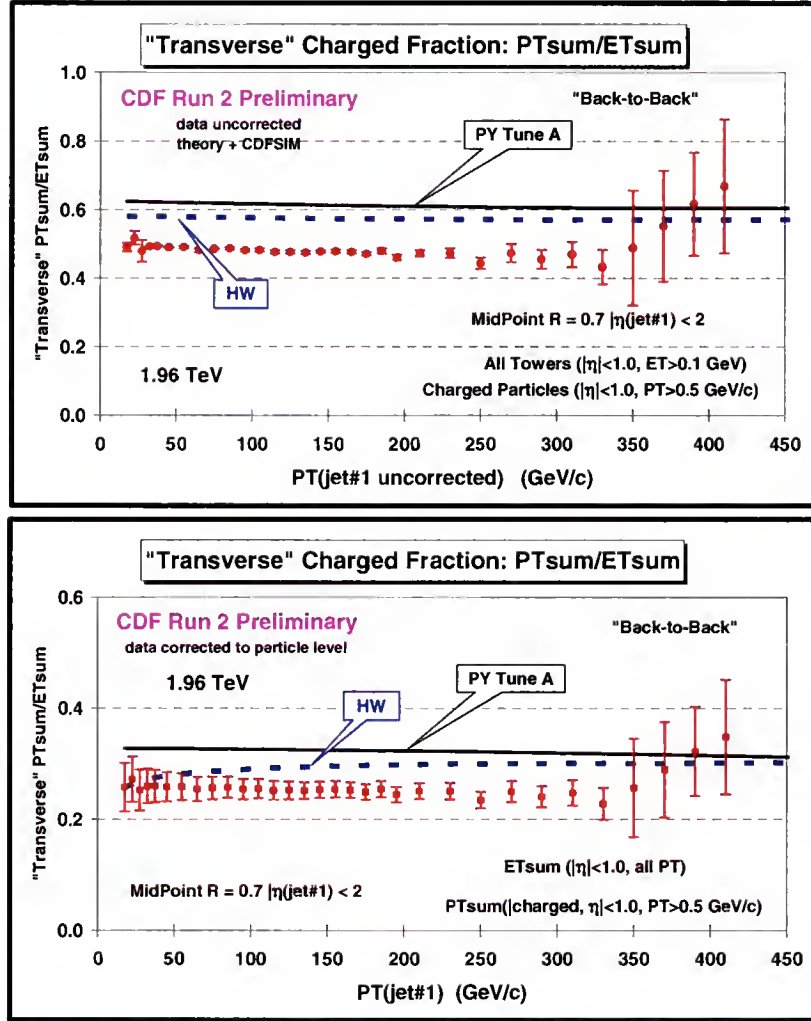


Figure 6-22: Data at 1.96 TeV on the charged fraction, PT_{sum}/ET_{sum} , in the “transverse” region for “back-to-back” events defined in Fig. 6-3 as a function of the leading jet P_T , where PT_{sum} includes charged particles with $p_T > 0.5$ GeV/c and $|\eta| < 1$ and the ET_{sum} includes all particles with $|\eta| < 1$. The data are compared with PYTHIA Tune A and HERWIG. (*top*) Shows the uncorrected data (with statistical errors only) compared with the theory after detector simulation (CDFSIM). (*bottom*) Shows the data corrected to the particle level (with errors that include both the statistical error and the systematic uncertainty) compared with the theory at the particle level (*i.e.* generator level).

6.4 “Leading Jet” versus “Back-to-Back” Events

Figure 6-23 and Figure 6-24 compare the data on the density of charged particles and the charged PT_{sum} density in the “transverse” region corrected to the particle level for “leading jet” and “back-to-back” events with PYTHIA Tune A and HERWIG at the

particle level. As expected, the “leading jet” and “back-to-back” events behave quite differently. For the “leading jet” case the “transMAX” densities rise with increasing $P_T(\text{jet}\#1)$, while for the “back-to-back” case they fall with increasing $P_T(\text{jet}\#1)$. The rise in the “leading jet” case is, of course, due to hard initial and final-state radiation, which has been suppressed in the “back-to-back” events. The “back-to-back” events allow for closer look at the “beam-beam remnant” and multiple parton scattering component of the “underlying event” and PYTHIA Tune A (with multiple parton interactions) does a better job describing the data than HERWIG (without multiple parton interactions).

The “transMIN” densities are more sensitive to the “beam-beam remnant” and multiple parton interaction component of the “underlying event”. The “back-to-back” data show a decrease in the “transMIN” densities with increasing $P_T(\text{jet}\#1)$ which is described fairly well by PYTHIA Tune A (with multiple parton interactions) but not by HERWIG (without multiple parton interactions). The decrease of the “transMIN” densities with increasing $P_T(\text{jet}\#1)$ for the “back-to-back” events is very interesting and might be due to a “saturation” of the multiple parton interactions at small impact parameter. Such an effect is included in PYTHIA Tune A but not in HERWIG (without multiple parton interactions).

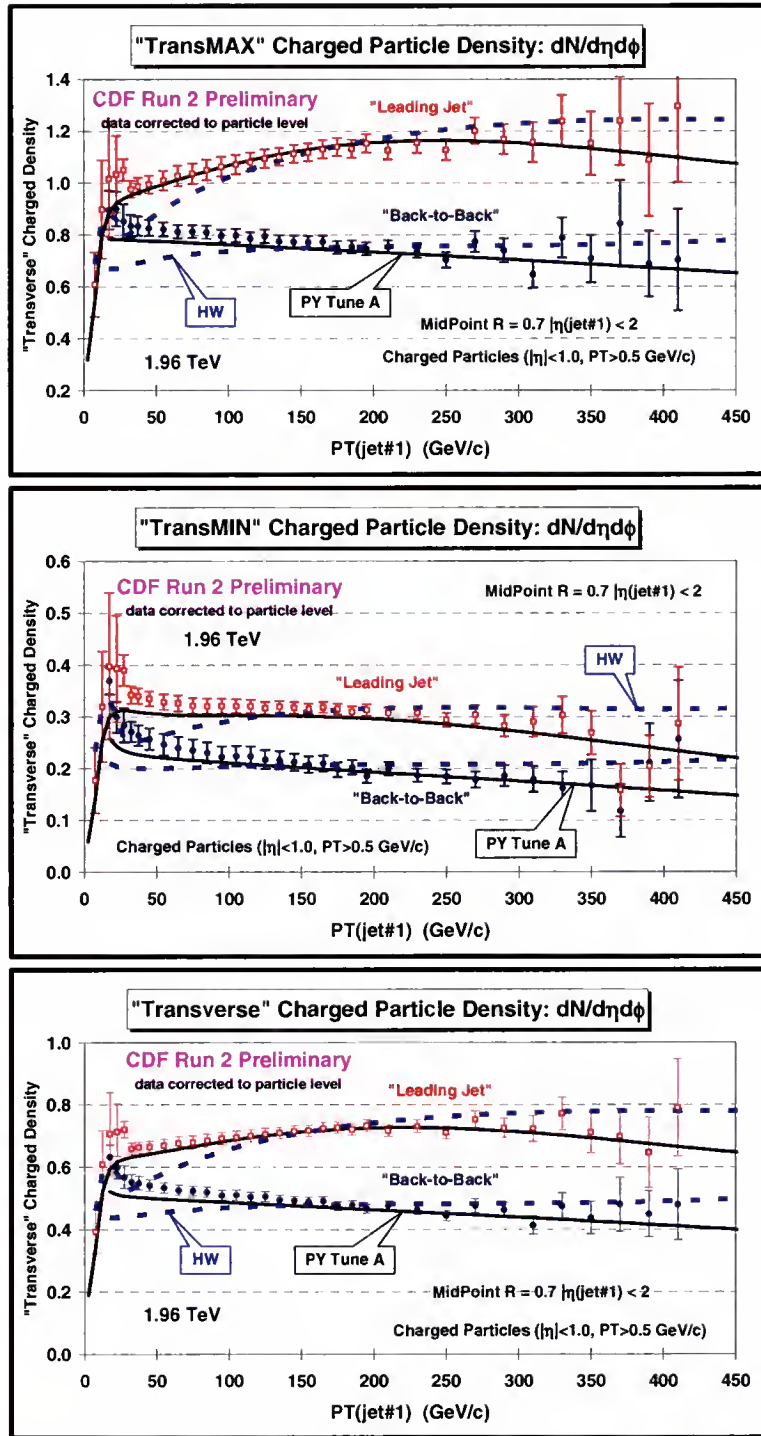


Figure 6-23: Data at 1.96 TeV on the density of charged particles, $dN_{ch}/d\eta d\phi$, with $p_T > 0.5$ GeV/c and $|\eta| < 1$ in the "transMAX" region (*top*), "transMIN" region (*middle*), and "transverse" region (average of "transMAX" and "transMIN") (*bottom*) for "leading jet" and "back-to-back" events defined in Fig. 6-3 as a function of the leading jet p_T compared with PYTHIA Tune A and HERWIG. The data are corrected to the particle level (with errors that include both the statistical error and the systematic uncertainty) and compared with the theory at the particle level (*i.e.* generator level).

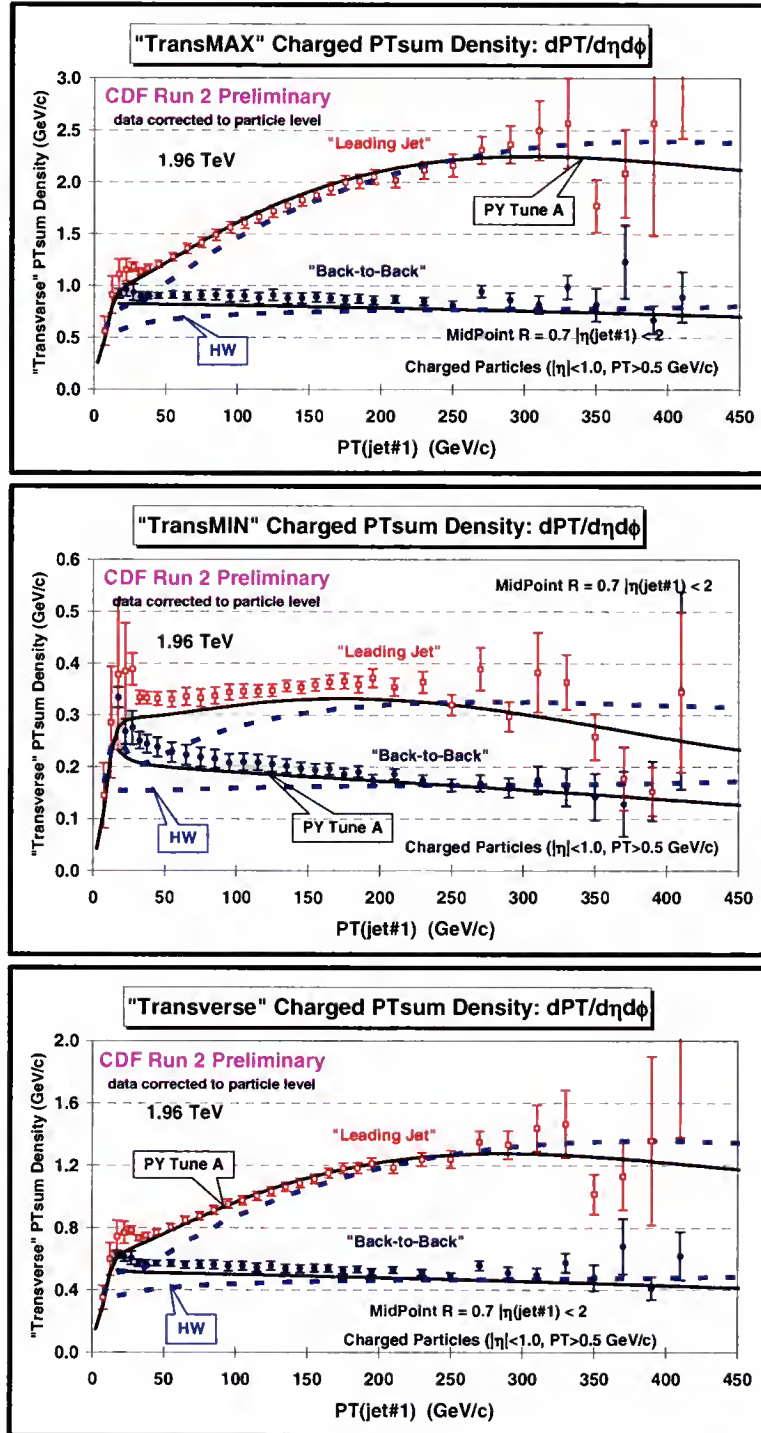


Figure 6-24: Data at 1.96 TeV on charged PTsum density of charged particles, $dPT_{\text{sum}}/d\eta d\phi$, with $p_T > 0.5$ GeV/c and $|\eta| < 1$ in the “transMAX” region (top), “transMIN” region (middle), and “transverse” region (average of “transMAX” and “transMIN”) (bottom) for “leading jet” and “back-to-back” events defined in Fig. 6-3 as a function of the leading jet P_T compared with PYTHIA Tune A and HERWIG. The data are corrected to the particle level (with errors that include both the statistical error and the systematic uncertainty) and compared with the theory at the particle level (*i.e.* generator level).

Fig. 6-25 compares the data on average $\langle p_T \rangle$ of charged particles and the average maximum charge particle p_T , PT_{max} , in the “transverse” region corrected to the particle level for “leading jet” and “back-to-back” events with PYTHIA Tune A and HERWIG at the particle level. Again the “leading jet” and “back-to-back” events behave quite differently.

Fig. 6-26 shows the data corrected to the particle level on the ETsum density, $dE_T/d\eta d\phi$, in the “transverse” region for “leading jet” and “back-to-back” events compared with PYTHIA Tune A and HERWIG at the particle level. Neither PYTHIA Tune A or HERWIG produce enough energy in the “transverse” region. HERWIG has more “soft” particles than PYTHIA Tune A does slightly better in describing the energy density in the “transMAX” and “transMIN” region.

Fig. 6-27 shows the data corrected on the charged fraction, PT_{sum}/ET_{sum} , in the “transverse” region for “leading jet” and “back-to-back” events compared with PYTHIA Tune A and HERWIG at the particle level. Neither PYTHIA Tune A or HERWIG produce enough energy in the “transverse” region and therefore predict too large of a charged fraction. Note that both PYTHIA Tune A and HERWIG predict a charged fraction of about 0.5 if one includes all particles in both P_{Tsum} and E_{Tsum} .

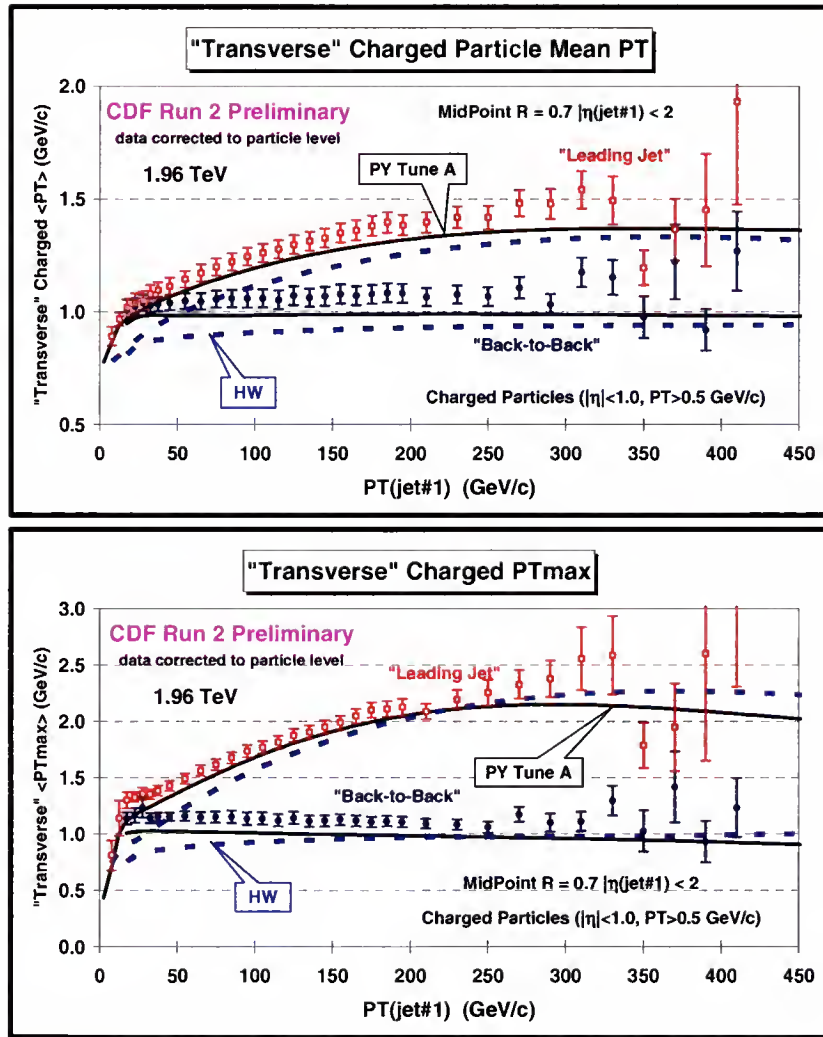


Figure 6-25: Data at 1.96 TeV on the average $\langle p_T \rangle$ of charged particles (*top*) and the average maximum p_T , PT_{max} , for charged particles (*bottom*) with $p_T > 0.5$ GeV/c and $|\eta| < 1$ in the “transverse” region for “leading jet” and “back-to-back” events defined in Fig. 6-3 as a function of the leading jet P_T compared with PYTHIA Tune A and HERWIG. The data are corrected to the particle level (with errors that include both the statistical error and the systematic uncertainty) and compared with the theory at the particle level (*i.e.* generator level).

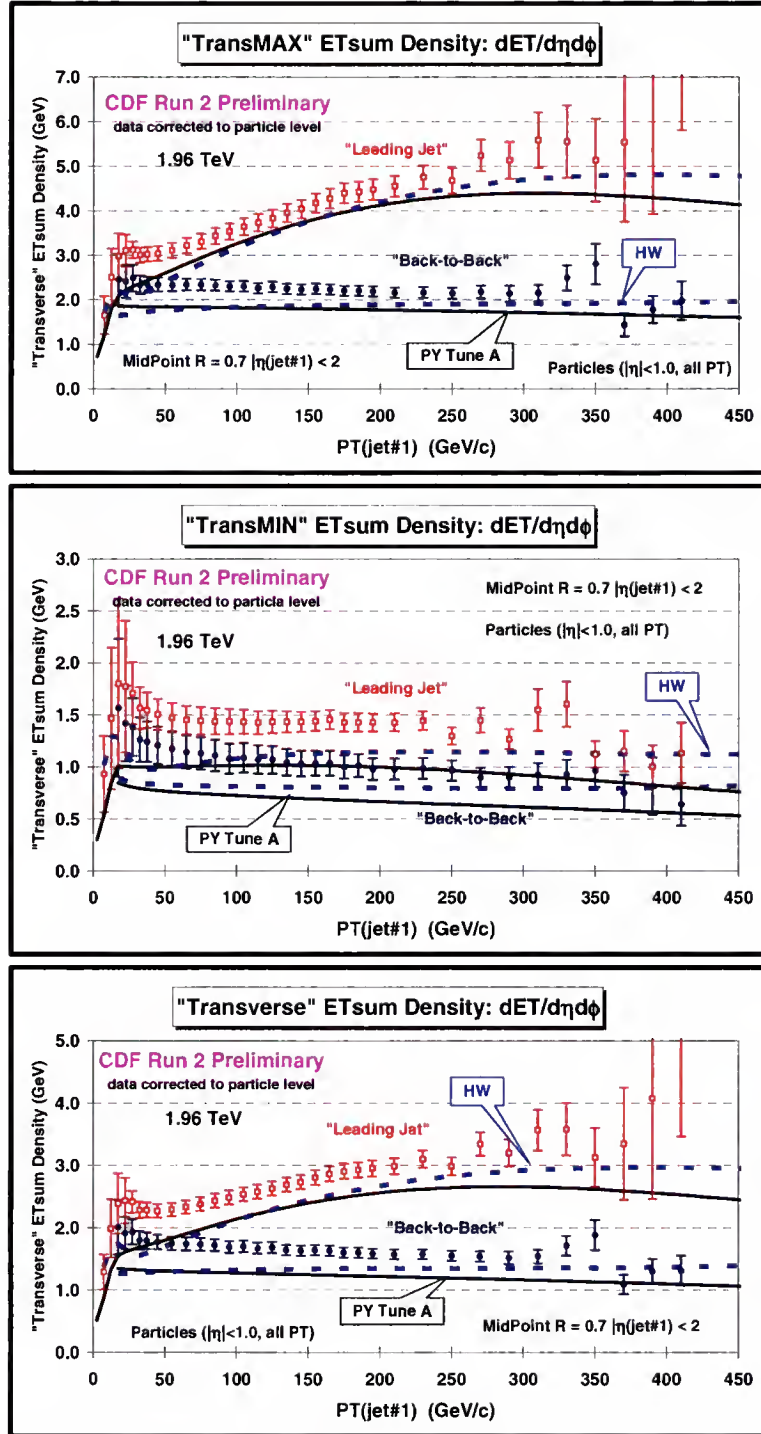


Figure 6-26: Data at 1.96 TeV on the ETsum density, $dE_T/d\eta d\phi$, for particles with $|\eta| < 1$ in the “transMAX” region (top), “transMIN” region (middle), and “transverse” region (average of “transMAX” and “transMIN”) (bottom) for “leading jet” and “back-to-back” events defined in Fig. 6-3 as a function of the leading jet P_T compared with PYTHIA Tune A and HERWIG. The data are corrected to the particle level (with errors that include both the statistical error and the systematic uncertainty) and compared with the theory at the particle level (*i.e.* generator level).

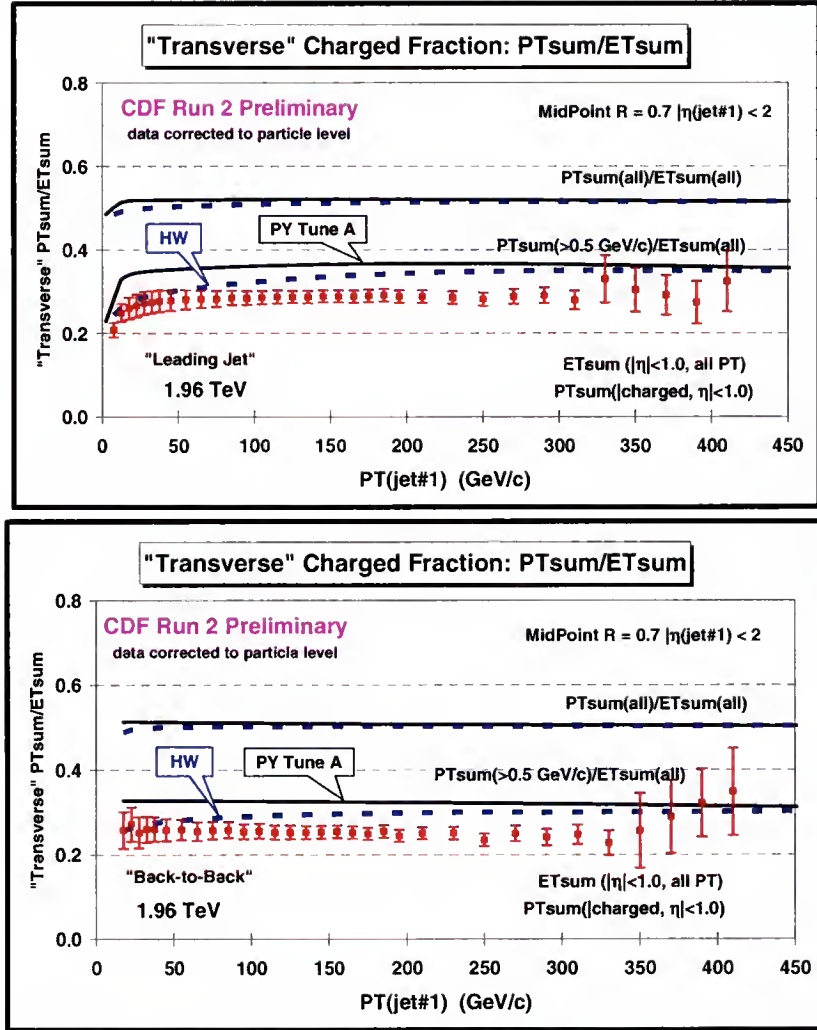


Figure 6-27: Data at 1.96 TeV on the charged fraction, PT_{sum}/ET_{sum} , in the “transverse” region defined in Fig. 6-3 for “leading jet” events (*top*) and “back-to-back” events (*bottom*) as a function of the leading jet P_T , where PT_{sum} includes charged particles with $p_T > 0.5$ GeV/c and $|\eta| < 1$ and the ET_{sum} includes all particles with $|\eta| < 1$, compared with PYTHIA Tune A and HERWIG. The data are corrected to the particle level (with errors that include both the statistical error and the systematic uncertainty) and compared with the theory at the particle level (*i.e.* generator level).

Figure 6-28 compares the corrected “leading jet” and “back-to-back” data on the density of charged particles, $dN/d\eta d\phi$, the P_{Tsum} density, $dP_{Tsum}/d\eta d\phi$, and the E_{Tsum} density, $dE_{Tsum}/d\eta d\phi$, for “TransDIF” (*i.e.* the “transMAX” region minus the “transMIN” region) as a function of the leading jet P_T . Figure 6-28 also shows the predictions of PYTHIA Tune A and HERWIG. The difference between “transMAX” and “transMIN”

is very sensitive to the “hard scattering” component of the “underlying event” (i.e hard initial and final-state radiation) and therefore we expect to see a big difference between “leading jet” events and the “back-to-back” events which is the case. Again, PYTHIA Tune A does a better job describing the data than does HERWIG for the charged particle densities and the charged $P_{T\text{sum}}$ densities. Surprisingly, both PYTHIA Tune A and HERWIG agree with the data for the “transDIF” $E_{T\text{sum}}$ density.

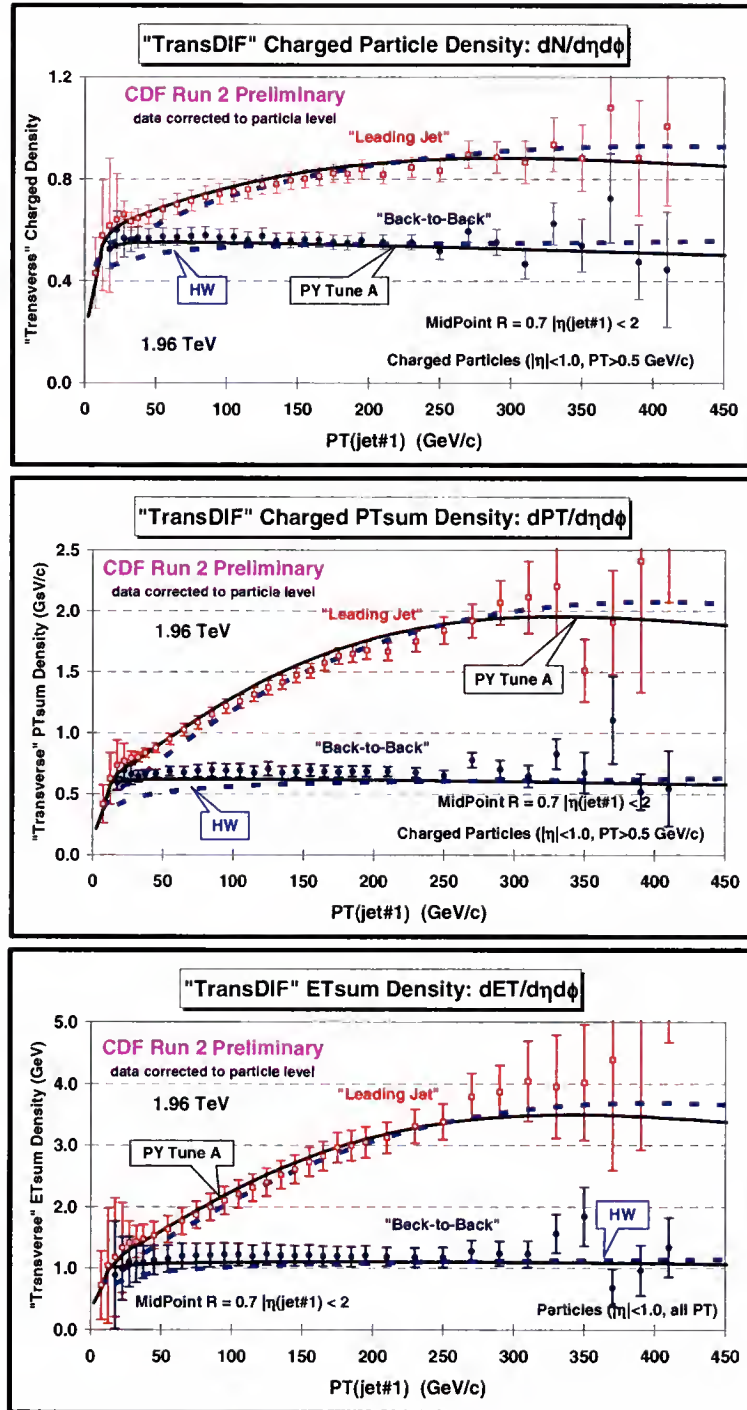


Figure 6-28: Data at 1.96 TeV on the density of charged particles, $dN/d\eta d\phi$ and the P_{Tsum} density, $dP_{Tsum}/d\eta d\phi$ for charged particles with $p_T > 0.5$ GeV/c and $|\eta| < 1$ for the "transMAX" minus the "transMIN" region defined in figure 6-3 for "leading jet" and "back-to-back" events defined in Fig. 6-2 as a function of the leading jet P_T compared with PYTHIA Tune A and HERWIG. The "transDIF" E_{Tsum} density, $dE_{Tsum}/d\eta d\phi$ for particles with $|\eta| < 1$ is also presented. The data are corrected to the particle level (with errors that include both the statistical error and the systematic uncertainty) and compared with the theory at the particle level (*i.e.* generator level).

CHAPTER 7

SUMMARY AND CONCLUSION

The goal of this analysis is to produce data on the “underlying event” that is corrected to the particle level so that it can be used to tune the QCD Monte-Carlo models without requiring CDF detector simulation (*i.e.* CDFSIM). Unlike our previous Run 2 “underlying event” analysis [6] which used JetClu to define “jets” and compared uncorrected data with PYTHIA Tune A and HERWIG after detector simulation (CDFSIM), in this analysis we use the MidPoint algorithm ($R = 0.7$, $f_{\text{merge}} = 0.75$) and correct the observables to the particle level. The corrected observables are then compared with PYTHIA Tune A and HERWIG at the particle level (*i.e.* generator level). This analysis also provides our first look at the energy in the “underlying event” (*i.e.* the “transverse” region).

In this analysis we look at both the charged particle and the energy components of the “underlying event”. We use the direction of the leading calorimeter jet in each event to define two “transverse” regions of η - ϕ space that are very sensitive to the “underlying event”. In addition, by selecting events with at least two jets that are nearly back-to-back ($\Delta\phi_{12} > 150^\circ$) with $P_T(\text{jet}\#3) < 15 \text{ GeV}/c$ we are able to look closer at the “beam-beam remnant” and multiple parton interaction components of the “underlying event”.

Comparing the corrected observables with PYTHIA Tune A and HERWIG at the particle level (*i.e.* generator level) continue to validate the conclusions we found when comparing the uncorrected data with the Monte-Carlo models after detector simulation (*i.e.* CDFSIM) [8]. PYTHIA Tune A (with multiple parton interactions) does a better job

in describing the “underlying event” (*i.e.* “transverse” regions) for both “leading jet” and “back-to-back” events than does HERWIG (without multiple parton interactions). Herwig does not have enough activity in the “underlying event” for $P_T(\text{jet\#1})$ less than about 150 GeV, which was also observed in a published Run I analysis [13].

Figure 7-1 compares the original Run I published data on the underlying event with our current results. We have extended the range of the leading jet P_T from 50 GeV to over 400 GeV. We now use the MidPoint Jet finding algorithm and most importantly correct the data back to the particle level.

This analysis gives our first look at the energy in the “underlying event” (*i.e.* the “transverse” region). Figure 6-28 shows that PYTHIA Tune A and HERWIG agree with the “transDIF” $E_{T\text{sum}}$ density data. Since both MC generators correctly predict the “hard scattering” component of the underlying event, this strongly suggests that the discrepancies and low jet#1 P_T reflect a needed tuning of the “beam-beam remnant” and multiple parton interaction components of the underlying event.

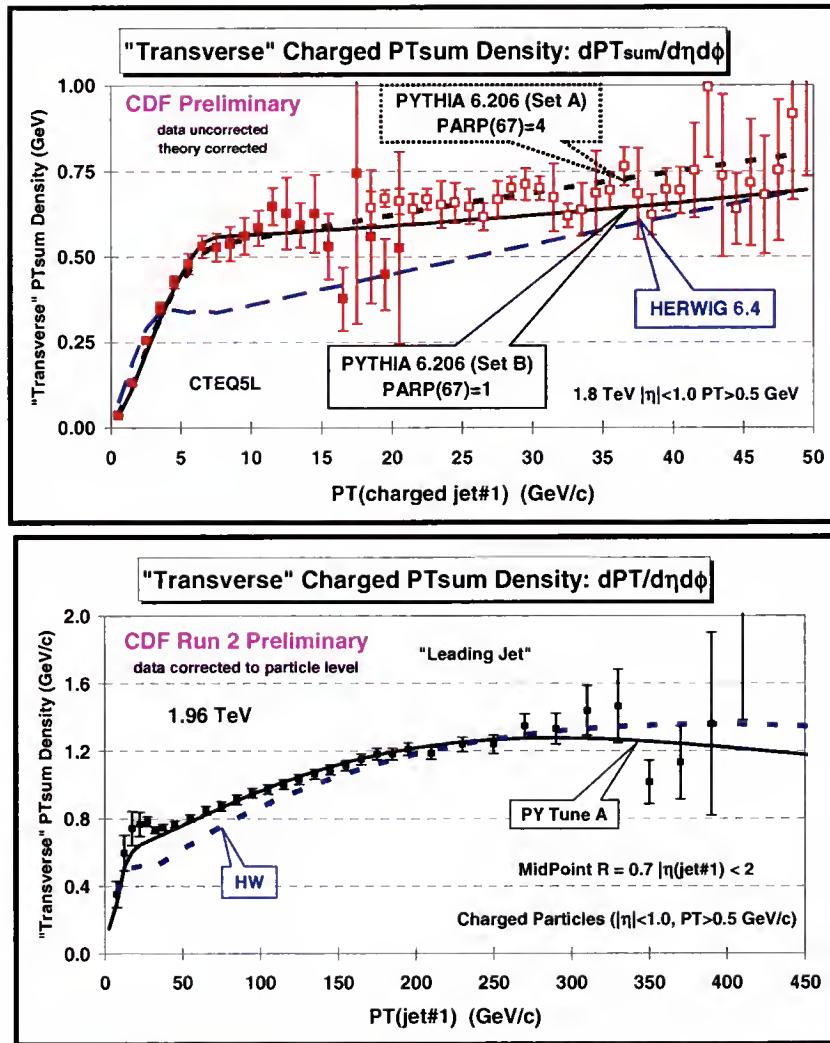


Figure 7-1: A comparison between the Run I and Run II analysis on the PTsum density in the "transverse" region. (*top*) Data uncorrected (with errors that include both statistical and the systematic uncertainty) at 1.8 TeV on the charged PTsum density, $dPT_{sum}/d\eta d\phi$, with $PT > 0.5$ GeV/c and $|\eta| < 1.0$ for leading jet events defined in Fig. 6-3 as a function of leading jet PT compared PYTHIA set A, PYTHIA set B, and HERWIG. (*bottom*) Data corrected (with errors that include both statistical and the systematic uncertainty) at 1.96 TeV on the charged PTsum density, $dPT_{sum}/d\eta d\phi$, with $PT > 0.5$ GeV/c and $|\eta| < 1.0$ for "leading jet events" defined in Fig. 6-3 as a function of leading jet PT compared PYTHIA Tune A and HERWIG.

REFERENCES

- [1] The CDF Collaboration (F. Abe et al.), Phys. Rev. Lett. 77, 438 (1996).
- [2] The D0 Collaboration (G.C. Blazey et al.), *Proceedings of the 31st Rencontres de Moriond: QCD and High-Energy Hadronic Interactions*, Les Arces, France (1996), p. 155: CDF and D0 Collaborations, Freedy Nang, FERMILAB-CONF-97-192-E
- [3] D. Kosower, *Extracting Parton Densities from Collider Data*, hep-ph/9708392.
- [4] G. Bodwin, Phys. Rev. D 31, 2616 (1985)
- [5] J.C. Collins, D.E. Soper, G. Sterman, Nucl. Phys. B 261, 104 (1985).
- [6] S. Mrenna, *Higher order corrections to parton showering from resummation calculations*, arXiv:hep-ph/9902471 v2 26 Mar 1999.
- [7] J. Pumplin, Phys. Rev. D 57, 5787 (1998)
- [8] R. Field, *The Underlying Event in Large Transverse Momentum Charged Jet and Z-Boson Production*, CDF/PUB/MIN_BIAS /PUBLIC/5463
- [9] R. Field, R. Haas, H. Frisch, D. Stuart, *The Underlying Event: Dijet vs. Z-jet*, CDF/ANAL/CDF/CDFR/5295 (2000)
- [10] R. Field, *The Underlying Event in Run 2*, CDF/ANAL/CDF/CDFR/6403 (2003)
- [11] A. Cruz, R. Field, *Using MAX/MIN Transverse Regions and Associated Densities to Study the Underlying Event*, CDF/ANAL/CDF/CDFR/6759 (2003)
- [12] A. Cruz, R. Field, *Jet Topologies in Min-Bias and Hard Collisions in Run 2 at the Tevatron*, CDF/ANAL/CDF/CDFR/6819 (2004).
- [13] R. Field, D. Stuart, *Charged Jet Evolution and The Underlying Event in Proton-Anitproton Collisions at 1.8 TeV*, CDF/PUB/CDF/CDFR/5453.
- [14] S. L. Glashow, Nucl. Phys. 22, 579, (1961).
- [15] S. Weinberg, Phys. Rev. Lett. 19, 1264 (1967).

- [16] J. F. Donoghue, E. Golowich, B.R. Holstein, *Dynamics of the Standard Model*, Cambridge Monographs on Particle Physics, Nuclear Physics and Cosmology, CUP, 1996 (reprinted).
- [17] F. Halzen, A. Martin, *Quarks and Leptons*, John Wiley and Sons, New York (1984).
- [18] The UA1 Collaboration (G. Arnison *et al.*), Phys. Lett. B 122, 103 (1983).
- [19] The UA2 Collaboration (P. Bagnaia *et al.*), Phys. Lett. B 122, 476 (1983).
- [20] The UA1 Collaboration (G. Arnison *et al.*), Phys. Lett. B 126, 398 (1983).
- [21] The UA2 Collaboration (P. Bagnaia *et al.*), Phys. Lett. B 129, 130 (1983).
- [22] R. Field, *Min-Bias and the Underlying Event at the Tevatron and the LHC*, talk presented at the Fermilab ME/MC Tuning Workshop, Fermilab, October 4, 2002.
- [23] R. Field, *Toward an Understanding of Hadron Collisions: From Feynman-Field until Now*, talk presented at the Fermilab Joint Theoretical Experimental “Wine & Cheese” Seminar, Fermilab, October 4, 2002.
- [24] R. Field, *Min-Bias and the Underlying Event at CDF*, talk presented at the Monte-Carlo Tools for the LHC Workshop, CERN, July 31, 2003.
- [25] A. Martin, W. J. Stirling, R. G. Roberts, Phys. Rev. D. 50 6734 (1994).
- [26] H1 Collaboration (C. Adloff *et al.*), Eur. Phys. J. C13 (2000) 609.
- [27] H1 Collaboration (C. Adloff *et al.*), Eur. Phys. J. C19 (2001) 269.
- [28] H1 Collaboration (C. Adloff *et al.*), Eur. Phys. J. C21 (2001) 33.
- [29] ZEUS Collaboration (S. Chekanov *et al.*), Eur. Phys. J. C21 (2001) 443.
- [30] D0 Collaboration (B. Abbott *et al.*), Phys. Rev. Lett. 86 (2001) 1707.
- [31] CDF Collaboration (T. Affolder *et al.*), Phys. Rev. D64 (2001) 032001.
- [32] G. Altarelli, G. Parisi, Nucl. Phys. B126 (1977) 298.
- [33] T. Sjöstrand, *High-Energy-Physics Event Generation with PYTHIA 5.7 and JETSET 7.4*, CERN-TH.711/93, December, 1993.
- [34] G. Abbiendi, I. G. Knowles, G. Marchesini, B. R. Webber, M. H. Seymour, and L. Stanco, Comput. Phys. Commun. 67, 465 (1992)
- [35] J.D. Bjorken, Phys Rev D 47, 101 (1993)
- [36] E. Gotsman, E.M Levin, and U. Maor, Phys. Lett. B 309, 199 (1993)

- [37] The CDF Collaboration (F. Abe *et al.*), Phys. Rev. Lett. 74, 855 (1995)
- [38] The D0 Collaboration (S. Abachi *et al.*), Phys. Rev. Lett. 76, 734 (1996).
- [39] Fermi lab Beam Division, *Run II Handbook*, http://www-bd.fnal.gov/lug/runII_handbook/RunII_index.html., The CDF Collaboration, 1998 (accessed August 2005)
- [40] The CDF II Collaboration , *The CDF II Detector Technical Design Report*, FERMILAB-PUB-96/390-E (1996).
- [41] The D0 Collaboration, *The D0 Detector*, Nuclear Instruments and Methods, A 338, 185 (1994). D0 Collaboration's Run II Nuclear Instruments and Methods paper in preparation.
- [42] The CDF Collaboration, *Proposal for Enhancement of the CDFII Detector. An Inner Silicon Layer and Time of Flight Detector*, FERMILAB-Proposal-909 (1998).
- [43] L. Balka, *The CDF Central Electromagnetic Calorimeter*, Nucl. Instrum. Meth. A 267 (1988) 272-279.
- [44] S. Bertolucci, *The CDF Central and Endwall Hadron Calorimeter*, Nucl. Instrum. Meth. A 267 (1988) 301-314.
- [45] A. Albrow, *The CDF plug Upgrade Electromagnetic Calorimeter: Test Beam Results*, Nucl. Instrum. Meth. A 480 (2002) 524-546.
- [46] K. Yasuoka, *Response Maps of the CDF Central Electromagnetic Calormeter with Electrons*, Nucl. Instrum. Meth. A 267 (1998) 315-329.
- [47] S.D. Ellis, J. Huston, M. Tönnesmann, *Building Better Cone Jet Algorithms*, (2003)
- [48] G.C Blazey, *et. al. Run II Jet Physics: Proceedings of the Run II QCD and Weak Boson Physics Workshop*, hep-ex/0005012
- [49] P. Aurenche, *et. al., The QCD and Standard Model Working Group: Summary Report from Les Houches*, hep-ph/0005114.
- [50] J.E. Huth, *et al., Proceedings of Research Directions for the Decade: Snowmass 1990*, July 1990, edited by E.L. Berger (World Scientific Singapore, 1992). P. 134.
- [51] S.D. Ellis, J. Huston, M. Tönnesmann, hep-ph/0111434
- [52] G. Marchesini and B. R. Webber, Nucl. Phys B310, 461 (1988); I. G. Knowles, Nucl. Phys. B310, 571 (1988)
- [53] S. Catani, G. Marchesini, B. R. Webber, Nucl. Phys. B349, 635 (1991).

- [54] Anwar Bhatti, Eve Kovacs, Joey Huston, and Valeria Tano *Comparison of Soft Momentum Distribution in CDF data and HERWIG+QFL at 1800 and 630 GeV.*, CDF/ANAL/JET/CDFR/5600.
- [55] Anwar Bhatti, Joey Huston, Eve Kovacs, and Valeria Tano, *Comparison of Underlying Event Energy in Herwig and CDF Data*, CDF/ANAL/JET/CDFR/5214.

BIOGRAPHICAL SKETCH

Luis Alberto Cruz was born on July 2, 1972, in New Haven, Connecticut. After graduating from Amity High School in 1990, he continued his education at the University of New Haven in West Haven Connecticut.

In 1995 he received his Bachelors of Science in biology and began doing research at the John B. Pierce Laboratories at the Yale School of Medicine. In 2000 he published a paper in the journal *Nature* on his discovery of Thermal Taste.

In the summer of that same year Luis Alberto Cruz changed fields and became a graduate student in the Department of Physics at the University of Florida. He was honored with the Departmental and University Graduate student teaching awards in 2003. In 2004 he joined the CDF collaboration and worked with Professor Richard Field on the “underlying” event at the Tevatron.

In 2005, Luis Alberto Cruz graduated from the University of Florida with a degree of Doctor of Philosophy.

USING MAX/MIN TRANSVERSE REGIONS TO STUDY THE UNDERLYING EVENT IN RUN2 AT THE TEVATRON

Luis Alberto Cruz
(352) 514-8490, Alberto@phys.ufl.edu
Department of Physics
Chair: Richard Field
Degree: Doctor of Philosophy
Graduation Date: July 2005

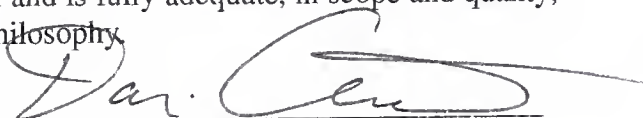
Elementary particle physics attempts to answer very fundamental questions of how the Universe was created and how it works. One approach to unlocking these mysteries is by colliding very fast moving protons and antiprotons and studying the outcome. Most of the time these particles ooze through each other, but occasionally we get a collision that is characterized by a large amount of transverse momentum. This signals a special kind of collision that can be calculated by the theorist. The problem lies in the fact that only a portion of the collision can be calculated. The majority of the collision is messy and must be modeled. The data presented here helps to improve the current models and allows for a better understanding of the dynamics of nuclear forces.

I certify that I have read this study and that in my opinion it conforms to acceptable standards of scholarly presentation and is fully adequate, in scope and quality, as a dissertation for the degree of Doctor of Philosophy.



Richard Field, Chair
Professor of Physics

I certify that I have read this study and that in my opinion it conforms to acceptable standards of scholarly presentation and is fully adequate, in scope and quality, as a dissertation for the degree of Doctor of Philosophy.



Darin Acosta
Professor of Physics

I certify that I have read this study and that in my opinion it conforms to acceptable standards of scholarly presentation and is fully adequate, in scope and quality, as a dissertation for the degree of Doctor of Philosophy.



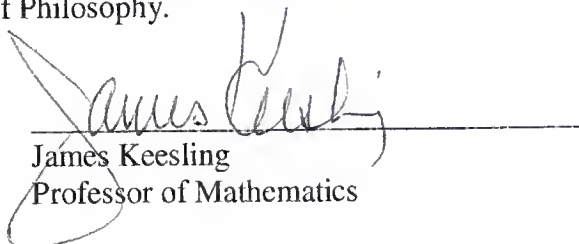
James Fry
Professor of Physics

I certify that I have read this study and that in my opinion it conforms to acceptable standards of scholarly presentation and is fully adequate, in scope and quality, as a dissertation for the degree of Doctor of Philosophy.



Pierre Sikivie
Professor of Physics

I certify that I have read this study and that in my opinion it conforms to acceptable standards of scholarly presentation and is fully adequate, in scope and quality, as a dissertation for the degree of Doctor of Philosophy.



James Keesling
Professor of Mathematics

LD
1780
20 05

.C957

UNIVERSITY OF FLORIDA



3 1262 08553 7230